Spring 2007

Measurements of Correlated Pair Momentum Distributions in -3He(e,e',p,p)n with CLAS

Hovhannes Baghdasaryan
Old Dominion University

Follow this and additional works at: https://digitalcommons.odu.edu/physics_etds

Part of the Elementary Particles and Fields and String Theory Commons, and the Nuclear Commons

MEASUREMENTS OF CORRELATED PAIR MOMENTUM DISTRIBUTIONS IN ^{3}He(e,e'pp)n WITH CLAS

by

Hovhannes Baghdasaryan
M.S. June 2005, Old Dominion University

A Dissertation Submitted to the Faculty of
Old Dominion University in Partial Fullfillment of the
Requirement for the Degree of

DOCTOR OF PHILOSOPHY

PHYSICS

OLD DOMINION UNIVERSITY
May 2007

Approved by:

Dr. Lawrence B. Weinstein (Director)

Dr. Moskow Amaryan

Dr. Wallv Van Orden _

Dr. Charles I. Sukenik

Dr. Li Shi Luo

ABSTRACT

MEASUREMENTS OF CORRELATED PAIR MOMENTUM DISTRIBUTIONS IN ^{3}He(e,e'pp)n WITH CLAS

Hovhannes Baghdasaryan
Old Dominion University, 2007
Director: Dr. Lawrence B. Weinstein

Nucleon-Nucleon (NN) Short Range Correlations (SRC) represent a valuable part of the nuclear wave function. Improved knowledge of SRC will give us a better understanding of nuclear matter and nuclear interactions in extreme conditions. A study of the effects of short-range correlations using the ^{3}He$(e, e'pp)n$ reaction measured at Jefferson Lab is presented. Two different approaches were selected to investigate SRC. The first approach consists of the kinematics when we investigate the two active protons and neutron is the spectator (was not involved in the interaction). This kinematics dominates by Final State Interactions which are reasonably well described by Laget calculations. The second approach consists of the kinematics when the one nucleon carries almost all energy of the virtual photon and the subject of interest is the spectator pair. Looking at the reactions, we can extract the kinematic regions where the NN SRC is an almost non interacting spectator pair. We have measured the relative and total momentum distributions of spectator pp and pn pairs up to 600 MeV/c. The theoretical calculations generally fail to describe the data.

ACKNOWLEDGMENTS

I would like to thank everybody who helped me to write this dissertation. Especially my family members whose support helped to write this dissertation a second time. I would like to thank my father, Albert S. Baghdasaryan who helped me understand the importance of a good education and hard work. Thanks to my uncle, Dr. Valery S. Baghdasaryan, who interested me in physics and was constantly an example to me. Thanks to my mother, Irina G. Baghdasaryan, who found all the right words to keep my spirits up.

I am very grateful to all of the faculty and staff of the Old Dominion University Physics Department, and especially to my adviser, Dr. Larry Weinstein, who helped me not only as a great mentor but also as a great teacher. His ability to explain complicated problems to me speak of his high standards as a teacher and a leader. I also want to mention Dr. Moskov Amaryan who helped me to understand not only nuclear but also hadronic physics. His energy and interest in the science created new understanding of the word "Researcher". Also, I would like to thank Anatoly Radyushkin who is probably one of the greatest physicists I know, and to Mark Havey who helped me understand that and to accept the fact that life can't be planned because there is always the probability of something going incredibly wrong.

I would like to thank Dr. Stepan Stepanyan for help in understanding the CLAS detector and for the advising he did at the beginning of my education. I want to thank Kim Egiyan for the opportunity he created for me in the nuclear physics field. Also, I would like to thank the friends who helped me professionally and emotionally during the preparation of this dissertation: Theresa Lindeman, Gagik Gavalian, Aram Teymurazyan, Hrayr Matevosyan and Heghine Seraydaryan.

TABLE OF CONTENTS

LIST OF TABLES

LIST OF FIGURES

CHAPTER 1

INTRODUCTION

One of the main problems in nuclear physics is to understand the nucleus and the interactions inside the nucleus[1]. We need the answer to three main questions in order to completely understand the nuclear medium:

- What is the charge distribution in the nucleus?

- What is the matter distribution in the nucleus?

- What is the momentum distribution of the matter inside of the nucleus?

High precision elastic electron scattering experiments precisely measured the nuclear charge density distribution. This challenged the independent particle model (IPM or Hartree -Fock approximation) to describe the nuclear ground state. Without repulsive short-range forces between the nucleons, even a heavy nucleus like ^{238}U will collapse. The strong repulsive part of the nucleon-nucleon (NN) interaction in the many body system is referred to as the Short Range Interaction (SRI) and the effects of this repulsion are called Short Range Correlations (SRC).

The IPM approximation adopted the single particle model. The Hamiltonian in this approximation can be written as

$$H = \sum_i T_i + \sum_{i<j} V_{ij} = \sum_i (T_i + U_i) + (\sum_{i<j} V_{ij} - \sum_i U_i)$$

where T_i is the kinetic energy, V_{ij} is the NN interaction between the ith and jth nucleons, and U_i is the single particle potential (the average potential acting on nucleon i due to the presence of all the other nucleons). The residual interaction $(\sum_{i<j} V_{ij} - \sum_i U_i)$ is small (ignored or treated by variational methods in the IPM). In the IPM the motion of each nucleon inside of the nucleus is not affected by the other individual nucleons. This approximation gives a good description of some general properties of the nucleus such as the charge distribution (or charge density) but it fails to describe the momentum density distribution.

---

[1]This Dissertation follows the form of *The Physical Review, C*

Even though the nucleus itself can be at rest, the nucleons inside are in constant motion. Quantum mechanically, this means that we have a wave function $\psi(\vec{p_1}, \vec{p_2}, ..., \vec{p_N})$. As the wave function of a free particle with momentum $\vec{p}$ is $\phi(\vec{p})$, the probability of finding a nucleon with a certain momentum p is $|\langle \phi(\vec{p})|\psi(\vec{p_1}, \vec{p_2}, ..., \vec{p_N})\rangle|^2$. A full calculation of the wave function will include the correlations of all orders. It is important to note that the averaging over the strong short range repulsive part of the NN potential is inaccurate, especially at short NN distances.

Correlations are corrections to the IPM. The mathematical description of the momentum density distribution inside of the nucleus is

$$\rho(\vec{p}) = \sum_{i=1}^{A} \rho_i(\vec{p}) + \int \sum_{i<j}^{A} \rho_{ij}(\vec{p}, \vec{p_2}) dp_2 + ...$$

where the first sum corresponds to the single nucleon momentum distribution and the second sum is two body correlations $(\rho_{ij}(\vec{p_1}, \vec{p_2}) \neq \rho_i(\vec{p_1}) \cdot \rho_i(\vec{p_2})$ for correlated nucleons). The density distribution is directly connected to the wave function of the nucleus.

The main challenge is to obtain the correct wave function from the solution of the non-relativistic Schrödinger equation. There are several nucleon-nucleon phenomenological potentials on the market (AV18, Nijm-I, Nijm-II, CD-Bonn, Reid 93) which allow us to calculate the wave functions for light nuclei. Each of these potentials has a slightly different Short Range Interaction (SRI) and mostly the same Long Range Interaction (LRI).

Correlations, especially in heavy nuclei, have traditionally been calculated as a correction to the IPM wave function. As an artifact of this approach to nuclear structure usually starting from IPM, we distinguish between two kinds of correlations: Short and Long Range. The Long Range Correlations (LRC) are produced by collective excitation modes of the nucleus caused by the part of Hamiltonian neglected in the IPM. LRC are due to the finite size of the nucleus and are well explained by light meson exchange (π^+, π^- and π^0). The Short Range Correlations (SRC) are generated by the hard core repulsion of the nucleon-nucleon interaction which prohibits two nucleons from approaching too close to each other.

First of all, let us try to define the correlation between two nucleons in a heavy nucleus. The correlation can originate from the central repulsive and tensor forces. The complete correlation operator has the form

$$C = C_\Omega C_r$$

where C_r is the radial term (called the Radial Correlation operator) and C_Ω is the tensor term (called the Tensor Correlation operator). The radial operator C_r

$$C_r = \exp(-i \sum_{i<j} \frac{1}{2}(s(r_{ij})p_{r_{ij}} + p_{r_{ij}}s(r_{ij})))$$

[1] shifts a pair of particles in the radial direction away from each other (uses the radial momentum operator p_r together with the shift function $s(r)$ where r is the distance between two nucleons). $s(r)$ is large at short distances and vanishes at large distances.

The tensor force depends on the spins and the spacial orientation of the nucleons $\hat{r}_{ij} = (\vec{r_i} - \vec{r_j})/(|\vec{r_i} - \vec{r_j}|)$. The tensor operator

$$C_\Omega = \exp\{-i \sum_{i \neq j} \frac{3}{4}\theta(r_{ij})[(\vec{\sigma}_i\hat{r}_{ij})(\vec{\sigma}_j\vec{p}_{\Omega_{ij}}) + (\vec{\sigma}_j\vec{p}_{\Omega_{ij}})(\vec{\sigma}_i\hat{r}_{ij})]\}$$

shifts perpendicular to the relative $\hat{r}_{ij}$. $\vec{p}_\Omega$ is the orbital part of the momentum operator and $\theta(r_{ij})$ is a function that controls the strength of the tensor correlations.

The shift of particles in the radial direction away from each other due to the short range repulsive force is called Short Range Correlations. In the particular case of two body SRC, the momentum of both particles should be equal to each other and opposite. Also the momentum of each particle should be higher than the Fermi momentum of the nucleus (i.e., than the typical momentum of nucleons in the nucleus).

This is not relevant to ^{3}He where there are no IPM calculations and the bound state wave function can be solved exactly [2]. Therefore we need to develop an operator-independent definition of correlations. For this purpose we will restrict ourselves to two nucleon correlations. Then **the effect when a nucleons momentum is balanced by the momentum of only one other nucleon is called an SRC.** Thus, the experimental signature of an SRC will be an NN pair with small total momentum p_{tot} and large relative momentum p_{rel}. In this thesis we will not distinguish between Radial and Tensor correlations.

It is important to mention that the investigation of SRC is experimentally compli-
cated because of several other competing effects (like Final State Interactions (FSI),
Isobar configurations (IC) and Meson Exchange Currents (MEC)).

Quite a few experimental attempts were made to investigate SRC. One of the
most important measurements (but model dependent) of the SRC is the momentum
distribution of the nucleons in the nucleus. The direct connection with the wave
function shows the contribution of different effects into the cross section.

Inclusive quasielastic $A(e, e')X$ measurements at $x_B > 1$ provide information
about the momentum distribution of the nucleons in the nucleus. This momentum
distribution includes all effects such as two nucleon and three nucleon correlations.
Any additional requirement may allow us to extract more information about differ-
ent effects. For example direct comparison of the momentum density $n(k)$ between
theory and experiment for different nuclei has been done by Ciofi degli Atti et $al.$
[3]. Figure 1 shows $n(k)$ extracted from the experimental data compared to the-
oretical calculations. $n(k)$ is obtained from the experimental cross sections by a
model dependent derivation. The theoretical calculations of $n(k)$ contain two terms
$n_0(k)$ (Hartree-Fock + Soft Core approximation) and $n_1(k)$ (SRC). The $n_0(k)$ term
corresponds to the $A - 1$ residual nucleus left relatively unexcited and the $n_1(k)$
corresponds to the $A - 1$ residual nucleus in a highly excited state (usually a second
nucleon is emitted).

The dotted and solid lines on Figure 1 correspond to the momentum density with-
out $(n_0(k))$ and with $(n_0(k) + n_1(k))$ SRC respectively. The open triangles represent
$n_0(k)$ obtained from $A(e, e'p)A - 1$ exclusive experiments. The open squares repre-
sent $n(k)$ obtained from inclusive $A(e, e')X$ experiments. In the case of $A(e, e')X$,
the cross sections were obtained using the information of the scattered electron only
and thus are integrated over all nuclear final states. The filled triangles are extracted
from the inclusive reaction $A(e, e'p)X$. Here the proton momentum distribution was
obtained directly from measuring the protons. In the case of ^{3}He, the open trian-
gles show the ^{3}He$(e, e'p)d$ reaction. The ^{3}He$(e, e'p)d$ reaction does not include the
effects of the proton belonging to an SRC since in that case the deuteron would have
broken up. The closed triangles show $n(k)$ derived from the ^{3}He$(e, e'p)X$ reaction,
integrating over all final states.

It is important to mention several features of the theoretical calculations and the data:

- $n_0(k)$ drops rapidly at $k > 1.8$ fm^{-1}.

- $n_0(k)$ agrees well with $A(e, e'p)A - 1$ exclusive experiments.

- $n_0(k) + n_1(k)$ agrees well with $A(e, e')x$ and $A(e, e'p)X$ experiments.

Unfortunately no data were available then for exclusive reactions on heavier nuclei. However, assuming that the calculations are correct, the results show the huge contribution of SRC to the momentum distribution at large momentum. Note that the predictions show almost the same behavior for $n_1(k)$ for all nuclei with $A > 2$.

While it is not possible to determine $n(k)$ unambiguously from $A(e, e')$ data, by taking ratios of (e, e') cross sections on different nuclei, many of the ambiguities cancel. Ratios of (e, e') cross sections were measured recently using the CEBAF Large Acceptance Spectrometer (CLAS) in Hall-B at the Thomas Jefferson National Laboratory (TJNAF). Indications of SRC both in heavy and light nuclei were observed. Figure 2 shows the (e, e') cross section ratios R_{He3}^A for a) ^{12}C and b) ^{56}Fe with respect to ^{3}He as a function of $x_B = \frac{Q^2}{2m_p\omega}$ for $1.4 < Q^2 < 2.6$ (GeV/c)^2 [4] where the 4-momentum transfer $Q^2 = 2EE' \sin^2(\theta_e/2)$, E is the electron beam energy, E' is the scattered electron energy, θ_e is the scattered electron angle, and $\omega = E - E'$ is the transferred energy. The cross section ratios are constant (scale) for $x_B > 1.5$. This scaling is predicted by the Short Range Correlation model [5] and indicates the dominance of scattering from correlated NN pairs. These ratios in the scaling regime are proportional to the relative probability of NN correlations in the two nuclei. The contribution of FSI for all the nuclei was estimated to be the same, and thus cancels in the ratio. These results tell us the relative probability of SRC in the different nuclei but do not tell us anything about their momentum distributions.

Earlier more evidence for SRC was obtained from the $(e, e'p)$ reaction on heavier nuclei. Bobeldijk *et al.* [6] shows missing momentum distributions of low-lying states in the reaction ^{208}Pb$(e, e'p)^{207}$Tl compared to several non-relativistic Distorted Wave Impulse approximation (DWIA) calculations (see Figure 3). Three of the calculations [7, 8, 9] included different ways to account for long-range and short-range correlations (LRC) and (SRC). The DWIA calculations without SRC reproduce the data up until
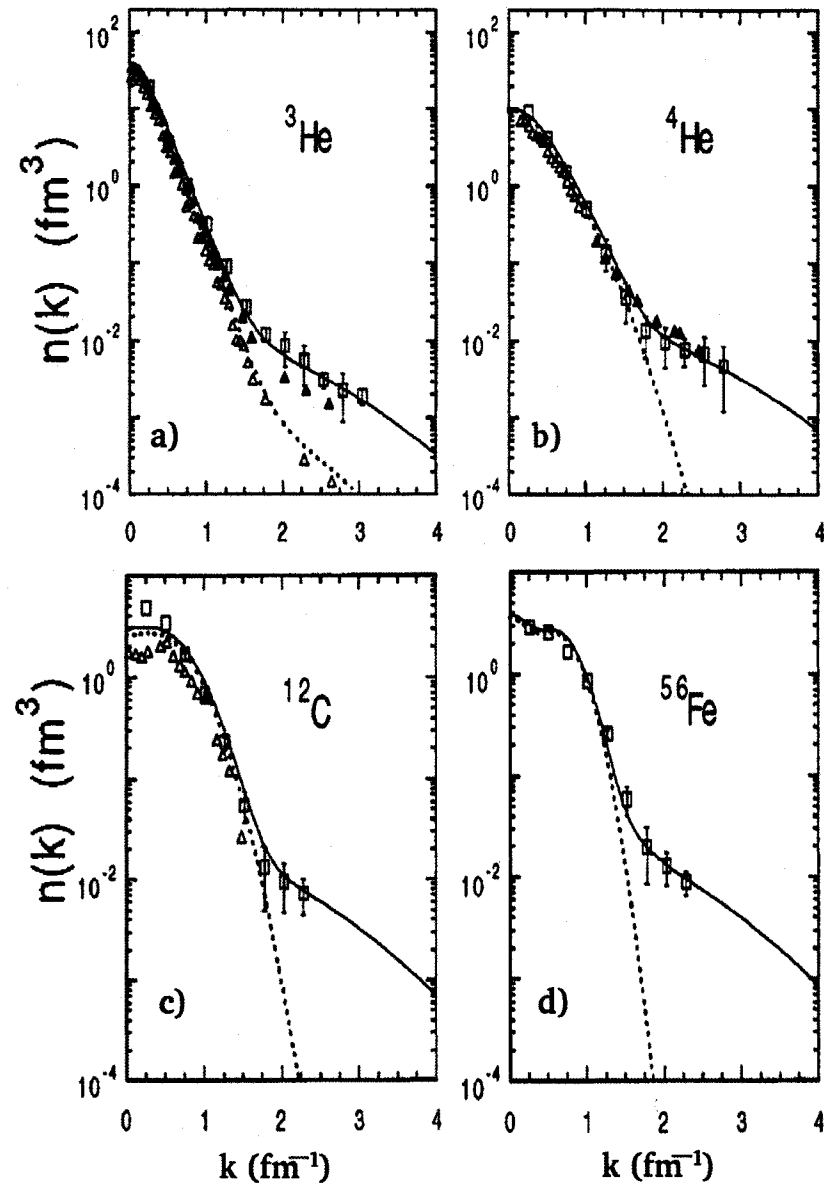
FIG. 1. The many-body nucleon momentum distribution $n(k)$. The dotted and solid lines corresponds to the momentum distribution without and with the effects of SRC respectively. The open triangles represent the experimental data obtained from exclusive $A(e, e'p)A - 1$ measurements. The data presented with open squares were obtained from inclusive $A(e, e')X$ measurements. The filled triangles were extracted from inclusive reaction $A(e, e'p)X$ measurements.
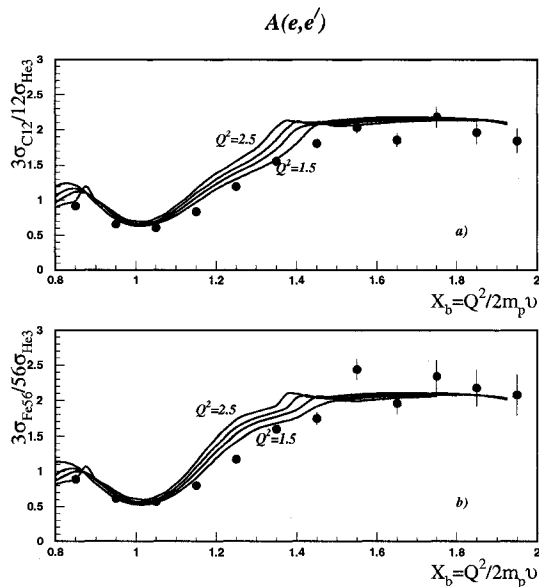
FIG. 2. $A(e, e')$ cross section ratios to ^{3}He. $R_{\text{He3}}^A(x_B)$ is shown as a function of x_B for $1.4 < Q^2 < 2.6$ (GeV/c)^2. Curves are Short Range Correlation model predictions. a) ^{12}C, b) ^{56}Fe [4].

$p_m = 300$ MeV/c. The rest of the data can be explained qualitatively by including by LRC and SRC. The SRC and LRC can account for some of the discrepancy but do not describe the data well enough.

More evidence for NN correlations was obtained in Hall-A at TJNAF by measuring the ^{16}O$(e, e'p)$ reaction at missing energies $E_{miss} = \omega - T_p - T_{A-1}$ (energy of the $A - 1$ nucleus) up to 120 MeV [17]. Figure 4 shows the six-fold differential cross section for four different missing momenta. The histogram and points show the experimental cross sections. The solid line is the DWIA calculation of the s-shell by Kelly [11], folded with the Lorentzian parametrization of Mahaux [16]. The dashed line is the two nucleon knockout calculation by Ryckebusch [12, 13, 14, 15] including contributions from pion exchange and intermediate $\Delta(1232)$ and central short range correlations. The dot dashed line also includes tensor correlations.

The energy of the beam was 2.4 GeV, $Q^2 = 0.8$ (GeV/c^2)^2 and $\omega = 445$ MeV. The peaks at $E_{miss} = 12$ MeV and 18 MeV correspond to proton knockout from the $1p$-shell and are described by relativistic DWIA calculations. At low missing momenta there is a peak centered at $E_{miss} \approx 40$ MeV corresponding to proton knockout from
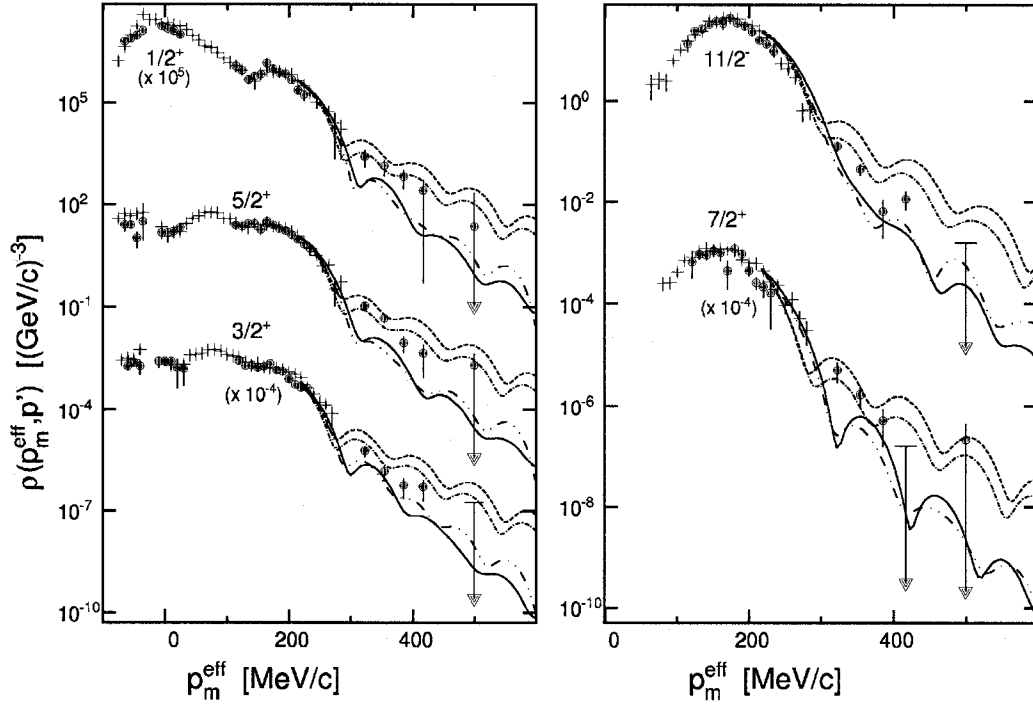
FIG. 3. Missing momentum distribution for low-lying states in the reaction ^{208}Pb$(e, e'p)^{207}$Tl. Solid circular – data [6], plus – data [10], the solid lines – DWIA calculations (no correlations in wave function), dash double dotted – with correlation by Pandharipande [7], dashed – with correlation by Ma and Wambach [8], dot dashed – with correlations by Mahaux and Sartor [9].

the s-shell. The threshold for two nucleon knockout is approximately 25 MeV. The s-shell peak vanishes beneath a flat background as the missing momentum increases. Single proton knockout explains the cross sections only at low p_{miss} up to $E_{miss} < 60$ MeV. The flat continuum observed at large p_{miss} was qualitatively explained by Ryckebusch [12, 13, 14, 15] with a two nucleon knockout $((e, e'pp)$ and $(e, e'pn))$ calculations, including pion exchange, intermediate $\Delta(1232)$ production, and central and tensor correlations. The full calculation is still a factor of two below the data.

More evidence of SRC was obtained from measurements of ^{16}O$(e, e'pp)^{14}$C performed by Starink *et al.* at NIKHEF [18]. Figure 5 shows the differential cross sections as a function of missing energy and missing momentum [18] for two proton
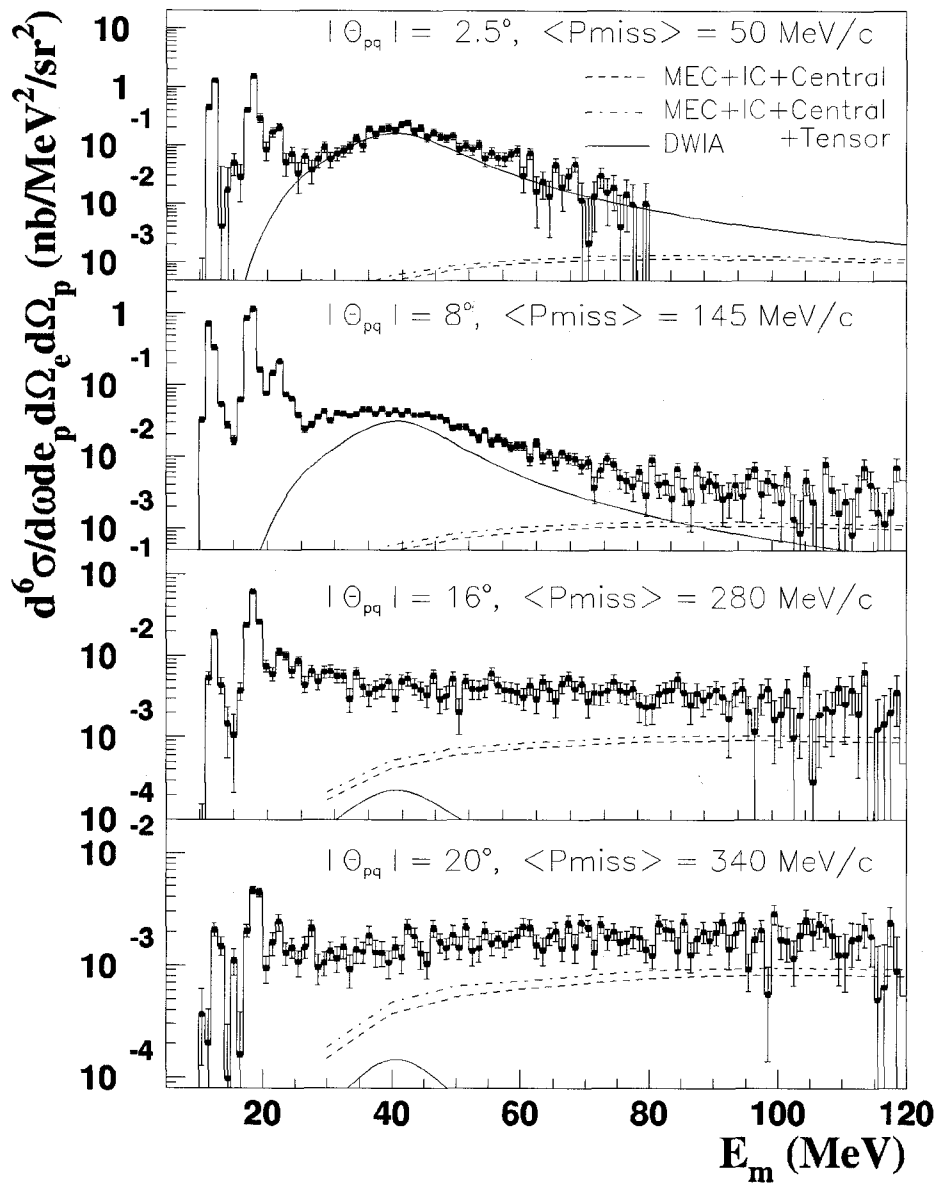
FIG. 4. Cross section for the $^{16}O(e, e'p)$ reaction as a function of missing energy for different missing momenta. The histogram and points show the experimental cross sections. The solid line is the DWIA calculation of the s-shell by Kelly [11], folded with the Lorentzian parametrization of Mahaux [16]. The dashed line is the two nucleon knockout calculation by Ryckebusch [12, 13, 14, 15] including contributions from pion exchange and intermediate $\Delta(1232)$ and central short range correlations. The dot dashed line also includes tensor correlations.
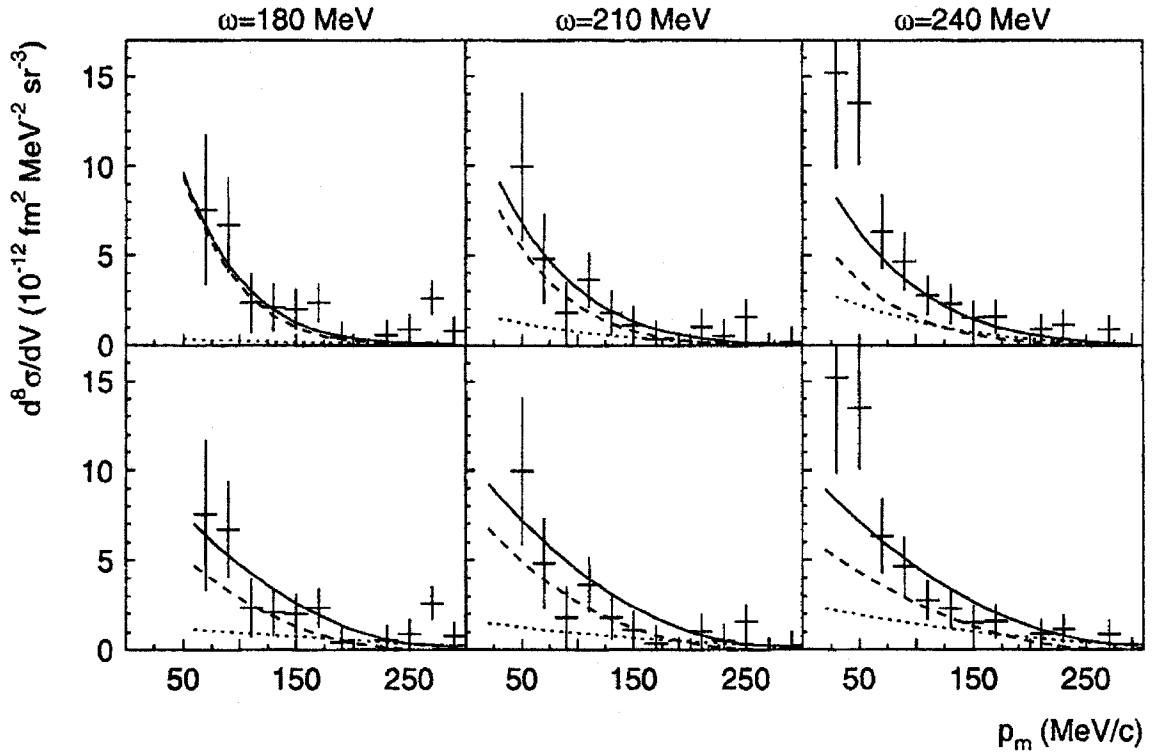
FIG. 5. Cross section for the ^{16}O$(e, e'pp)^{14}$C reaction as a function of missing energy for different missing momenta [18]. Curves on the top plots correspond to the Pavia model [19] and curves on the bottom plots to the Gent model [12]. The solid curves represent the calculated total cross section, dashed and dotted curves correspond to the contribution of the one- and two-body hadronic currents, respectively.

knockout to the ground state of ^{14}C. The momentum distribution reflects an angular momentum $L = 0$ for the center-of-mass motion of the pair, and thus suggests the dominant role for the knockout of a $^1S_0$ pair driven by SRC. The calculations also show the large contribution of two body currents (especially at larger ω) [12].

The phenomena of SRC was also investigated by Groep et $al.$ in the ^{3}He$(e, e'pp)n$ reaction at the Amsterdam Pulse Stretcher ring at NIKHEF [20]. Figure 6 shows the differential cross section for the ^{3}He$(e, e'pp)$ reaction at $\omega = 220$ MeV as a function of different missing momenta ($\mathbf{p}_m = \mathbf{q} - \mathbf{p}_1 - \mathbf{p}_2$). The curve shows the calculations by the Bochum group which include the effect of re-scattering of the outgoing nucleon to all orders and also partially account for the meson exchange currents (MEC) [21]. The ^{3}He calculations do best at lower ω and lower p_{miss}. At higher ω, MEC and IC
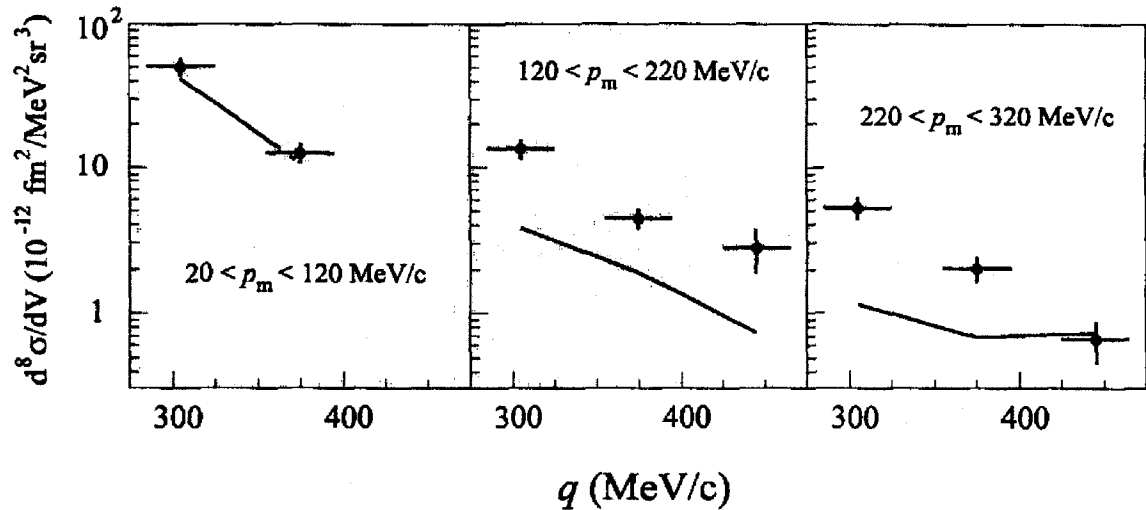
FIG. 6. Differential cross section for the ^{3}He$(e, e'pp)$ reaction at $\omega = 220$ MeV for different missing momenta as a function of momentum transfer [20]. The curve shows the calculations which include the effect of re-scattering of outgoing nucleon to all orders and also accounts for meson exchange currents (MEC) [21].

become more important. The results shows the cross section almost five times higher than the calculation. The calculations are exact if there are no MEC or IC.

Niyazov et $al.$ also measured the ^{3}He$(e, e'pp)n$ reaction at higher energies at Hall-B TJNAF [22] with $E = 2.2$ GeV at $Q^2 \approx 0.8$ GeV^2. They observed that when one nucleon carried most of the kinetic energy, the other two nucleons were emitted predominantly back to back. Figure 7 shows the opening angle of the spectator pair. The peak at 180° indicates the correlation between the pair. The filled dots show the data, the open points show the data with the cut on the momentum of the struck nucleon perpendicular to the virtual photon direction $p_{pp}^{perp} < 0.3$ GeV/c, and the histogram shows the calculated phase space. They concluded that they had measured the joint momentum distribution of a correlated nucleon pair. Figure 114 shows the published relative and total momentum distribution for the correlated pp and pn pair. We will discuss these results further in Chapter 5.

Several major points can be concluded from the previously obtained results:

- $A(e, e')$ ratios show the universality of SRC.

- Previous $(e, e'p)$ measurements showed indirect evidence for SRC.
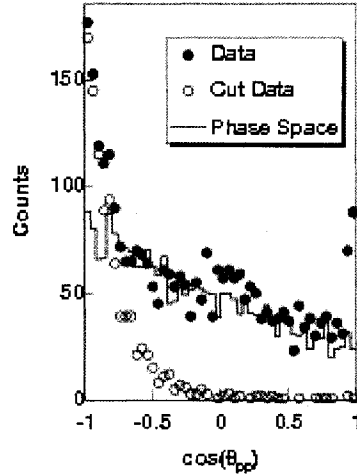
FIG. 7. Cosine of the opening angle of two spectator nucleons in the ^{3}He$(e, e'pp)n$ reaction [22]. Filled dots show the data, open points show the data cut on the momentum of the struck nucleon perpendicular to the virtual photon direction $p_{pp}^{perp} < 0.3$ GeV/c and the histogram shows the phase space.

- Previous $(e, e'pp)$ measurements showed direct evidence for SRC.

- A previous ^{3}He$(e, e'pp)n$ measurement claimed to measure the joint distorted momentum distribution of nucleons in an SRC.

The main goal of this dissertation is to better understand the structure of ^{3}He, including especially the effects of SRC. Toward this end we measured the ^{3}He$(e, e'pp)n$ reaction at $E_{beam} = 4.71$ GeV in the TJNAF CLAS detector. Part of this dissertation focuses on extending the measurements of Niyazov *et al.* to higher momentum transfer and part focuses on exploring other kinematics of the reaction. This will be a good check for the results obtained by Niyazov *et al.*. As the effects of SRC should not depend on momentum transfer, the results for 2.2 and 4.7 GeV beams should be consistent.

Chapter 2 describes some of the theoretical models used to compare to the data. Chapter 3 presents an overview of the experimental setup. The data analysis, calibrations and efficiency calculations are presented in Chapter 4. Final results are presented in Chapter 5.

CHAPTER 2

THEORY INTRODUCTION

2.1 INTRODUCTION TO THE THEORETICAL MODELS

In this chapter we will introduce the theoretical models for later comparison with experimental results. There are several ingredients involved in any calculation of the ^{3}He$(e, e'NN)N$ disintegration cross section:

1. Initial state wave function

2. Virtual photon–nucleus interaction operator

3. Final state wave function

   - rescattering of the struck nucleon

   - reinteraction of the residual nucleons

First we need the correct form of the ^{3}He wave function, which can be obtained by exact solution of the Schrödinger equation, typically using the Faddeev equation or other equivalent methods [2]. Some models use a truncated version of the exact wave function, for calculational simplicity and speed. Different NN potentials and $3N$ forces produce different wave functions. It is important to mention that the NN potentials are not well constrained for $p > 350$ MeV/c.

The operator can be a single nucleon knockout operator, or it can also include two or more nucleon currents, typically through the inclusion of Meson Exchange Currents (MEC) and Isobar Configurations (IC). Figure 8 shows one of each diagram contributing to the MEC and IC processes.

Ideally, the three nucleon final state would also be described exactly. However, that is not possible at these energies. Calculations that ignore the rescattering of the struck nucleon are frequently referred to as "Plane Wave Impulse Approximation"[1].

---

[1]There is significant nomenclature confusion for the ^{3}He$(e, e'pp)n$ reaction. PWIA is sometimes used to refer to the final state where all three nucleons are plane waves (PW) and sometimes to the final state where only the struck nucleon is a PW and the other two are treated precisely.
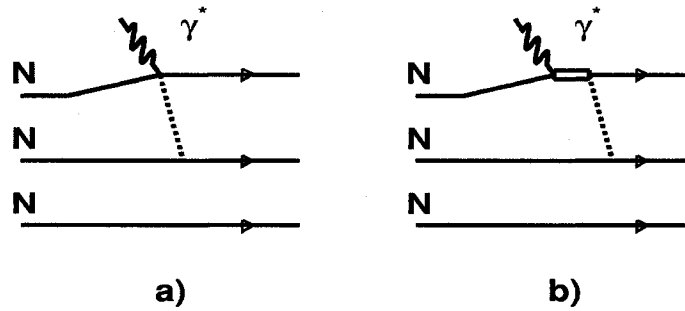
FIG. 8. Examples of two body current operator diagrams. a) one of the contributing MEC diagrams, b) IC diagrams

These calculations can either treat all three nucleons as plane waves or include the low energy interaction of the two residual nucleons.

Rescattering of the struck nucleon at these energies is frequently calculated in the Glauber Approximation. The Glauber approximation treats the nucleons as a diffracting plate. In this approach the remaining nucleons inside of the nucleus are stationary. Another method of calculating the Final State Interaction (FSI) of the struck nucleon is to use the Generalized Eikonal Approximation (GEA). In this approach, the scattering amplitude is expressed through the sum of the diagrams. We will present details of three calculations, a GEA calculation by Sargsian *et al.*, a PWIA calculation that treats the residual nucleus exactly by Golak *et al.*, and a diagrammatic calculation that includes MEC and IC by Laget.

2.2   EXCLUSIVE ELECTRO-DISINTEGRATION OF ^{3}HE AT HIGH Q^2: GENERALIZED EIKONAL APPROXIMATION (GEA)

The calculation done by Sargsian *et al.* [24] uses an exact initial state wave function obtained using the CD-Bonn potential and calculates the FSI of the struck energetic nucleon with the recoil nucleons within the generalized eikonal approximation (GEA). The GEA allows to include the potentially large momenta of the other bound nucleons in the nucleus [24]. The important advantage of this approach, unlike the Glauber Approximation, is the possibility to study in a self-consistent way, the effect of the short range correlations on the final state interaction.

This work includes calculations for the exclusive ^{3}He$(e, e'pp)n$ reactions at high

Q^2 $(1 < Q^2 < 4\,\mathrm{GeV}^2)$ in which one nucleon in the final state can be clearly identified as the knocked-out or leading nucleon which carries practically all of the momentum of the virtual photon. The calculation of the scattering amplitude of this reaction is done within the generalized eikonal approximation (GEA) [25, 26, 27] in which the scattering amplitude expressed through the sum of diagrams corresponding to the nth order re-scattering of the knocked-out nucleon with the residual nucleons in the nucleus. Then each diagram is evaluated based on the effective Feynman diagram rules derived within the GEA [26, 27]. If the probed internal momenta are sufficiently small, $\frac{p^2}{m_N^2} \ll 1$, the non relativistic ground state nuclear wave functions can be used which were calculated based on realistic NN interaction potentials. Furthermore, in quasi-elastic kinematics, the Isobar Current and Meson Exchange contributions were not calculated. These approximations limit the range of validity of the calculation[2].

2.2.1 Reaction and Kinematics

Sargsian's calculation is based on the electro-disintegration of ^{3}He in the reaction ^{3}He$(e, e'pp)n$:

$$e + {}^3\mathrm{He} \rightarrow e' + N_f + N_{r2} + N_{r3} \tag{1}$$

where e and e' are the initial and scattered electrons with four-momenta k_e and k'_e respectively. The ^{3}He nucleus has four-momentum p_A. N_f, N_{r2} and N_{r3} correspond to the leading and two recoil nucleons with four-momenta p_f, p_{r2} and p_{r3} respectively. The four-momentum of the virtual photon is $q = (q_0, \mathbf{q}) \equiv k_e - k_{e'}$ with $Q^2 = -q^2$. Hereafter the z direction is chosen parallel to $\mathbf{q}$ and the scattering plane is the plane of the $\mathbf{q}$ and $\mathbf{k}'_e$ vectors.

The calculation is valid in the following kinematic regime:

$$\text{(a)}\ 1 \leq Q^2 \leq 4\,\mathrm{GeV}^2; \quad \text{(b)}\ \mathbf{p_f} \approx \mathbf{q}; \quad \text{(c)}\ |\mathbf{p_m}|, |\mathbf{p_{r2}}|, |\mathbf{p_{r3}}| \leq 500\,\mathrm{MeV/c}, \tag{2}$$

where the missing momentum is defined as $\mathbf{p_m} = \mathbf{p_f} - \mathbf{q}$. $Q^2 \geq 1\,(\mathrm{GeV/c}^2)^2$ is the lower limit of high-momentum transfer in the electro-disintegration. These conditions allow one to identify N_f as the knocked-out nucleon, while N_{r2} and N_{r3} could be considered as recoil nucleons which might not interact directly with the virtual

---

[2]Relativistic effects were incorporated self-consistently in GEA using the light-cone formalism, see appendix in Ref.[26].

photon. The model requires that $Q^2 \leq 4$ $(\text{GeV}/c^2)^2$ so that color coherence effects are small and the produced hadronic state represents a single state (i.e., a nucleon) rather than a superposition of different hadronic states in the form of a wave packet (see e.g. Ref.[32]). Additionally, the requirement of $|\mathbf{p_m}|, |\mathbf{p_{r2}}|, |\mathbf{p_{r3}}| \leq 500$ MeV/c allows one to consider the nucleons as the basic degrees of freedom in describing the interacting nuclear system.

The following three sections describe the three different approximations calculated by Sargsian.

2.2.2 Plain Wave Impulse Approximation

The contribution to the electromagnetic transition amplitude A^μ, in which the knocked out nucleon does not interact with the other nucleons, corresponds to the plain wave impulse approximation (PWIA). In this case the wave function of the knocked out nucleon is a plane wave.

The IA term of the scattering amplitude, A_0^μ, is described by the Feynman diagram of Figure 9 and equal to:
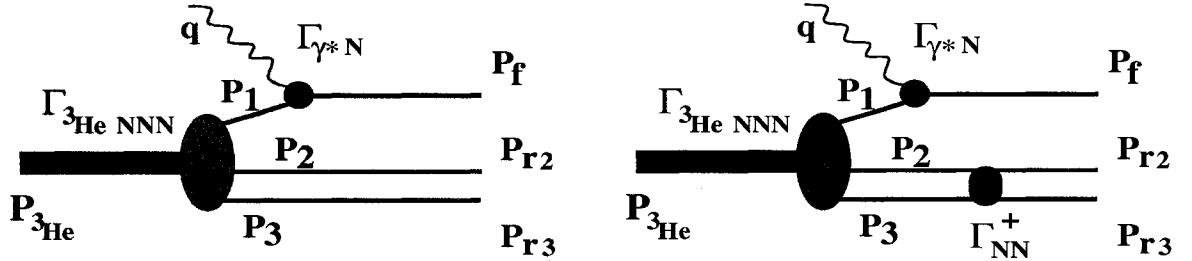
FIG. 9. PWIA and DWIA contribution to the scattering amplitude of $^3\text{He}(e, e'N_fN_{r2})N_{r3}$ reaction. a) Plain Wave Impulse Approximation b) Pair distortion.

$$A_0^\mu = -\int \frac{d^4p_2}{i(2\pi)^4} \bar{u}(p_{r2})\bar{u}(p_{r3})\bar{u}(p_f) \cdot \Gamma_{NN}^+(p_2, p_3) \cdot \Gamma_{\gamma^*N}^\mu \cdot \frac{\vec{p_3} + m}{p_3^2 - m^2 + i\varepsilon} \times$$

$$\times \frac{\vec{p_2} + m}{p_2^2 - m^2 + i\varepsilon} \cdot \frac{\vec{p_1} + m}{p_1^2 - m^2 + i\varepsilon} \cdot \Gamma_{3\text{He}NNN}(p_1, p_2, p_3) \, \chi^A, \tag{3}$$

where $\mathbf{p_1} = \mathbf{p_m} \equiv \mathbf{p_f} - \mathbf{q}$ and $|\vec{p_3}| = |\vec{p_A} - \vec{p_1} - \vec{p_2}|$, $\Gamma_{NN}^+(p_2, p_3)$ is the vertex function describing the transition from $(A-1)$ nucleons to $(A-1)$ nucleons final state,

$\Gamma_{^3\mathrm{He}NNN}(p_1, p_2, p_3)$ is the vertex function describing the transition from ^{3}He to $3N$ nucleon final state and $\Gamma^\mu_{\gamma^* N}$ is the vertex for the $\gamma^* N$ interaction. For nucleon momenta $p_i < 500$ MeV/c it can be integrated over dp_2^0, estimating it through the residue at the positive energy pole of the propagator of nucleon "2". This corresponds to the positive energy projection of the virtual nucleon state. Such integration effectively corresponds to the replacement:

$$\int \frac{dp_2^0}{p_2^2 - m^2 + i\varepsilon} = -\frac{i2\pi}{2E_2} \approx -\frac{i2\pi}{2m}. \tag{4}$$

The condition that the internal momenta of the nucleons remain small ($\mathbf{p}^2_{m,2,3} \ll m^2$) also allows one to use the closure relation for on-mass shell nucleons to express the numerator of the bound nucleon propagator as follows:

$$\vec{p} + m = \sum_s u(p, s)\bar{u}(p, s). \tag{5}$$

Using Eq. (4) and (5) in Eq. (3) one obtains:

$$
\begin{aligned}
A_0^\mu &= \sqrt{2E_{r2}2E_{r3}}(2\pi)^3 \sum_{s_1, s_2, s_3, t_2, t_3} \int d^3 p_2 \Psi_{NN}^{\dagger p_{r2}, s_{r2}, t_{r2}; p_{r3}, s_{r3}, t_{r3}}(p_2, s_2, t_2; p_3, s_3, t_3) \\
&\quad \times j_{t1}^\mu(p_m + q, s_f; p_m, s_1)\Psi_A^{s_A}(p_m, s_1, t_1; p_2, s_2, t_2; p_3, s_3, t_3),
\end{aligned} \tag{6}
$$

where $s_A, s_1, s_2, s_3, s_f, s_{r2}, s_{r3}$ describe the spin projections of the ^{3}He-nucleus, the initial nucleons and the final nucleons respectively. The isospin projections of nucleons are represented by $t_1, t_2, t_3, t_f, t_{r2}, t_{r3}$ and use these indexes to identify the protons and neutrons. In the above equation, $\Psi_A^{s_A}$ is the ground state wave function of the ^{3}He nucleus with polarization vector $\mathbf{s_A}$ and Ψ_{NN} represents the bound or continuum NN wave function. One can further simplify Eq. (6) using the fact that Ψ_{NN} is a function only of the relative three-momenta of spectator nucleons and the spins. This allows one to replace the $d^3 p_2$ integration by $d^3 p_{23}$ ($\mathbf{p_{23}} = (\mathbf{p_2} - \mathbf{p_3})/2$ and $\mathbf{P_{cm23}} = \mathbf{p_2} + \mathbf{p_3}$) which yields

$$
\begin{aligned}
A_0^\mu &= \sqrt{2E_{r2}2E_{r3}}(2\pi)^3 \sum_{s_1, s_2, s_3, t_2, t_3} \int d^3 p_{23} \Psi_{NN}^{\dagger p_{r23}, s_{r2}, t_{r2}; s_{r3}, t_{r3}}(p_{23}, s_2, t_2; s_3, t_3) \\
&\quad \times j_{t1}^\mu(p_m + q, s_f; p_m, s_1)\Psi_A^{s_A}\left(p_m, s_1, t_1; -\frac{p_m}{2} + p_{23}, s_2, t_2; -\frac{p_m}{2} - p_{23}, s_3, t_3\right).
\end{aligned} \tag{7}
$$

For the case of the reaction of ^{3}He$(e, e'pp)n$, Ψ_{NN} is a continuum NN wave function which can be represented through the Lippmann-Schwinger equation as follows:

$$\Psi_{NN}^{\dagger p_{r23}, s_{r2}, t_{r2}; s_{r3}, t_{r3}}(p_{23}, s_2, t_2; s_3, t_3) = \delta^3(\mathbf{p_{23}} - \mathbf{p_{r23}}) +$$

$$\frac{1}{2\pi^2} \frac{\langle s_{r2}, t_{r2}; s_{r3}, t_{r3} \mid f_{NN}^{\text{off shell}}(\mathbf{p_{r23}}, \mathbf{p_{23}}) \mid s_2, t_2; s_3, t_3 \rangle}{\mathbf{p_{23}}^2 - \mathbf{p_{r23}}^2 - i\varepsilon}, \tag{8}$$

where $\mathbf{p_{23}} = \frac{\mathbf{p_2} - \mathbf{p_3}}{2}$, $\mathbf{p_{r23}} = \frac{\mathbf{p_{r2}} - \mathbf{p_{r3}}}{2}$ and $f_{NN}^{\text{off shell}}$ is a half-off-shell non-relativistic amplitude of NN scattering (see e.g. Ref.[28]). Terms on the right-hand side of Eq. (8) characterize two distinctive dynamics of production of the recoil NN state. If only the first term of Eq. (8) is kept in Eq. (7), this will correspond to the approximation in which all three final nucleons propagate as plane waves. Hereafter we will refer to this approximation as the plane wave impulse approximation (PWIA) (see Figure 9(a)). The second term in Eq. (8) describes a re-interaction between the pair of slow nucleons which distorts the plane wave of the outgoing recoil nucleons (see Figure 9(b)). The Γ_{NN}^+ term is responsible for the Pair Distortion (PD) strength. This approximation we will call Plane Wave Impulse Approximation with Pair Distortion (PWIA+PD). The pair distortion calculations were done by using SAID group's parametrization of low-to-intermediate energy [29] NN scattering amplitudes as well as a new parametrization of the high-energy small-angle NN scattering amplitude [30].

2.2.3 Single re-scattering amplitude

The diagrams in Figure 10 describe the process in which the knocked-out (fast) nucleon re-scatters off one of the spectator nucleons. The amplitude corresponding to the diagram of Figure 10(a) is:

$$A_{1a}^\mu = -\frac{F}{2} \sum_{s_1, s_2, s_3} \sum_{t_1, t_{2'}, t_2, t_3} \int \frac{d^3k}{(2\pi)^3} d^3 p_3 \Psi_{NN}^{\dagger p_{r2}, s_{r2}, t_{r2}; p_{r3}, s_{r3}, t_{r3}}(p_2', s_2, t_{2'}; p_3, s_3, t_3) \times$$

$$\times \frac{\chi_1(s_2^{NN}) f_{NN}^{t_{2'}, t_f | t_2, t_1}(k_\perp)}{\Delta^0 - k_z + i\varepsilon} \times$$

$$\times j_{t_1}^\mu(p_1 + q, s_f; p_1, s_1) \cdot \Psi_A^{s_A}(p_m + k, s_1, t_1; p_2, s_2, t_2; p_3, s_3, t_3),$$

$$\tag{9}$$
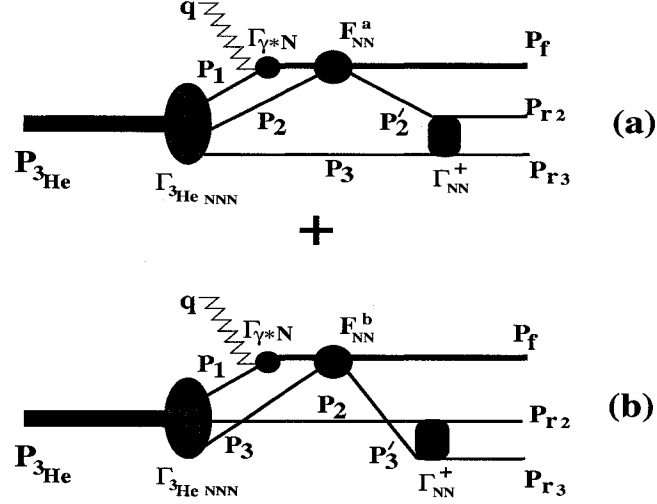
FIG. 10. Single re-scattering contribution to the scattering amplitude of $^3\mathrm{He}(e, e'N_fN_{r2})N_{r3}$ reaction. F_{NN}^a and F_{NN}^b are hard rescattering operators and Γ_{NN}^+ accounts for the Pair Distortion.

where $\chi_1(s_2^{NN}) = \frac{\sqrt{s_2^{NN}(s_2^{NN}-4m^2)}}{2qm}$ and $F = \sqrt{2E_{r2}2E_{r3}}(2\pi)^3$, $p_1 = p_A - p_2 - p_3$, $p_2' = p_{r2} + p_{r3} - p_3$ and $s_2^{NN} = (p_1 + q + p_2)^2$.

The contribution of the second diagram in Figure 10 can be calculated by interchanging the momenta of the "2" and "3" nucleons in Eq. (9). Doing this and changing the integration variables d^3p_3 to d^3p_{23} (similar to Section 2.2.2), for the complete single re-scattering amplitude one obtains:

$$
\begin{aligned}
A_1^\mu &= A_{1a}^\mu + A_{1b}^\mu \\
&= -\frac{F}{2} \sum_{s_1,s_2,s_3} \sum_{t_2't_3'} \sum_{t_1,t_2t_3} \int \frac{d^3k\,d^3p_{23}}{(2\pi)^3} \Psi_{NN}^{\dagger p_{r23},s_{r2},t_{r2};s_{r3},t_{r3}}(p_{23},s_2,t_{2'};s_3,t_{3'}) \\
&\quad \times j_{t_1}^\mu(p_1+q,s_f;p_1,s_1)[\frac{\chi_1(s_2^{NN})f_{NN}^{t_f,t_{2'}|t_1,t_2}(k_\perp)\delta^{t_{3'},t_3}}{\Delta^0 - k_z + i\varepsilon} \times \\
&\quad \times \Psi_A^{s_A}(p_m + k, s_1, t_1; -\frac{p_m}{2} + p_{23} - k, s_2, t_2; -\frac{p_m}{2} - p_{23}; s_3, t_3) + \\
&\quad + \frac{\chi_1(s_3^{NN})f_{NN}^{t_f,t_{3'}|t_1,t_3}(k_\perp)\delta^{t_{2'},t_2}}{\Delta^0 - k_z + i\varepsilon} \times \\
&\quad \times \Psi_A^{s_A}(p_m + k, s_1, t_1; -\frac{p_m}{2} + p_{23}, s_2, t_2; -\frac{p_m}{2} - p_{23} - k; s_3, t_3)].
\end{aligned}
\tag{10}
$$
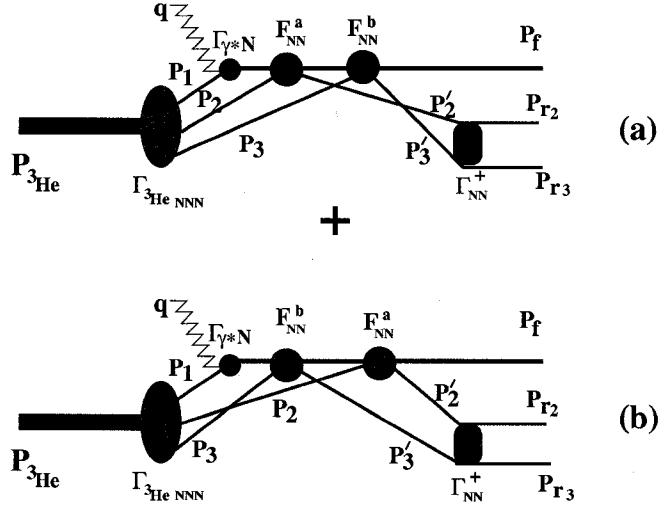
FIG. 11. Double rescattering contribution to the scattering amplitude of the $^3\text{He}(e, e'N_f N_{r2})N_{r3}$ reaction.

2.2.4 Double rescattering amplitude

Figure 11 shows the diagrams corresponding to double rescattering (in which knocked-out nucleon re-scatters off both spectator nucleons in the nucleus). The amplitude corresponding to the diagram of Figure 11(a) is:

$$
\begin{aligned}
A^\mu_{2a} &= \frac{F}{4} \sum_{s_1,s_2,s_3} \sum_{t_j,t_{i'}} \int \frac{d^3p'_3}{(2\pi)^3} \frac{d^3p_2}{(2\pi)^3} d^3p_3 \, \Psi_{NN}^{\dagger p_{r2},s_{r2},t_{r2};p_{r3},s_{r3},t_{r3}}(p'_2, s_2, t_{2'}; p'_3, s_3, t_{3'}) \times \\
&\times \frac{\chi_2(s^{NN}_{b3}) f_{NN}^{t_{3'},t_f|t_3,t_{1'}}(p'_{3\perp} - p_{3\perp}) \, \chi_1(s^{NN}_{a2}) f_{NN}^{t_{2'},t_{1'}|t_2,t_1}(p'_{2\perp} - p_{2\perp})}{\Delta_3 + p'_{3z} - p_{3z} + i\varepsilon \quad \Delta^0 + p_{mz} - p_{1z} + i\varepsilon} \\
&\times j^\mu_{t1}(p_1 + q, s_f; p_1, s_1) \cdot \Psi^{sA}_A(p_1, s_1, t_1; p_2, s_2, t_2; p_3, s_3, t_3),
\end{aligned}
\tag{11}
$$

where $\chi_1(s^{NN}_{a2}) = \frac{\sqrt{s^{NN}_{a2}(s^{NN}_{a2} - 4m^2)}}{2qm}$ with $s^{NN}_{a2} = (p_1 + q + p_2)^2$ and $\chi_2(s^{NN}_{b3}) = \frac{\sqrt{s^{NN}_{b3}(s^{NN}_{b3} - 4m^2)}}{2p_{fz}m}$ with $s^{NN}_{b3} = (p_1 + q + p_2 - p'_2 + p_3)^2$.

This amplitude corresponding to the diagram of Figure 11(b) is obtained by interchanging momenta of nucleons "2" and "3" in Eq.(11). If $k_2 = p'_2 - p_2$ and $k_3 = p'_3 - p_3$ then changing the $d^3p'_3$ integration to $d^3p'_{23}$ obtained result is:

$$
A^\mu_2 = A^\mu_{2a} + A^\mu_{2b} =
$$

$$\frac{F}{4} \sum_{s_1,s_2,s_3} \sum_{t_1,t_2,t_3,t_{1'},t_{2'},t_{3'}} \int d^3 p'_{23} \frac{d^3 k_3}{(2\pi)^3} \frac{d^3 k_2}{(2\pi)^3} \Psi_{NN}^{\dagger p_{r23},s_{r2},t_{r2};s_{r3},t_{r3}} (p'_{23}, s_2, t_{2'}; s_3, t_{3'})$$

$$\times \left[\frac{\chi_2(s_{b3}^{NN}) f_{NN}^{t_{3'},t_f|t_3,t_{1'}}(k_{3\perp})}{\Delta_3 - k_{3z} + i\varepsilon} \frac{\chi_1(s_{a2}^{NN}) f_{NN}^{t_{2'},t_{1'}|t_2,t_1}(k_{2\perp})}{\Delta^0 - k_{2z} - k_{3z} + i\varepsilon} + \right.$$

$$\left. \frac{\chi_2(s_{b2}^{NN}) f_{NN}^{t_{2'},t_f|t_2,t_{1'}}(k_{2\perp})}{\Delta_2 - k_{2z} + i\varepsilon} \frac{\chi_1(s_{a3}^{NN}) f_{NN}^{t_{3'},t_{1'}|t_3,t_1}(k_{3\perp})}{\Delta^0 - k_{2z} - k_{3z} + i\varepsilon} \right] \times$$

$$\times j_{t1}^{\mu}(p_m + k_2 + k_3 + q, s_f; p_m + k_2 + k_3, s_1)$$

$$\times \Psi_A^{s_A}(p_m + k_3 + k_2, s_1, t_1; -\frac{p_m}{2} - k_2 + p'_{23}, s_2, t_2; -\frac{p_m}{2} - k_3 - p'_{23}, s_3, t_3). \quad (12)$$

2.2.5 Differential Cross Section

The calculated amplitudes allow one to evaluate observables (both polarized and unpolarized) for the high Q^2 quasi-elastic electro-production from ^{3}He. The ^{3}He$(e, e'pp)n$ differential cross section is given by

$$d^{12}\sigma = \frac{1}{4j_A}(2\pi)^4 \delta^4(k_e + P_A - k'_e - p_f - p_{r2} - p_{r3}) \sum_{nucleons} |M_{fi}|^2$$

$$\frac{d^3 k'_e}{(2\pi)^3 2E'_e} \frac{d^3 p_f}{(2\pi)^3 2E_f} \frac{d^3 p_{r2}}{(2\pi)^3 2E_{r2}} \frac{d^3 p_{r3}}{(2\pi)^3 2E_{r3}}, \quad (13)$$

where $j_A = \sqrt{(k_e P_A)^2 - m_e^2 M_A^2}$. Here we sum over the nucleons knocked-out by the virtual photon. The factor of $1/4$ comes from averaging over the initial polarizations of the electron and ^{3}He. Thus the integrated differential cross section is

$$d^9\sigma = \frac{1}{4j_A}(2\pi)^4 \delta(E_e + M_A - E'_e - E_f - E_{r2} - E_{r3}) \sum_{nucleons} |M_{fi}|^2$$

$$\frac{d^3 k'_e}{(2\pi)^3 2E'_e} \frac{d^3 p_f}{(2\pi)^3 2E_f} \frac{d^3 p_{r2}}{(2\pi)^3 2E_{r2}} \frac{1}{(2\pi)^3 2E_{r3}}, \quad (14)$$

where $\mathbf{p_{r3}} = \mathbf{k_e} - \mathbf{k'_e} - \mathbf{p_f} - \mathbf{p_{r2}}$. In Eqs. (13) and (14) the transition matrix, M_{fi}, represents the convolution of the electron and nuclear currents, in which the nuclear current represents the sum of the IA, single and double rescattering amplitudes,

$$M_{fi} = -4\pi\alpha \frac{1}{q^2} j_\mu^e \cdot \left(A_0^\mu + A_1^\mu + A_2^\mu\right), \quad (15)$$

where A_0, A_1 and A_2 are defined in Eqs. (7), (10) and (12) respectively.

2.2.6 Summary

This theoretical framework for Sargsian's calculation of high Q^2 exclusive electro-disintegration of the $A = 3$ system can be used to account for the finite and relatively large momenta of the recoil nucleons.

2.3 ELECTRON SCATTERING ON ^{3}HE

The calculation by Golak *et al.* presented in this section treats the single nucleon knock out relativistically and the residual NN interaction is complete to all orders.

The central quantities in the description of electron induced processes are the nuclear matrix elements:

$$N^\mu \equiv \langle \Psi_f^{(-)} \mid j^\mu(\mathbf{q}) \mid \Psi_{^3\mathrm{He}}^{\theta^* \phi^*} \rangle. \tag{16}$$

They are composed of the polarized ^{3}He target state, the components $j_\mu(\mathbf{q})$ of the current operator and the final $3N$ scattering state $\langle \Psi_f^{(-)} \mid$ with asymptotic momenta and spin quantum numbers f. For proton-deuteron (pd) breakup, these are the proton and deuteron momenta and their spin magnetic quantum numbers, and for the three nucleon breakup these are the three final nucleon momenta and again their spin magnetic quantum numbers. The initial ^{3}He spin direction is determined by the angle θ^* with respect to the photon momentum $\mathbf{q}$ and by the azimuthal angle ϕ^* in relation to the scattering plane formed by the initial and final electron momenta.

The ^{3}He state is a solution [38] of the Faddeev equation

$$\psi = G_0 t P \psi + G_0(1 + tG_0)V_4^{(1)}(1 + P)\psi, \tag{17}$$

where the Faddeev component ψ determines the full state via

$$\Psi_{^3\mathrm{He}} = (1 + P)\psi. \tag{18}$$

The ingredients are the free $3N$ propagator G_0, the NN t-operator generated via the Lippmann-Schwinger equation from any modern NN interaction and a suitably chosen permutation operator P [39]. Further $V_4^{(1)}$ is one of the three parts of a $3N$ force into which any $3NF$ can be decomposed. We assume here that the t-operator acts on the pair 23 and that $V_4^{(1)}$ is the part of the three-nucleon force which is symmetrical under exchange of particles 2 and 3.

This leads to the nuclear matrix element

$$N^\mu = \langle \psi_f \mid U^\mu \rangle, \tag{19}$$

where the auxiliary state $\mid U^\mu \rangle$ obeys the Faddeev-like integral equation

$$
\begin{aligned}
\mid U^\mu \rangle &= (1+P)j^\mu(\mathbf{q}) \mid \Psi_{^3\text{He}} \rangle \\
&+ PtG_0 \mid U^\mu \rangle + (1+P)V_4^{(1)}G_0(tG_0+1) \mid U^\mu \rangle.
\end{aligned} \tag{20}
$$

$|\psi_f\rangle$ is a known channel-dependent state, which for the complete three-body breakup is given as $|\psi_f^{3N}\rangle = (1 + G_0 t)|\phi_0\rangle$, with $|\phi_0\rangle$ being plane waves, antisymmetrized in the two-body subsystem, where t acts.

In general the series shown in Figure 12 converges very slowly or even diverges [40, 41]. Therefore it is important to rely on the full solution of Eq. (20), which also guarantees that $\langle \Psi_f^{(-)}|$ and $|\Psi_{^3\text{He}}\rangle$ are consistent solutions to the same 3N Hamiltonian.

The standard non-relativistic single nucleon piece and two-body currents of the $\pi-$ and $\rho-$ exchange type related to the AV18 NN force [35] [36] are used as the current operator. In the case of elastic electron scattering on ^{3}He, the seagull terms from [37] are used.

This calculation treats the initial state and the two slow final state nucleons exactly. The struck nucleon is treated as a plane wave (i.e., struck nucleon rescattering is ignored). Thus, this calculation is optimal for kinematics where struck nucleon rescattering is negligible.

2.4 DIAGRAMMATIC APPROACH

We also compared our data with the theoretical calculations by J. M. Laget [31] performed in the Diagrammatic Approach. The initial state wave function is taken as the solution to the Faddeev equation with the Paris potential and the continuum was approximated by the sum of a plane wave and half-off-shell scattering amplitudes, where two nucleons scatter and the third is a spectator. Additionally, the two and three body MEC were considered. The SRC effect is included in the initial state wave function. FSI was included as the sum of several rescattering diagrams. Figure 13 shows several diagrams used for the calculations in the Diagrammatic Approach.
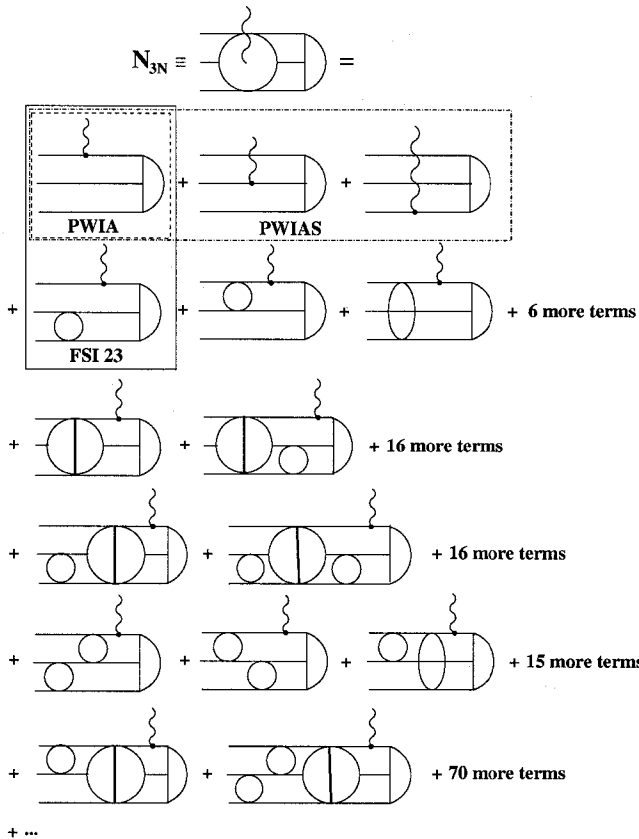
FIG. 12. Diagrammatic representation of the nuclear matrix element for the three–body electrodisintegration of ^{3}He. The open circles and ovals represent the two-body t-matrices. The big circles with a vertical line denote the action of $V_4^{(1)}$. The horizontal lines describe free propagation between interactions. The half-moon symbol on the very right side stands for the ^{3}He bound state.

2.5 SUMMARY

In this dissertation we will compare the experimental results with several theoretical models. Table I presents the models, the effects and the approximations which are included in the calculations. Golak 1 and Sarg PWIA treat all three nucleons as Plane Waves. Golak FULL calculations include the exact continuum state wave function. Note that Golak FULL is just PWIA+PD. The calculations of Sarg PWIA+PD include the SAID group's parametrization of low-to-intermediate energy [29] NN scattering amplitudes. Sarg Full also includes a new parametrization of the high energy small angle NN scattering amplitude [30] via GEA. Laget FULL
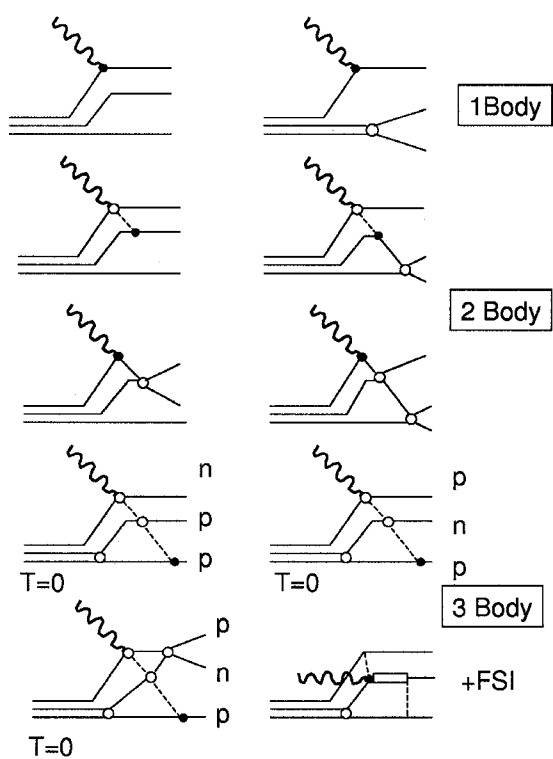
FIG. 13. Diagrams used in Diagrammatic Approach by J. M. Laget [31] for the three-body electrodisintegration of ^{3}He.

calculation includes Meson Exchange Currents and Single Rescattering Amplitudes.

TABLE I. The models used for the comparison with experimental results. BS – Bound State, FS – Final State, WF – Wave Function, PW – Plane Wave. FSI refers to the struck nucleon FSI, Diag refers to the diagrammatic approach.

Model	Wave Function	BS WF NN potential	slow NN FS WF	MEC	FSI
Golak 1	Exact	AV18	PW	None	None
Golak FULL	Exact	AV18	Exact	None	None
Sarg PWIA	Exact	CD-Bonn	PW	None	None
Sarg PWIA+PD	Exact	CD-Bonn	PW+SAID	None	None
Sarg FULL	Exact	CD-Bonn	PW+SAID	None	GEA
Laget PWIA+PD	Truncated	Paris	Approx	None	None
Laget FULL	Truncated	Paris	Approx	Diag	Diag

CHAPTER 3

EXPERIMENTAL SETUP

3.1 CONTINUOUS ELECTRON BEAM ACCELERATOR FACILITY

The experiment has been carried out using the electron beam provided by the Continuous Electron Beam Accelerator Facility (CEBAF) at Jefferson Lab (TJNAF). Its electron accelerator is based on 338 superconducting cavities that boost the beam with radio-frequency waves and provide a high luminosity continuous electron beam with energy up to almost 6 GeV. A schematic of the machine is shown in Fig. 14. The 67 MeV injector delivers polarized electrons from a strained GaAs photocathode source. The beam has a 1.497 GHz micro bunch structure. The beam from the injector is accelerated through a unique recirculating beam-line that looks like a racetrack, with two linear accelerators joined by two 180° arcs with a radius of 80 meters. Twenty cryomodules, each containing eight superconducting niobium cavities, line the two linear accelerators. Accelerating cavities are cooled to 2 Kelvin by liquid helium, produced at the Lab's Central Helium Liquefier. The two parallel linacs recirculate the beam up to five times boosting the beam energy up to 1.2 GeV for each turn. Presently, the maximum beam energy is 5.6 GeV, with a maximum current of 180 μA. Quadrupole and dipole magnets in the tunnel steer and focus the beam as it passes through each arc. More than 2,200 magnets are necessary to keep the beam on a precise path and tightly focused. The energy spread of the beam is $\Delta E/E < 10^{-4}$. Beam is directed into each experimental hall's transport channel using magnetic or RF extraction. The RF scheme uses 499 MHz cavities, which kick every third bunch out of the machine. Beam is delivered into three experimental areas (Hall A, B and C) with one beam "bucket" every 2 ns.

3.2 HALL-B BEAM-LINE

The electron beam delivered to Hall-B is monitored by several devices. Three nanoamp (nA) beam position monitors measure current and position of the beam in real-time with resolution better than 100 μm. A "harp" is located upstream from the center of the CLAS detector to measure the beam distribution. The acceptable
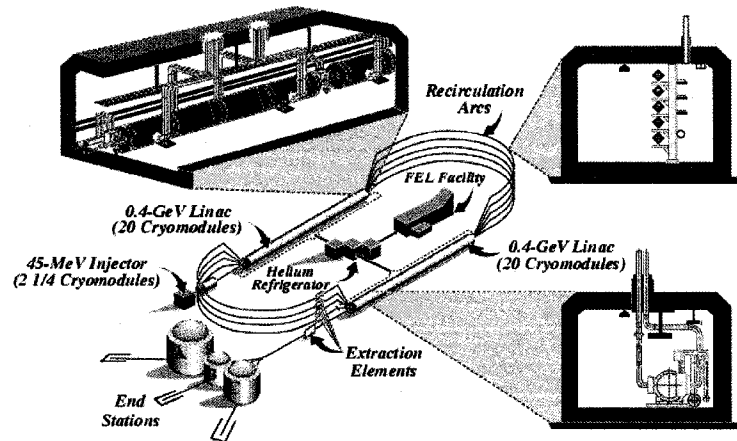
FIG. 14. A schematic view of the accelerator. One of the cryomodules is shown in the upper left corner. A vertical cross section of a cryomodule is shown in the lower right corner. A cross section of the five recirculation arcs is shown in the upper right corner.

width of the beam is typically less than 200 μm.

At the very end of the beam line, the Faraday cup (FC) measures the accumulated charge. The FC is made of 4 tons of lead and is 70 radiation lengths deep. The electron beam stops in the FC. The accumulated charge is measured and recorded for use in calculating cross sections.

3.3 CEBAF LARGE ACCEPTANCE SPECTROMETER, HALL B

CLAS (CEBAF Large Acceptance Spectrometer) is located in Hall B, Jefferson Lab. The CLAS is an almost 4π spectrometer. It provides a unique facility to investigate reaction mechanisms involved in inelastic electron scattering by allowing us to detect almost all of the particles emitted following virtual photon absorption. The magnetic field in the CLAS is generated by six superconducting coils arranged around the beam line to produce a field oriented primarily in the azimuthal direction about the beam axis, with maximum magnitude of about 2 Tesla (see Figure 15). The coils divide the detection system into six independent sectors. Each sector essentially acts as an independent spectrometer. The size and the shape of the coils (about 5 m long and 2.5 m wide) were chosen to optimize measurements with fixed
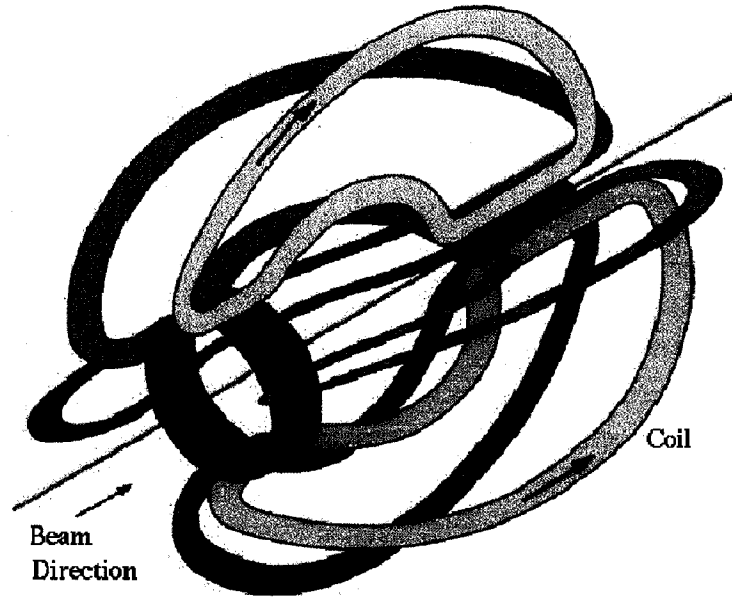
FIG. 15. Configuration of the torus coils.

targets. Each sector of the CLAS consists of three separate Drift Chamber (DC) assemblies to determine the trajectories and momenta of charged particles, Čerenkov Counters (CC) for electron identification, Scintillation Counters (SC) for time-of-flight (TOF) measurements, and an Electromagnetic Shower Calorimeter (EC) to identify showering particles such as electrons and photons and to detect neutrons (see Figure 16). A Faraday cup, located at the very end of the Hall-B beam line, is used to measure the integrated beam charge passing through the target. All detectors may be used to build the trigger configuration for the reaction of interest. The EC system coverage is extended by the Large Angle Calorimeter (LAC). The polar angle coverage in CLAS varies as 8° to 140° for the DC, 9° to 143° for the SC, and 8° to 45° for the CC and EC. The LAC accepts particles from 45° to 75° in two sectors. The next sections describe the individual detectors.

3.3.1 Drift Chambers.

The trajectories and momenta of the charged particles are measured by the drift chambers [44].

The drift chamber system is divided into six sectors by the six superconducting
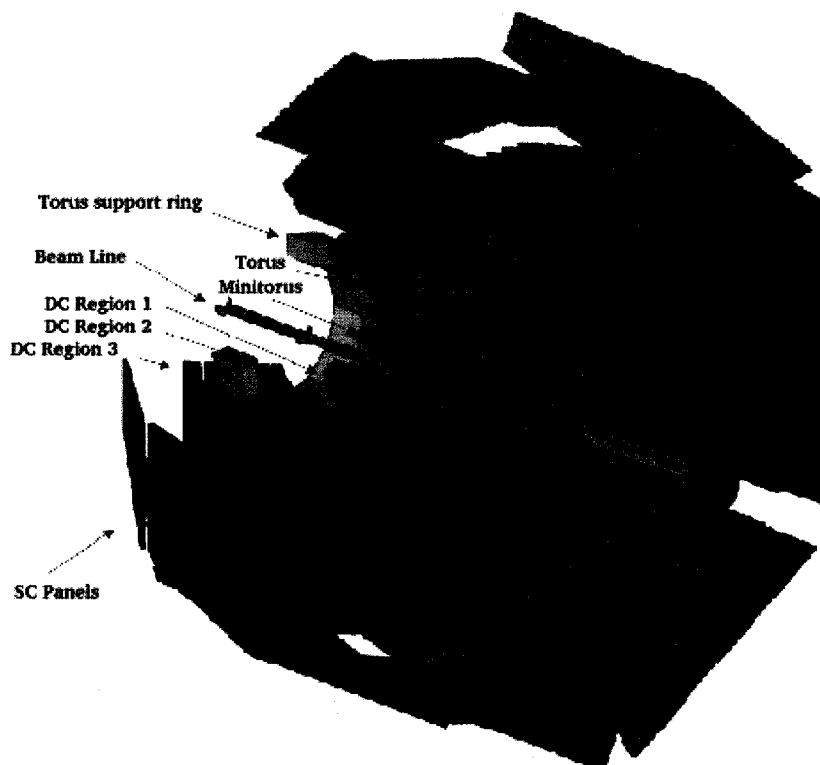
FIG. 16. Three dimensional view of CLAS.

toroidal magnets (Figure 15). The coils create a field free region around the target and a magnetic field that is primarily transverse to the particle trajectory. Each of the six sectors of the drift chambers consists of three separate regions: Region 1 close to the target (no magnetic field), Region 2 between the coils (high magnetic field up to 2 Tesla), and Region 3 outside of the coils (see Figures 15 and 16). The Region 2 drift chambers were built by the experimental nuclear physics group at ODU. Each region of the drift chambers consists of axial and stereo layers of wires. Axial wires are strung parallel to the direction of the magnetic field (perpendicular to the beam direction) to measure scattering angles and momenta. Stereo wires are strung at an angle of 6° with respect to the axial wires. The axial-stereo combination in each region allows us to determine the azimuthal angle ϕ of each particle. Each superlayer consists of six layers of sense wires, surrounded by field wires in hexagonal
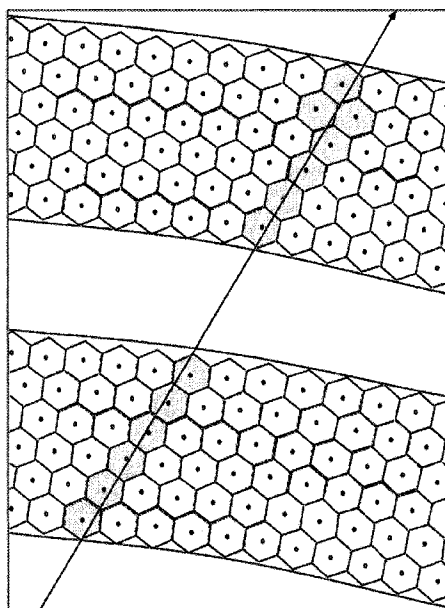
FIG. 17. Schematic of a section of drift chambers showing two super-layers. The wires are arranged in hexagonal patterns (cells). The sense wires are located in the center and field wires are located at each corner of each cell. The arrow shows a charged particle passing through the drift chambers and the shadowed hexagons represent the hit cells.

cells (see Figure 17)[1]. There are 192 sense wires per layer in Regions 2 and 3 and 128 sense wires per layer in Region 1. The total of 18 drift chambers with 35148 instrumented hexagonal drift cells can detect charged particles with momenta greater than 200 MeV/c over the polar angle range from 8° to 143°. There are also guard wires surrounding each superlayer to reproduce the electric field configuration of an infinite number of cells.

Charged particles traversing the drift chamber ionize gas molecules. The gas is maintained in an electric field so that the electrons and ions created in the ionization process drift toward the cathode (sense) and anode (field) wires, respectively. In the high field region near the cathode wires, drifting electrons collide with gas atoms and produce secondary ionization resulting in a multiplication of collected electrons and ions. Detected electric signals carry information about the particle's drift time which translates to the hit position of the original charged particle going through the detector. The electric signal passes through a preamplifier, an amplifier, a discriminator and 2:1 multiplexer and then starts a TDC. The TDCs are stopped by the event trigger. More details on the DC and their calibration are given in Section 4.1.

The drift chamber system uses an Ar/CO_2 gas mixture, 90/10 by volume, which has an ionization gain of $\approx 10^4$. That mixture is non-flammable, and it provides drift velocities of typically 4 cm/μsec and an operational voltage plateau of several hundred volts before breakdown. The intrinsic resolution provided by this gas is ≈ 100 μm [45]. The final spatial resolution is ≈ 400 μm, mostly limited by the knowledge of the geometry and the quality of the drift velocity parametrization.

3.3.2 Čerenkov Counters

The threshold Čerenkov Counters (CC) are designed to discriminate between electrons and hadrons, mostly negative pions, at the trigger level [46]. Charged particles traveling through the medium with a speed exceeding the local phase velocity of light emit electromagnetic radiation. The velocity threshold for Čerenkov light emission is $\beta=1/n$ where n is the refraction index of the medium. The Čerenkov material used is perfluorobutane C_4F_{10}, which has $n=1.00153$. That corresponds to

---

[1]Actually, the first (stereo) superlayer in Region 1 has only 4 layers of sense wires.
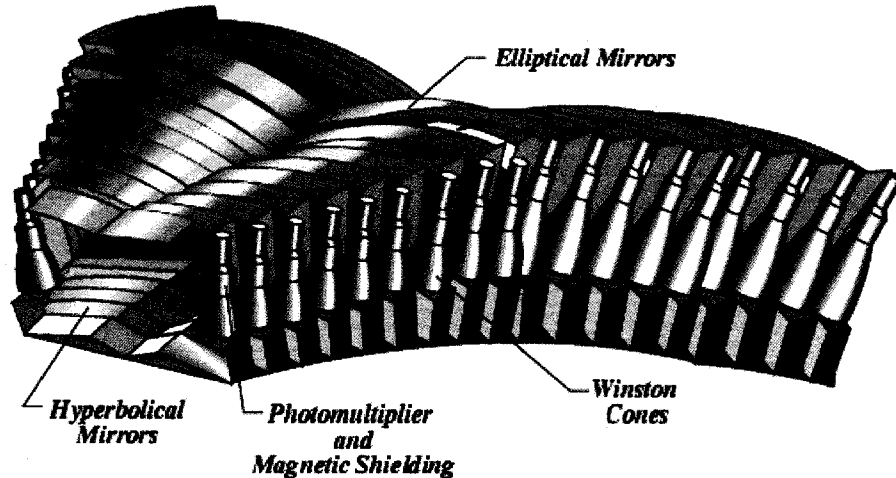
FIG. 18. Array of CC optical modules in one sector.

a threshold in energy of the particle:

$$E = \frac{m}{\sqrt{1 - \beta^2}} = \sqrt{\frac{n}{n-1}}\, m = 18.09 \ m,$$

where m is a mass of the particle. This provides an acceptably high pion momentum threshold ($p_\pi > 2.5$ GeV/c).

The Čerenkov detector of CLAS consists of six independent identical Čerenkov detectors (one per sector) and each detector covers a scattering angle θ from 8° to 45°. Each detector consists of 36 optical modules (see Figure 18) to cover 18 regions of θ, with two modules per θ region.

Each module has three mirrors - elliptical, hyperbolic and cylindrical - to direct the light into a light collecting Winston cone (see Figure 19). The mirrors are aligned to optimize the light collection by PMTs.

In electron scattering experiments with CLAS, the trigger is given by the detection of an electron in the final state. The Čerenkov counter is one of the detectors that might be used in the event trigger. The CC discriminator thresholds for our experiment are given in Section 3.3.6. The electron efficiency within the fiducial acceptance from the measured photo-electron yield exceeds 99% (see [46]). Outside of the fiducial region the efficiency drops rapidly and varies strongly. Therefore the
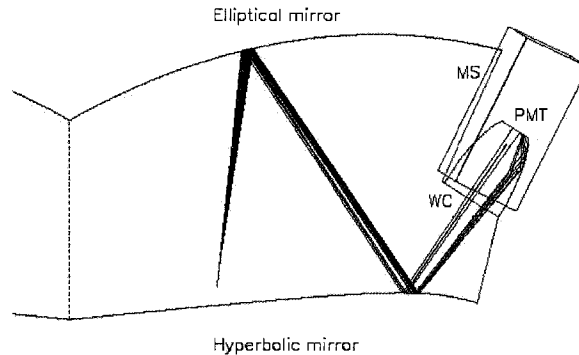
FIG. 19. One optical module of the CLAS Čerenkov Detector. Optical and light collection components are also shown. Čerenkov light from electrons reflected from the hyperbolic and and elliptical mirrors gets into the Winston Cone (WC), surrounded by a Magnetic Shield (MS) and collected by Photomultiplier Tubes (PMT).

non-fiducial region is usually excluded from the data analysis. The CC fiducial region is smaller than the EC fiducial region.

We did not use the CC for this data.

3.3.3 Time of Flight System

The Time-of-Flight (TOF) system of CLAS is designed to measure the time of flight for charged particles [47]. In conjunction with the tracking information, the TOF system allows us to determine the velocity of the particle, which determines the particle's mass

$$m = \frac{p\sqrt{1 - \beta^2}}{\beta}. \tag{21}$$

That explicitly identifies the particle. The TOF system consists of 57 scintillator strips (BC-408) in each of six sectors mounted as four panels combined together (see Figure 20). The length of the scintillator counters varies from 30 to 450 cm, with a width of 15 or 22 cm and a thickness of 5.08 cm. Scintillator strips are located perpendicularly to the beam direction with angular coverage of 2° each. The signal readout is done by PMT's connected to light guides attached to both ends of each paddle. Signals from the PMT's are read out by TDC's and ADC's. Due to cost considerations, the last 18 scintillators in the back angles are grouped into 9 pairs
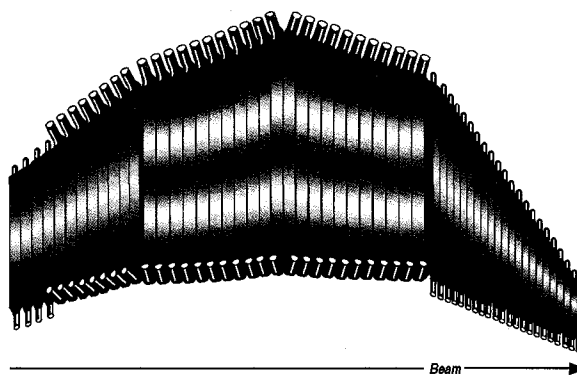
FIG. 20. The four panels of TOF scintillator counters for one of the sectors. Scintillators have different light guides and PMT's for different scattering angle coverage.

each connected to a single TDC and single ADC channel. Because of that pairing, each sector comprises 48 electronic channels. The timing resolution for scintillator counters varies with the length and width of the strip. The average time resolution is about 140 ps, which allows us to separate reliably pions and protons up to a momentum of 2.5 GeV/c.

3.3.4 Electromagnetic Shower Calorimeter

The Electromagnetic Calorimeter (EC) of CLAS is designed to identify electrons, neutrons, and photons. Mostly it is used for detection and triggering of electrons at energies above 0.5 GeV, detection of photons at energies above 0.2 GeV, and detection of neutrons, assuming their separation from photons based on time information [48].
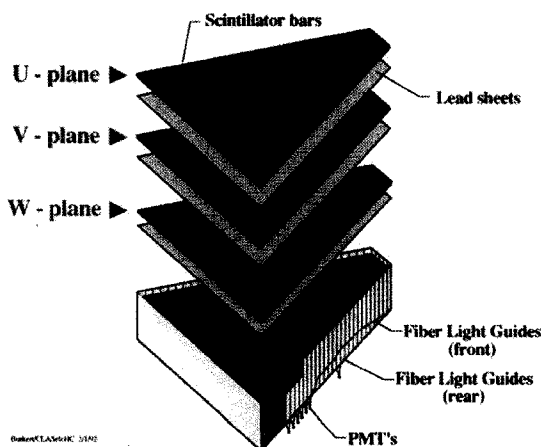
FIG. 21. View of one of the six CLAS electromagnetic calorimeter modules.

The EC system consists of alternating layers of scintillator strips and lead sheets with a total thickness of 16 radiation lengths. Electrons and photons traveling through the calorimeter produce an electromagnetic shower in the lead. The energy of the shower is converted into light by the scintillator strips, which is finally collected by PMT's [2]. A lead:scintillator thickness ratio of 0.2 was used, which requires 40 cm of scintillator material and 8 cm of lead per module. That gives approximately 1/3 of the energy of the shower to be deposited in the scintillator. In order to match the hexagonal geometry of the CLAS, the lead-scintillator sandwich is contained within a volume having a shape of an equilateral triangle (see Figure 21). There are 39 layers in the sandwich, each consisting of a 10 mm BC-412 scintillator followed by a 2.2 mm thick lead sheet. The calorimeter utilizes a "projective" geometry, in which the area of each successive layer increases. This minimizes shower leakage at the edges of the active volume and minimizes the dispersion in arrival times of signals originating in different scintillator layers. Each scintillator layer is made of 36 strips parallel to one side of the triangle, with the orientation of the strips rotated by 120° in each successive layer (see Figure 21). Thus there are three orientations or views (labeled U, V and W), each containing 13 layers, which provide stereo information on the location of energy deposition. The 13 layers of each

---

[2]Neutrons and the other hadrons make "hadronic showers".

view are combined into an inner (5 layers) and outer (8 layers) stack, to provide longitudinal sampling of the shower for improved hadron identification. Each module thus requires 36(strips)×3(views)×2(stacks) = 216 PMTs. Altogether there are 1296 PMTs and 8424 scintillator strips in the six EC modules used in CLAS.

A fiber-optic light readout system transmits the scintillator light to the PMTs. Figure 22 displays a schematic side view of the fiber-optic readout unit of the calorimeter module. These fibers were bent in a controlled way to form semi-rigid bundles originating at the ends of the scintillator strips and terminating at a plastic mixing light-guide adapter coupled to a PMT.

The total energy deposited in the calorimeter is available at the trigger level to reject minimum ionizing particles or to select a particular range of scattered electron energy. Pion events are largely suppressed by setting the EC total energy threshold E_{total} in the CLAS hardware trigger. The overall calorimeter position resolution is $\sigma = 2.3$ cm. The time resolution is about $\tau = 3$ ns.

3.3.5   Target

We used a liquid helium target at an average temperature of 3.25 K. Cooling and recirculation of ^{3}He was provided by the CLAS cryogenic system. The target cell is tapered cylinder (see Figure 23) made of kapton (7.2 mg/cm^2) about 5 cm long and with diameters 1.2 cm upstream and 0.7 cm downstream. Aluminum entrance and exit windows are 4 mm in diameter with a thickness of 15 μm (see Table II). The target cell is thermally insulated with 5 layers of aluminized mylar (0.88 mg/cm^2 per layer) combined with cerex (1 mg/cm^2 per layer). The target cell is contained within the vacuum of the scattering chamber. The scattering chamber walls were built of foam with 64 mg/cm^2 density and covered with nylon (4 mg/cm^2). The target parameters, such as temperature and pressure, were monitored during the run. We used the density versus pressure dependence given in [49] to extract the target density for our run. Target conditions were very stable; temperature and pressure fluctuated from 3.1 to 3.4 K and from 790 to 740 mBar, respectively. That gives a 1% change in the target density, which was found to be 0.067±0.0007 g/cm^3.

TABLE II. Specifications of the cryogenic helium target.

Item	Value
Length (cm)	5.00
Diameter (cm)	1.2 up 0.7 down
Temperature (K)	3.25
Pressure (mBar)	765
Density (g/cm^3)	0.067 (^{3}He)

3.3.6 Event Trigger and Data Acquisition (DAQ)

The event trigger is formed from a combination of the signals from the CLAS detector components that pass pretrigger discriminators. The configuration of the event trigger and the pretrigger discriminator thresholds are set to satisfy the requirements of each experiment. We used an inclusive (e, e') trigger. A coincidence signal that selects an electron in the final state is used to initiate readout of the event by the Data Acquisition System. The 4.7 GeV beam current was limited by the DC Region 1 occupancy. We then set the EC threshold to maximize the DAQ rate. The Level 1 trigger used in our experiment required a hit in the EC. In addition to the Level 1 trigger, we used the Level 2 trigger which requires the existence of a track in the DC in the same sector. This track requirement reduced the data acquisition rate by about 20% which allowed us to use a slightly lower EC threshold. In order to get more forward angle electrons we did not use the CC in the trigger at 4.7 GeV [3]. The pretrigger thresholds are specified in Table III. Equation 22 relates the EC thresholds with the detected electron energy [50]

$$E_{el}{}^{EC} \text{ (in MeV)} = 214 + 2.47 \times EC_{threshold} \text{ (in mV)}. \tag{22}$$

The threshold on the total deposited energy in the calorimeter, EC_{total}, was chosen to reduce the background due to low energy electrons and photons. The threshold on EC_{inner} was set to exclude minimum ionizing particles.

A schematic of the Data Acquisition System is shown in Figure 24. The signals from the CLAS detectors used to form a trigger are sent to a pretrigger logic module.

---

[3]This trigger was used for run periods 1,2 and 4 in Table IV.

TABLE III. EC Discriminator Thresholds (DT).

	4.7 GeV	
	EC_{total}	EC_{inner}
Threshold	350 mV	60 mV
Physics Equivalents	1.1 GeV	0.4 GeV

If the pretrigger conditions are satisfied, the signal is submitted to the Level-1 trigger. If there is a trigger in the event, then the signal is passed to the Trigger Supervisor (TS) which communicates with the Read Out Controllers (ROCs). The Level 2 trigger is implemented between the Trigger Supervisor and the Read Out Controller. The Level 2 trigger is passed to the ROC from the TS by a different channel. If the Level 2 trigger is satisfied, then the data are read out, digitized and transferred to the Event Builder (EB). Finally the Event Recorder (ER) receives the information from the Event Builder through the Data Distribution (DD) shared memory. The data are written to the disk and later transferred to the tape SILO for permanent storage. During the experiment, the typical DAQ rates were about 2.-2.7 kHz with a live time of about 90%. We had a luminosity of $2.-2.5 \cdot 10^{34}$ nucleons cm^{-2} s^{-1} for the 4.7 GeV runs on ^{3}He. During the run, the beam conditions, live time, trigger rates, the status of the detectors and data quality plots were continuously monitored by shift personnel.
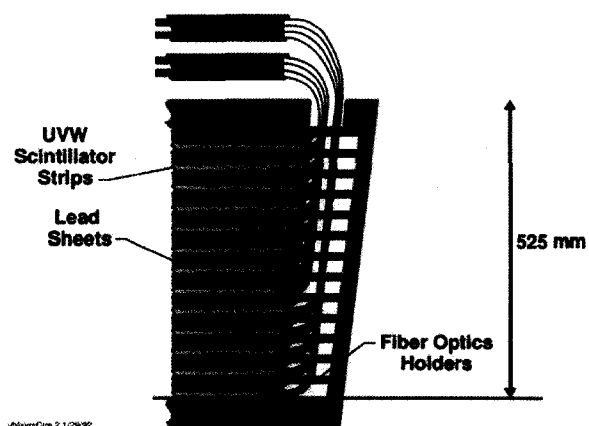
FIG. 22. Schematic side view of the fiber-optic readout unit of the calorimeter module.
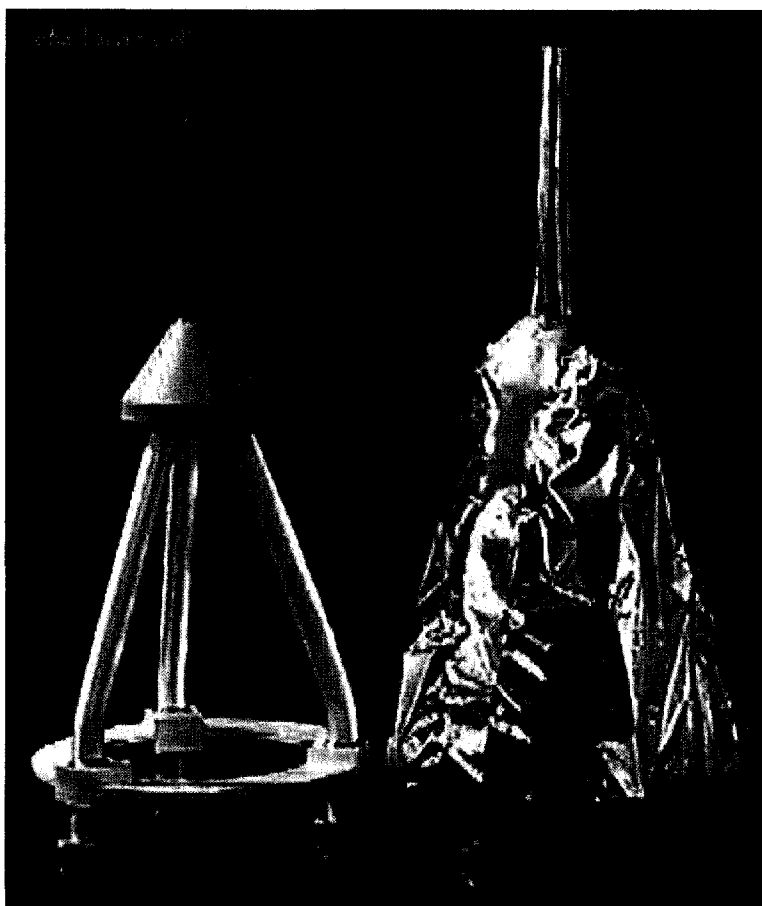
FIG. 23. Cryogenic target cell and recirculation system. The right picture shows the target cell ofter being covered with insulation.
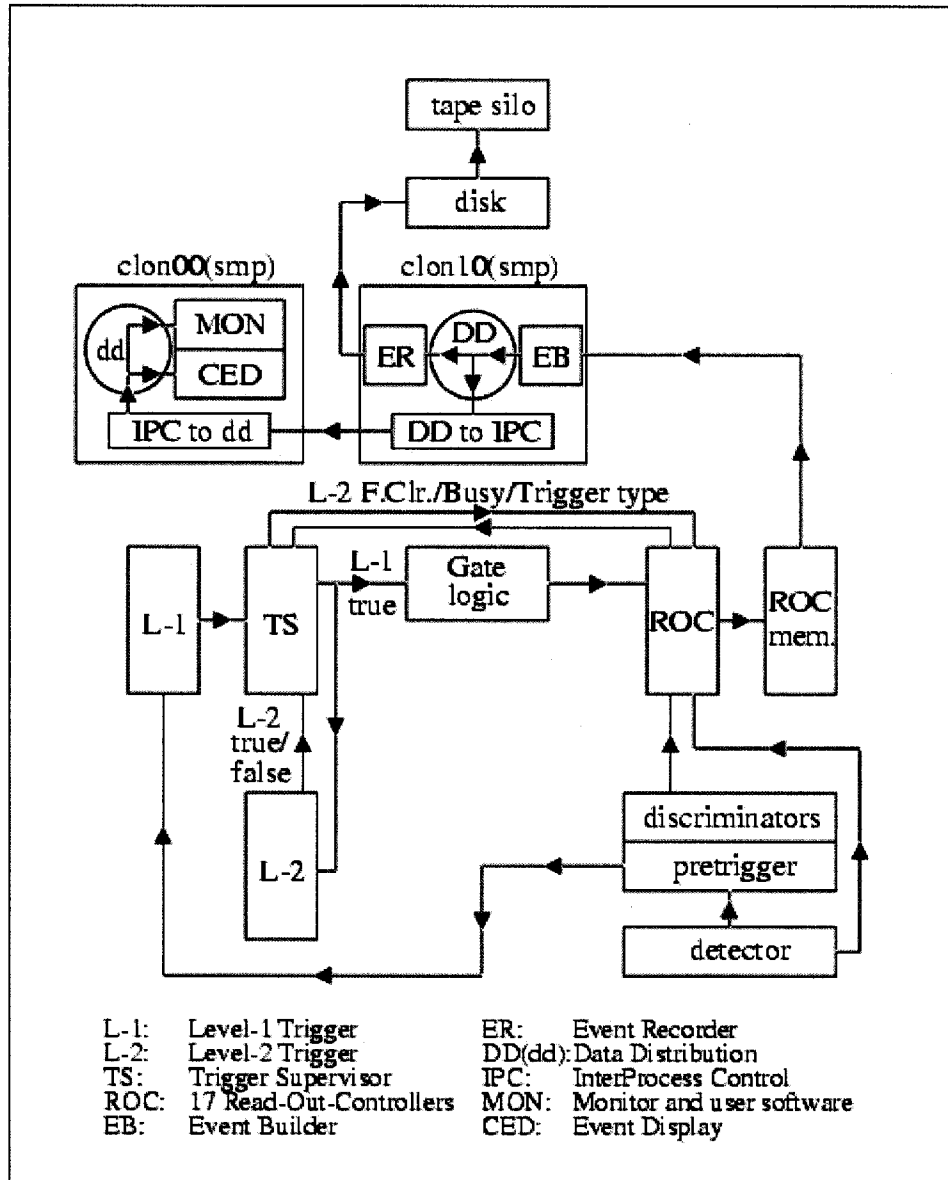
FIG. 24. Data Acquisition system of CLAS.

CHAPTER 4

DATA ANALYSIS

Experiment E2b was performed May 2 through Jun 23 of 2002. The data were collected on two targets (^{3}He and ^{56}Fe) at different energies of the incident electron beam (0.98, 4.462 and 4.71 GeV). Table IV shows the four parts of the run period. The average current used for the experiment was 8 nA, providing a luminosity on the order of 10^{34} cm^{-2}s^{-1}. For this analysis we used the ^{3}He data collected at 4.71 GeV beam energy. The trigger was defined by a hit in electromagnetic calorimeter with total deposited energy of at least 1 GeV. The Level 2 trigger was also used. The data rate was about 2.7 kHz and the dead time less than 13%. The beam energy was measured in Hall-A using their (ep) and ARC measurements.

Several corrections and calibrations were done to obtain data for the final physics analysis. The problems which will be addressed in this chapter are as follows.

- Data Processing

- Calibration

    - Drift Chamber (DC) Calibration

    - Electromagnetic Calorimeter (EC) Calibration

    - Time of Flight (TOF) Calibration

- Corrections and Cuts

    - EC Cuts

TABLE IV. Collected Runs Table.

Run Period	Runs	Energy	Torus(A)	Events	Target
1	32828–33023	4.462	2250	386.3 M	^{56}Fe
2	33083–33324	4.712	2250	820.9 M	^{3}He
3	33416–33705	0.982	1500	1287 M	^{3}He
4	33714–34000	4.712	2250	1824.6 M	^{3}He

- Angle and Momentum Corrections

- Energy Loss Corrections

- Interaction Vertex Corrections

- Vertex Cuts

- Electron Fiducial Cuts

- Proton Fiducial Cuts

The calibration of the EC and DC were done by experts and will be summarized here. TOF calibrations done by me will be described more thoroughly. Detectors were re-calibrated frequently to account for changing conditions. The DC electron drift velocity varies with changes in atmospheric pressure, temperature, humidity and gas mixture. All this can affect the drift time to drift distance reconstruction. TOF calibrations changed due to changes in the electronics or wiring.

4.1 DATA PROCESSING AND CALIBRATION

The collected data were "cooked" using the RECSIS offline reconstruction program. The "Cooking" procedure converts the raw detector information into momenta, vertices, times and particle information. RECSIS consists of modules designed to reconstruct hits from the raw detector data. Then the output from all detectors are passed to the Simple Event Builder module (SEB) which outputs the reconstructed events. The main goal of SEB is to:

- geometrically match each drift chamber track to the corresponding hits in the other detectors

- identify the event trigger particle (i.e., the electron)

- calculate the trigger time

- identify the particle types corresponding to the various tracks

- build an event and write it to output

The geometrical matching defines distances between the detectors' hit positions (r_i) and the position on the detector plane (r_{pl}) defined by the Master track. For charged particles, the DC track is taken as the Master track. For neutral particles, EC hits are used to generate Master tracks (straight lines starting at the origin). In each detector, the hit closest to the Master track is selected and associated with that track. Then for each hit the squared sum of difference between coordinates is divided by the uncertainty of that coordinate:

$$C_i^2 = \sum_{i=x}^{z} \frac{(r_{\mathrm{pl}} - r_i)^2}{\sigma_{r_i}^2} \tag{23}$$

where i runs for x, y and z coordinates for given detector coordinates, and σ_{r_i} is the error for given coordinate. The hit with minimum C_i is taken as a match. First the matching is done for all the tracks reconstructed in the given event, then the remaining hits are considered as candidates for neutral particles. Straight tracks are constructed for hits in the EC that were not associated with any of the DC tracks.

The second stage identifies the trigger particle, which is required to have a negative track and a showering hit (i.e., greater than minimum ionizing) in the EC. The largest momentum candidate is chosen. As we will see later, in this way we still have some pion contamination left. Another problem occurs because we require the trigger particle to be the largest momentum particle. We will later estimate the number of the electrons which have been misidentified because of these criteria.

The third step determines the time the trigger particle left the target. The trigger time on target is:

$$t_{\mathrm{trk}} = t_{\mathrm{det}} - \frac{R_{\mathrm{det}}}{\beta c} \tag{24}$$

where t_{det} is the time measured by the TOF detector, R_{det} is the path length of the particle's track (determined in the track reconstruction module), and $\beta = 1$ for electrons. If the trigger particle is found, then SEB constructs a logical structure for storing the particle information. An example of SEB hit matching is shown in Figure 25.

After selecting the trigger particle and calculating the trigger time, RECSIS calculates the velocity, β, for each particle candidate based on the detector measured time t_{det}, and the path length:
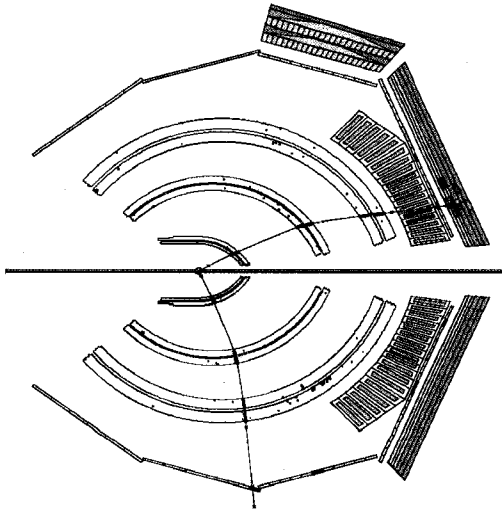
FIG. 25. Sample event reconstructed by RECSIS. The in-bending track on the top half of the detector corresponds to the electron that triggered the event, the out-bending track on the lower half corresponds to a positively charged particle.

$$\beta = \frac{R_{trk}}{\left(t_{det} - t_{trk}\right) \cdot c} \tag{25}$$

Charged particles are identified using β and the measured momentum. The β for neutral particles is calculated from the time measured by the EC. If β is within 5% of 1, then particle is identified as a photon, otherwise it is identified as a neutron.

4.1.1 Drift Chamber Calibration

The CLAS drift chambers consist of six identical sectors each of which is divided into three regions. Each region is a separate physical volume consisting of two superlayers (axial and stereo). The schematic view of the Drift Chambers is shown on Figure 26. Each superlayer contains six layers of sense wires (except superlayer 1, which has only four layers). Each superlayer is separately calibrated, yielding 36 sets of calibration constants.

The primary purpose of the Drift Chamber calibration is to refine the drift time to drift distance conversion to optimize position measurement. The constants for the drift time-to-drift distance conversion have to be systematically calibrated and

checked for stability over the run period. Commonly, one run is chosen from each day of the run period and approximately 100K events from this run are calibrated.

The calibration procedure consists of several iterations of running the reconstruction program followed by refitting the calibration constants.

The track reconstruction in the Drift Chambers is done in two stages. In the first stage, individual tracks are fit to hit-wire positions ("hit based tracking"). In this stage, the hits inside the superlayer are combined into track segments, which are then linked together to form tracks across all three regions. At this stage, due to the comparatively small size of the drift cells and the large number of wire layers, the track momenta can be reconstructed with $3 - 5\%$ resolution [44]. In the second stage, the time-of-flight information obtained from scintillator counters is used to determine the drift times for each wire hit. The drift time is given by:

$$t_{\text{drift}} = t_{\text{TDC}} + t_0 - t_{\text{start}} - t_{\text{flight}} - t_{\text{prop}} - t_{\text{walk}} \qquad (26)$$

where t_{start} is the event start time (determined by TOF), t_0 is the fixed-time delay for the wire, t_{TDC} is the time measured by the TDC, t_{flight} is the particle flight time from the reaction vertex to the wire, t_{prop} is the signal propagation time along the wire, and t_{walk} is a time-walk correction made for short times due to different ionization for slow and fast particles. Then these drift times are converted to drift distances using the constants we are calibrating. These drift distances give the Distance of Closest Approach (DIST) to each wire. This second stage is called time-based-tracking (TBT). The final track is then fit to minimize the residual distance from the track to each of the DISTs.

When a charged particle goes through the drift chambers, at least one cell in each of the 34 layers should be hit[1]. Each hit detected in the chamber is used to determine the particle's track via least a squares fit done in the CLAS reconstruction program. The quantities used to describe the distance of the charged particle track from a sense wire are:

- *DOCA* (Distance Of Closest Approach) is the distance from the fitted track to the sense wire determined by time-based tracking. This quantity is obtained from the fits to a global track that includes all layers

---

[1]In fact, on average there are 30 hits per time based track, due to inefficiencies and holes in the drift chambers
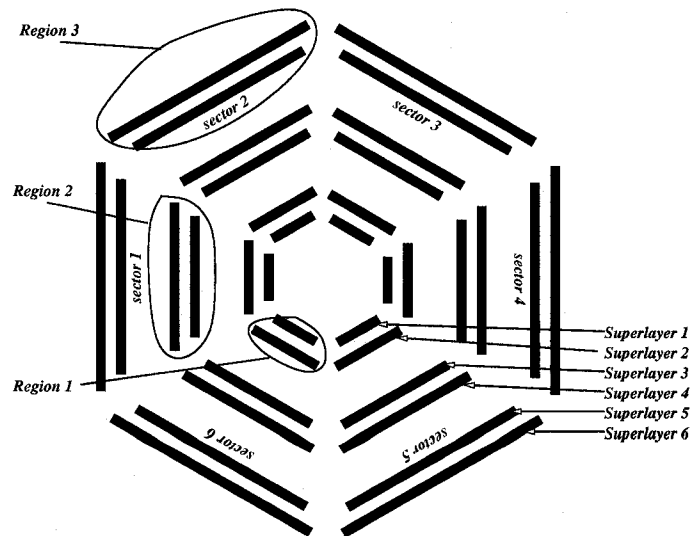
FIG. 26. Schematic View of the CLAS Drift Chambers. This view represents a vertical slice through the drift chambers at the target position. The schematic shows how the regions and superlayers are placed and named.

- $DIST$ is the measured distance from the sense wire to the track, which is calculated from the drift time and other parameters. The drift time is determined from the TDC values for the wire, corrected for fixed cable delays and track dependent delays such as flight time.

The difference between these quantities is called the "time residual", defined as:

$$Res = |DOCA| - |DIST| \tag{27}$$

The sign of the residual is determined by the sign of any systematic shift. The residuals are the primary means of measuring the resolution of the drift chambers. The standard deviations of the residual distributions are estimated by means of a Gaussian fit. Note that $DIST$ is defined as positive definite, while $DOCA$ is assigned a sign determined by whether the track passes to the right or to the left of the wire. A more detailed description of the drift chamber calibration procedure is given in [51].

4.1.2 Function Parametrization

The goal of the Drift Chamber calibration is to optimize the parameters of the drift velocity function for each superlayer in each sector. The drift velocity function is the relation between the distance of closest approach (DIST) of a particle track and the drift time, the time it takes the electrons knocked out by the particle to drift to the sense wire. The time to distance correlation function is determined by the drift chamber geometry and operating conditions and the gas mixture. The fact that the cells of the DC are not circular, but are hexagonal, leads to angle dependent corrections.

The track angle is the angle of the track relative to the side of the hexagon $0° - 30°$. The drift time to drift distance function at a given track angle is given by:

$$x(t) = v_0 t + \eta \Big(\frac{t}{t_{\max}}\Big)^p + \kappa \Big(\frac{t}{t_{\max}}\Big)^q \qquad (28)$$

where v_0 is the saturated drift velocity near $t = 0$, and the parameters η, κ, p and q are determined by minimizing the residual. For tracks near the outer edge of the
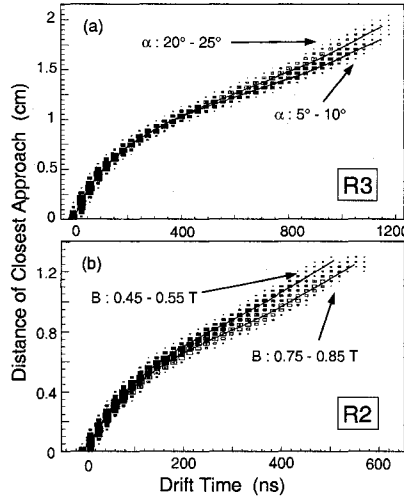
FIG. 27. Scatter plot of DOCA versus the corrected drift time for a) R3 axial wires showing the track angle dependence, and b) R2 axial wires showing the magnetic-field dependence where the local angle ranges between $23°$ and $25°$. The overlaid curves represent the fitted time-to-distance function

cell, the first arriving ions follow the electric-field line from the field wire to the sense wire, independent of entrance angle [51]. The corresponding maximum drift time is

referred to as t_{max}. A normalized drift time $\hat{t} = t/t_{max}$ is used as an argument to the time-to-distance function that satisfies the cell boundary constraint:

$$x(\hat{t} = 1, \alpha) = C \cdot \cos(30° - \alpha) \tag{29}$$

where α is the track angle and C represents the cell size. The time-to-distance function is deduced using a correction function:

$$x(\hat{t}, \alpha) = x_0(\hat{t}, \alpha_0) + C(\cos(30° - \alpha) - \cos(30° - \alpha_0))f(\hat{t}) \tag{30}$$

where x_0 represents the drift distance expected for a given normalized drift time assuming an entrance angle α_0. The track angle is taken the average entrance angle for the full fitted data set. The function $f(\hat{t})$ is used to correct the extracted drift distance for the true track angle.

Since the Region 2 drift chambers are located between the torus cryostat, the inhomogeneous magnetic field affects the drift velocity. These effects are modeled by a modification of the effective entrance angle of the track and by an increase of t_{max}. This issues are studied and described in [51]. The example of fitted time-to-distance distributions are shown Figure 27. Figure 27 (a) shows this distribution for Region 3 and 27 (b) for Region 2, which are located in the magnetic field. Figure 28 shows the residuals for superlayer 1–red, 2–green, 3–blue, 4–yellow, 5–magenta, 6–light blue obtained after the calibration vs run number.

4.1.3 Electromagnetic Calorimeter Time Calibration

The Electromagnetic Calorimeter (EC) is an important part of the CLAS detector. It serves three main functions [48]:

- Detection and triggering of electrons with momentum above 0.5 GeV. The total energy deposited in the EC allows minimum ionizing particle rejection at trigger level.

- Detection of photons at energies above 0.2 GeV, allowing π^0 and η reconstruction from the detection of their 2γ decay (not used in this analysis).

- Detection of neutrons, with discrimination between photons and neutrons using time-of-flight measurements (not used in this analysis).
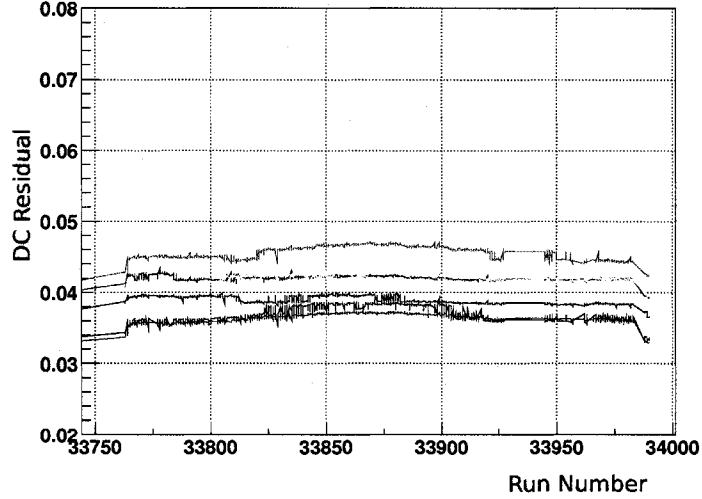
FIG. 28. Residuals after the calibration for different superlayers vs Run Number. Superlayer 1–red, 2–green, 3–blue, 4–yellow, 5–magenta, 6–light blue.

The EC timing is calibrated by comparing to the time measured by the TOF and extrapolated to the EC for electrons. Since there is no magnetic field between the scintillator counters and the electromagnetic calorimeter, the track of the particle is straight. The time measured by the EC should be:

$$T_{EC} = T_{TOF} + \frac{d_{trk} \cos \alpha}{c} \tag{31}$$

where T_{TOF} is the time measured by the TOF, d_{trk} is the distance between TOF and EC strips, and α is the particle impact angle on the EC plane. The time measured by the EC (T_{EC}) is assigned to the strip with the largest signal for each of the three views. Then the measured time is corrected for pulse height and length effects:

$$T_{EC} = P_0 + P_1 \cdot A_{TDC} + \frac{P_2}{\sqrt{A_{ADC}}} + P_3 \cdot L^2 + P_4 \cdot L^3 - \frac{L}{v_{eff}} \tag{32}$$

where L is the distance from the hit point to the EC readout edge, v_{eff} is the speed of light in the scintillator material, and A_{ADC} and A_{TDC} are the ADC and TDC values respectively. The first two terms are the simple linear response of the TDCs, the third term is the time-walk correction, the fourth and fifth terms are small corrections for the fact that signals arrive at the readout edge at slightly different times for different scintillator bars connected to the same PMT, and the last term compensates for the
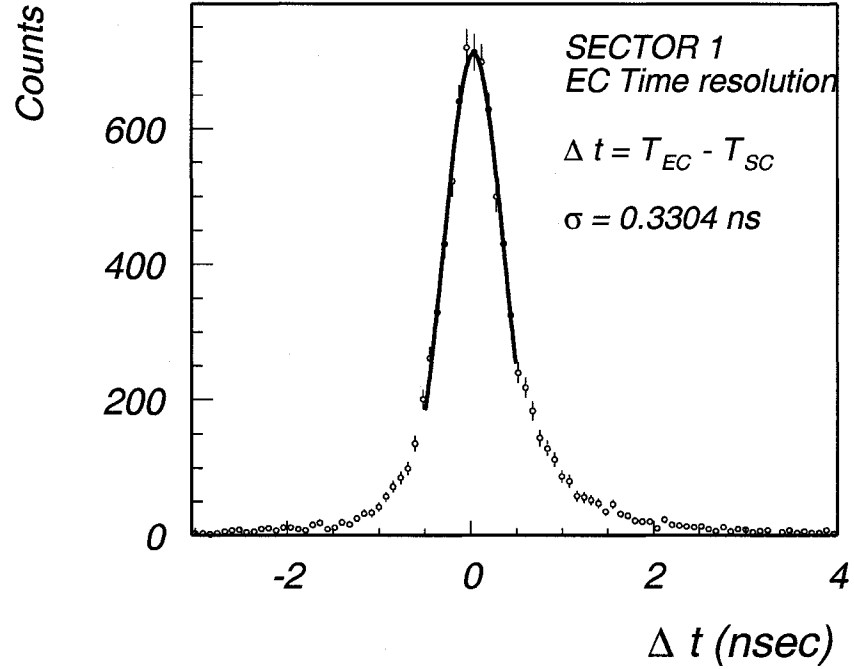
FIG. 29. The time resolution of the CLAS Electromagnetic Calorimeter. The calibrated TOF time difference defined in Eq. (33) is plotted for one sector.

time required for scintillator light to travel from the hit position to the readout edge. The fit parameters are saved in the calibration database. The time difference between the Time-of-Flight and EC time values can be seen in Figure 29. The quantity Δt (for electrons) is plotted for one sector, defined as:

$$\Delta t = T_{\mathrm{EC}} - T_{\mathrm{TOF}} - T_{\mathrm{trk}} \tag{33}$$

where T_{EC} is the time measured by the Electromagnetic Calorimeter, T_{TOF} is the time measured by the TOF counters, and T_{trk} is the time that take a particle with $\beta = 1$ to travel distance between the TOF counters and the plane of the EC. As can be seen from the picture, the overall EC time resolution is $\sigma \sim 330$ ps, which is partially due to the TOF resolution. Taking the TOF resolution equal to 150 ps, one can calculate the EC time resolution for electron to be $\sqrt{330^2 - 150^2} = 294$ ps. For neutral particles the resolution is not as good as for electrons.

4.1.4 TOF Calibration

The TOF is one of the essential components of CLAS detector. It is used to identify charged particles. The quality of particle identification primarily depends on the Time-Of-Flight measurements, therefore a big effort is devoted to TOF calibration. TOF calibration consists of: calibration of individual TDC and ADC channels, left-right PMT alignment, attenuation length calibration, and counter to counter calibration.

4.1.5 Pedestal and TDC calibration

The pedestals of the Analog-to-Digital Converter (ADC) were measured by taking runs with random triggers. This data is analyzed and saved in the calibration database. The Time-to-Digital Converters (TDC) were calibrated using runs taken with a special DAQ configuration. Every counter in the TOF system was pulsed with a laser and the responses of each TDC for various delays between the "START" and "STOP" signals were analyzed. The actual time was parametrized in terms of the measured TDC time as:
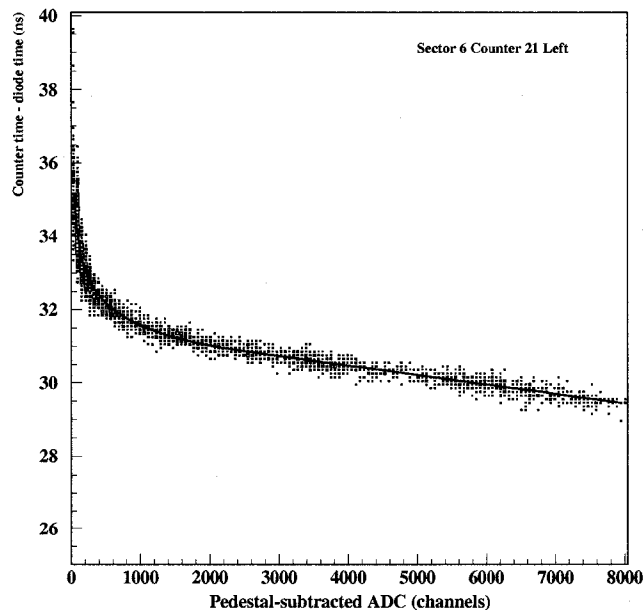
FIG. 30. Typical distribution of TDC time (channels) versus pulse height (ADC channels). The fitted function f_w is used in the time-walk corrections.

$$t = c_0 + c_1 T + c_2 T^2 \tag{34}$$

The constants c_1 and c_2 are saved in the calibration database. The parameter c_0 is not relevant, since left-right calibration is done later to equalize the left-right difference for each counter.

4.1.6 Time Walk Correction

The time-walk corrections were done using data obtained with the laser pulse run. The amount of light delivered to each counter was varied, and the pulse height and time were measured for pulses with different amplitudes to obtain the pulse height to time dependence. The time-walk correction is done in software:

$$t_w = t - f_w \frac{(A - P)}{V_T} + f_w \frac{600}{V_T} \tag{35}$$

where V_T is the TDC channel corresponding to the leading-edge discriminator threshold of 20 mV (~ 35 channels), A is the ADC channel, P is the pedestal for a given ADC, and f_w is the time walk correction shown on Figure 30. The parametrization of f_w contains three parameters (a, b and c). These parameters are determined for each PMT separately using laser calibration runs. The rapidly changing function (see Figure 30) is fitted with:

$$f_w(x) = \frac{b}{x^c}, \quad \text{for } x < a \tag{36}$$

$$f_w(x) = \frac{b}{a^c}(1 + c) - \frac{bc}{a^{c+1}}x, \quad \text{for } x > a \tag{37}$$

The fit parameters a, b and c are saved in the calibration database for offline software corrections.

4.1.7 Left-Right PMT Alignment

The measured position of the hit along the TOF counter is determined by the relative arrival time of the signals at the left and right PMTs. Therefore the relative left-right timing must be determined to provide accurate measurement of the position. For each counter the quantity:

$$l = t_L - t_R \tag{38}$$

should be centered around zero. If it is not, then an offset, Δt is added to this value, where:

$$\Delta t = \frac{l}{v_{\text{eff}}} \tag{39}$$

where v_{eff} is the effective velocity of the light in the TOF counter. The effective velocity is calculated using the hit position information provided by tracking:

$$y = v_{\text{eff}}\frac{(t_L - t_R - t_{\text{off}})}{2} \tag{40}$$

The dependence of the distribution $t_L - t_R$ versus y for each counter is fitted with a linear function to determine the constants t_{off} and v_{eff}. The offsets (Δt) are saved in the calibration database for offline time corrections.

4.1.8 Energy Calibration
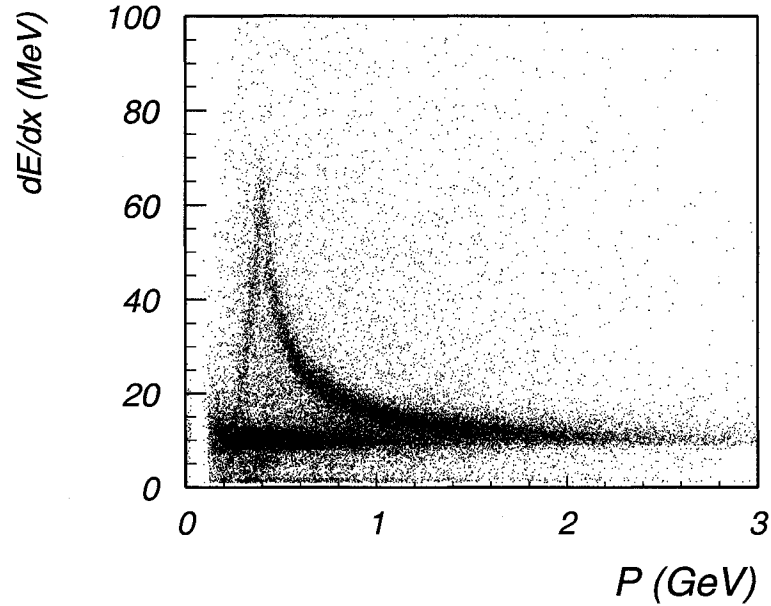
FIG. 31. Energy deposited in the TOF scintillators by hadrons versus hadron momentum after MIP calibration is done. The pion and proton bands are clearly distinguishable.

The time-of-flight system also serves for proton-pion separation without using timing information. The separation of protons from pions is done using the measured deposited energy in the scintillators. The dependence of the deposited energy

$(\delta E/\delta x)$ on momentum is different for protons and pions. The ADC pulse heights are normalized using energy deposited in the scintillators by minimum ionizing particles:

$$A_L = \frac{N_L}{k} \exp\left(-\frac{L/2 - y}{\lambda}\right) \tag{41}$$

$$A_R = \frac{N_R}{k} \exp\left(-\frac{L/2 + y}{\lambda}\right) \tag{42}$$

where A_L and A_R are the ADC channels (pedestal subtracted), N_L and N_R are the peak heights of the Left and Right PMTs respectively when the minimum ionizing particle passes through the center of the scintillator, L is the scintillator counter length, y is the distance of the hit measured from the center of the counter, and λ is the attenuation length. Then the energy, E_d, is found by calculating the geometrical mean from the Left and Right ADC channels:

$$\bar{A}_g = \sqrt{A_L A_R} = \alpha E_d \exp\left(-\frac{L}{2\lambda}\right) \tag{43}$$

where $\alpha = (N_L N_R)^{-1/2}/k$, and E_d is the position invariant measure of the deposited energy.

The energy calibration is done using minimum ionizing pions. The scintillator timing information is used to select the pions, therefore the method requires reasonable timing calibration. Figure 31 shows the deposited energy $(\delta E/\delta x)$ of hadrons versus hadron momentum after energy calibration. At low energies protons and pions can be well separated, and at higher momentum, starting from 0.8 GeV, the two bands start to merge. This method of pion identification was not used for data analysis, it only provided a reasonably clean sample of pions for further calibration.

4.1.9   RF and paddle-to-paddle corrections

Once all individual scintillator ADCs and TDCs have been calibrated, it is important to determine their relative timing offsets (paddle-to-paddle calibrations). The time of the hit in the counter is calculated as:

$$T_{\text{TOF}} = \frac{t_L + t_R}{2} - \frac{V_R - V_L}{2V_R V_L} y \tag{44}$$

where t_L and t_R is the time measured by the Left and Right PMTs respectively, y is the hit position, and V_L (V_R) is the speed of the light propagation towards the left
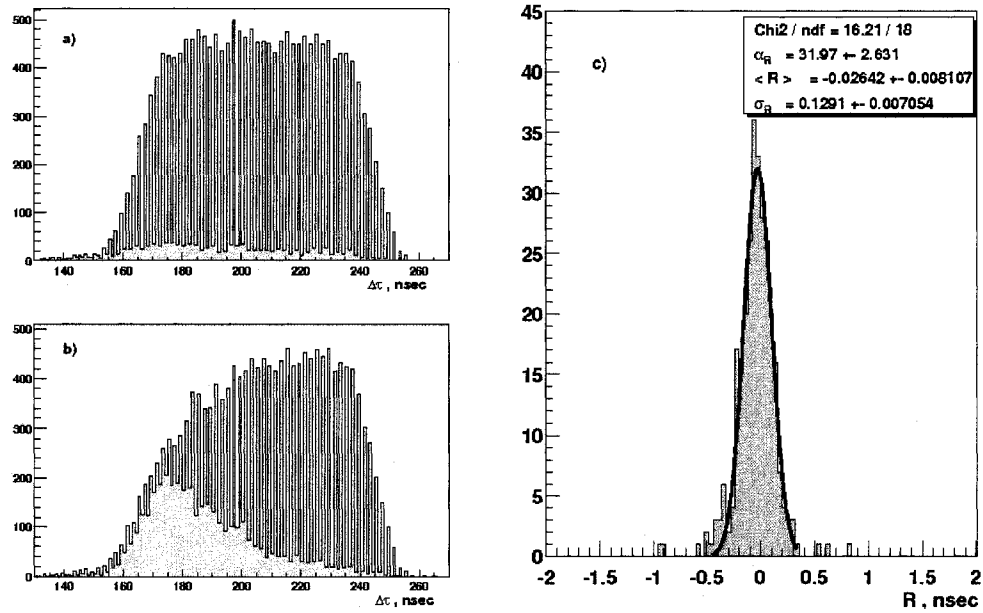
FIG. 32. Illustration of the beam RF-structure: a) $\Delta\tau$ distribution with properly calibrated TDCs, b) $\Delta\tau$ distribution when the c_1 parameter of the TDC of the RF-signal is miscalculated by less than 1%, c) R-distribution (described in Eq. (47)) for a single scintillator channel, fit to a Gaussian.

(right) PMT. First, all scintillator counter timing is aligned to the one of the RF-signal. The difference between the event start time and the RF time is calculated as:

$$\Delta\tau = T_{\text{TOF}} - T_{\text{flight}} - T_{\text{RF}} \tag{45}$$

where T_{flight} is the time of flight of the particle, calculated from the information provided by tracking (using the path length the particle has traveled and assuming $\beta = 1$), and T_{RF} is the time of the RF-signal.

The RF-signal is provided by the accelerator to all Halls. This signal is generated with each electron bunch (the length of each bunch is ~ 2 ps, and the distance between bunches is ~ 2 ns) with frequency $\nu = 1.4971$ GHz in the injector. The RF-signal is sent to all three experimental halls with a prescale factor of 40. The bunches delivered to each hall are separated by time intervals of:

$$\Delta T = \frac{3}{\nu} = \frac{3}{1.4971 \text{ GHz}} = 2.0039 \text{ ns} \tag{46}$$

where ν is the accelerator frequency, and the factor 3 appears because the beam

from the injector is shared among the three experimental halls. Figure 32 a) shows $\Delta\tau$ plotted for a single TOF channel. The multiple peaks on the plot arise from the prescale factor of 40. The TDCs of the RF-signal usually have a slope and need to be calibrated before calibrating the scintillation counters. The procedure of RF-signal calibration is described in [47]. Figure 33 a) shows the time delay (R) versus T_{RF} when the RF-signal TDC is not calibrated, and b) shows the same dependence after calibration. If the TOF and RF-signal TDCs are well calibrated, then the peaks on Figure 32 a) should be separated by exactly ΔT (2.0039 ns). This plot is also sensitive to the TDC calibrations. If the TOF TDCs and RF were not well calibrated, it may cause a pattern similar to the one shown in Figure 32 b).

For each scintillator counter, the time offset is calculated as:

$$R = \mathrm{mod}((T_{\mathrm{TOF}} - T_{\mathrm{flight}} - T_{\mathrm{RF}} + 100 \cdot \Delta T), \Delta T) - \frac{\Delta T}{2} \qquad (47)$$

where $\mathrm{mod}(a, b)$ is the modulus of a with respect to b and ΔT is the bunch spacing. This quantity defines the time delay for the each scintillator counter with respect to the RF-signal. Figure 32 c) shows the time delay (R) for one TOF counter. This value must be subtracted from the measured TOF time event by event. The resolution depends on the timing characteristics of the scintillator, the quality of the calibration of TOF TDCs, and the calibration of the RF-signal. Once the RF-signal has been calibrated, the R (given by Eq 47) for each counter is fitted to find the mean value (the shift from zero). These constants, called "fine tuning constants", are saved in the database, and the time measured by particular scintillation counter will be software corrected with the corresponding time delay constant. Since electrons are mainly produced in the forward direction, pions are used to calibrate backward counters. In the case of pions, the time of flight is calculated using tracking information.

4.1.10 Alignment of TOF system to the RF-signal

To determine the mass of hadrons using flight time information, one has to know the start time of the event. The natural choice would be using the electron time to determine the start time of the event at the collision vertex. The time of flight of the hadron and its resolution is given by:

$$T_{\mathrm{start}} = T_{\mathrm{TOF}}^{e} - \frac{L_{\mathrm{track}}^{e}}{c} \qquad (48)$$

$$T^h_{\text{flight}} = T^h_{\text{TOF}} - T_{\text{start}} \tag{49}$$

$$\delta T^h_{\text{flight}} = \sqrt{(\delta T^h_{\text{TOF}})^2 + (\delta T^e_{\text{TOF}})^2 + \left(\frac{\delta L^e_{\text{track}}}{c}\right)^2} \tag{50}$$

where T^h_{TOF} is the time measured by scintillator counter for hadron, L^e_{track} is the length of the electron track from target to scintillator counter and c is the speed of light. The electron timing resolution δT_{TOF} contributes significantly to the uncertainty of the hadron time of flight. To eliminate the contribution from the electron timing resolution, the RF-signal is used to determine the event start time. After the paddle-to-paddle calibration is complete, the timing offsets of all scintillator counters are adjusted with respect to the same RF bunch. Therefore, the time measured by scintillators for hadrons can be corrected with the RF-signal:

$$T_{\text{flight}} = T^h_{\text{TOF}} - \left(T^e_{\text{TOF}} - \frac{L^e_{\text{track}}}{\beta c} - R^e\right) \tag{51}$$

$$\delta T_{\text{flight}} = \sqrt{(\delta T^h_{\text{TOF}})^2 + \left(\frac{\delta L^e_{\text{track}}}{\beta c}\right)^2} \tag{52}$$

Before using Equation 51, all time-of-flight counters must be adjusted with respect to the RF-signal. But because the tuning of the beam can change the path length of electrons from the injector where the RF signal is generated to the target in the experimental hall, and because the signal propagation speed in the cables may vary with time, this adjustment must be done for every run.

4.1.11 Calibration Results

The procedures described above were done to allow the CLAS off-line analysis software to reliably distinguish among different types of hadrons. The timing resolution determined by the Time-of-Flight calibration is very important to identify hadrons and reduce non-physical background. The quality of Particle Identification (PID) can be seen in Figure 34. Figure 34 (a) shows the dependence of β versus particle momentum (all scintillator counters combined). One can see distinguishable bands for different particles, and protons can be clearly separated from protons up to 2.5 GeV/c. A particle's mass can be calculated knowing its velocity, measured by the TOF, and momentum, measured by tracking. Figure 34 (b) shows a mass spectrum for an empty target run (ie: scattering from the target cell walls) at an electron beam
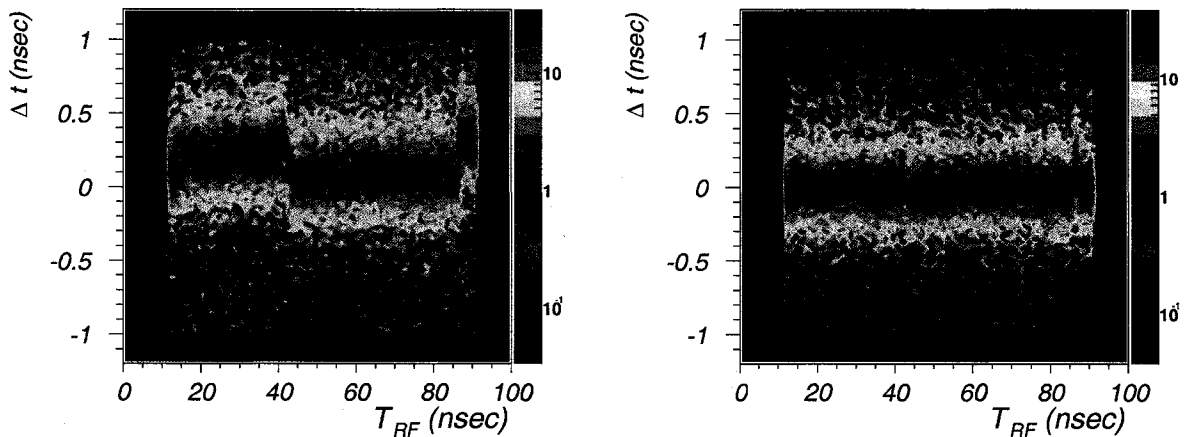
FIG. 33. Two dimensional plot of R versus t_{rf} distribution for a) uncalibrated RF-signal and b) calibrated RF-signal.

energy of 4.4 GeV. Separate mass peaks corresponding to pions, kaons, protons and deuterons can be seen.

It is also important that the calibrated results be stable during the entire period. Figure 35 shows the run number dependence of the RF offset (in red), σ_{RF} for electrons (in green), σ_H for hadrons, and $\sigma_{EC-time}$ the EC time resolution. The constant behavior during the 4th run period (runs 33714–34000) indicates the stability of the data through this run period.

4.2 CORRECTIONS AND CUTS

4.2.1 Trigger Particle Identification Cuts

As was mentioned in Chapter 3, RECSIS occasionally misidentifies the identification of the trigger particle. Especially at low momenta, the separation of negative pions and electrons is very complicated. We will use information from the EC to improve this separation. Figure 36(a) shows the ratio of the total energy deposited in the EC by the trigger particle (identified by RECSIS) divided by the momentum of that particle versus the momentum of that particle. Minimum ionizing pions passing through the scintillator should deposit around 2 MeV per centimeter. Therefore the
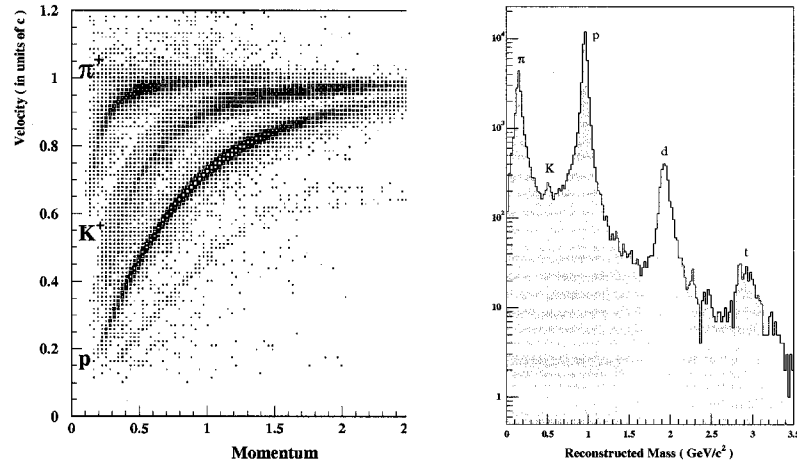
FIG. 34. Particle ID from TOF. a) the velocity of positively charged particles versus momentum. The kaon band is artificially enhanced by preselecting events from a data sample with a loose kaon cut. b) hadron masses calculated from momentum p and TOF for an empty target run at $E_0 = 4.4$ GeV. Clearly visible peaks correspond to pions, kaons, protons, deuterons and tritons respectively.
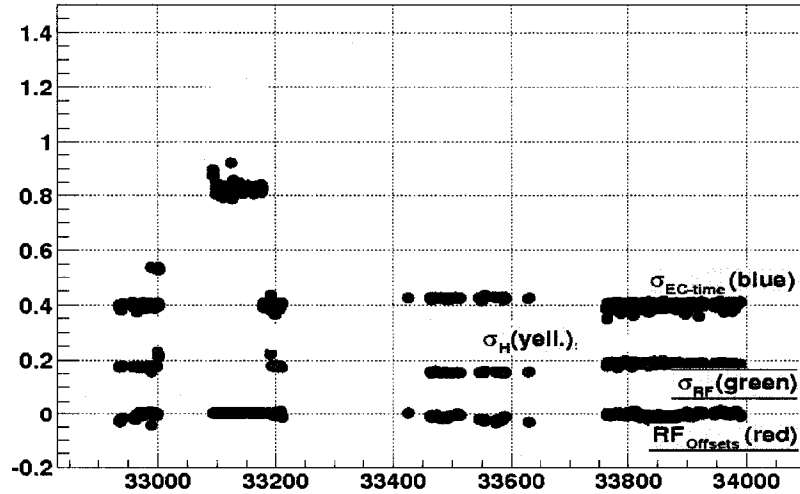
FIG. 35. Calibration time variation: RF offset, σ_{RF} (from electrons), resolution σ_H (hadrons), sigma of EC time depending on run number.
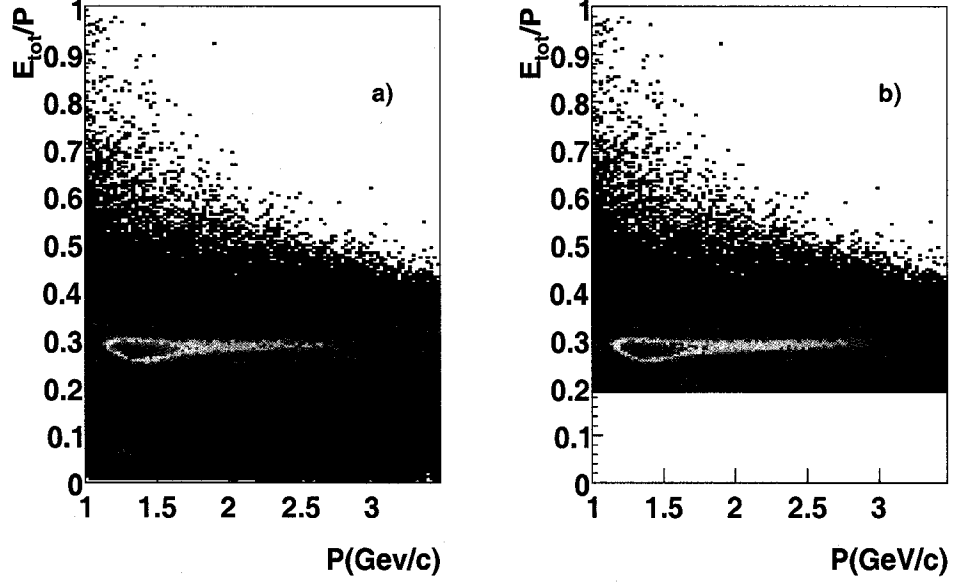
FIG. 36. Ratio of the total energy deposited in the EC by the trigger particle (identified by RECSIS) divided by the momentum of the particle versus momentum a) all events b) after cutting on $E_{\text{tot}}/p > 0.19$

total energy deposited in the detector should be independent of momentum. Electrons shower in the EC and deposit all of their energy. Therefore the energy deposited will be proportional to momentum. Figure 36(a) shows the constant distribution at E_{tot}/p for electrons at 0.3 and a band of pions (starting from 0.1) at low momenta. A similar picture can be obtained for the inner layer of the EC. Figure 37(a) shows the energy deposited in the inner layer of the EC divided by momentum. Note the contribution from minimum ionizing particles in the lower left corner. To eliminate the pion contribution, we required

$$E_{\text{tot}}/p > 0.19$$

and

$$E_{\text{in}}/p > 0.05$$

We also apply a cut on the momentum of the trigger electron $p + \text{el} > 1$ GeV/c
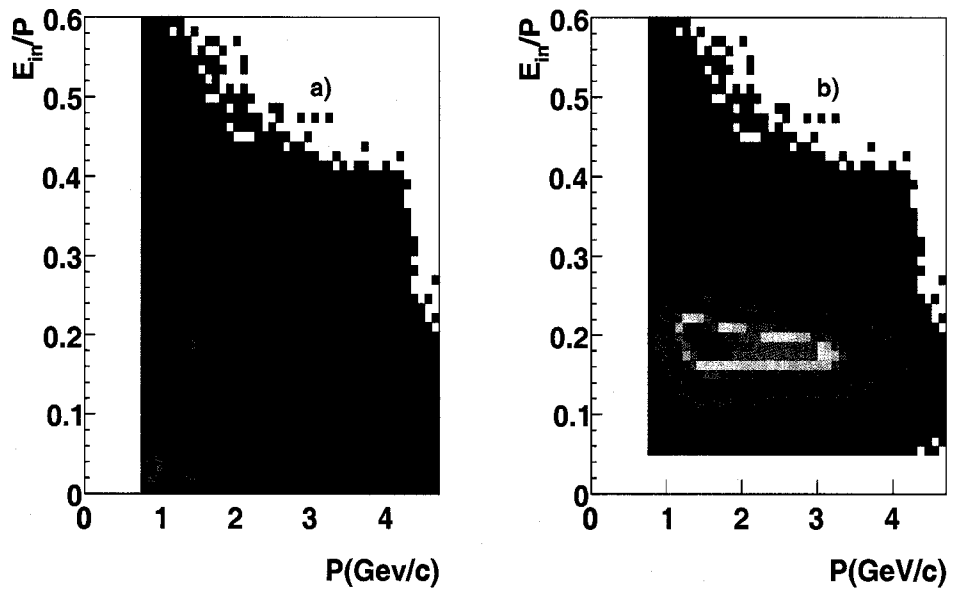
FIG. 37. Ratio of the energy deposited in the inner layer of the EC by the trigger particle (identified by RECSIS) divided by the momentum of the particle versus momentum a) all events b) after cutting on $E_{in}/p > 0.05$.

4.2.2 Momentum and Angle Corrections

There are several factors responsible for the incorrect reconstruction of momentum and angle in CLAS. In this section we will try to correct the momenta and angles for effects due to:

- Misalignment of the drift chambers relative to their nominal position

- Uncertainty of the magnetic field [52]

Since the drift chambers were installed in 1995, sectors of Region 3 have been removed almost every year for repair. Region 1 was moved once, but as a single unit. After removal, the precision of re-installation is about 3 mm. Using straight track events it is possible to measure this to about 100 μm, however, the absolute displacement of the drift chambers is greater and can not be accounted during the reconstruction. Without correction, the invariant mass ($W^2 = (m_p + \omega)^2 - \vec{q}^2$) spectrum for $^1H(e, e')$ data shows a strong dependence on the polar angle ϕ of the electron (Fig. 38) which causes fairly bad resolution (around 40 MeV). The ϕ dependence of W is a magnetic field problem since $\vec{B}$ is not parallel to $\hat{\phi}$ near the cryostat.

The ability to measure exclusive reactions hands us a powerful tool to parametrize the unknowns above and correct for the momentum and angle errors. The procedure to do that was developed and well described by Sebastian Kuhn and Alexei Klimemko [54]. The effect of displacement of the DC and possible discrepancies in the magnetic field on the measured scattering angle θ_{rec} have been parametrized in the form

$$d\theta = (c_1 + c_2\phi_{rec})\frac{\cos\theta_{rec}}{\cos\phi_{rec}} + (c_3 + c_4\phi_{rec})\sin\theta_{rec} \tag{53}$$

$$\theta_{cor} = \theta_{rec} + d\theta$$

and

$$dp = \left\{(c_5 + c_6\phi_{rec})\frac{\cos\theta_{cor}}{\cos\phi_{rec}} + (c_7 + c_8\phi_{rec})\sin\theta_{cor}\right\} \cdot \frac{p_{rec}}{qB_{torus}}c$$
$$+c_9 + c_{10}\phi_{rec} + c_{11}\phi_{rec}^2 + (c_{12} + c_{13}\phi_{rec} + c_{14}\phi_{rec}^2)\sin\theta_{cor}\ c \tag{54}$$

$$p_{cor} = p_{rec} + dp$$

(a)   (b)
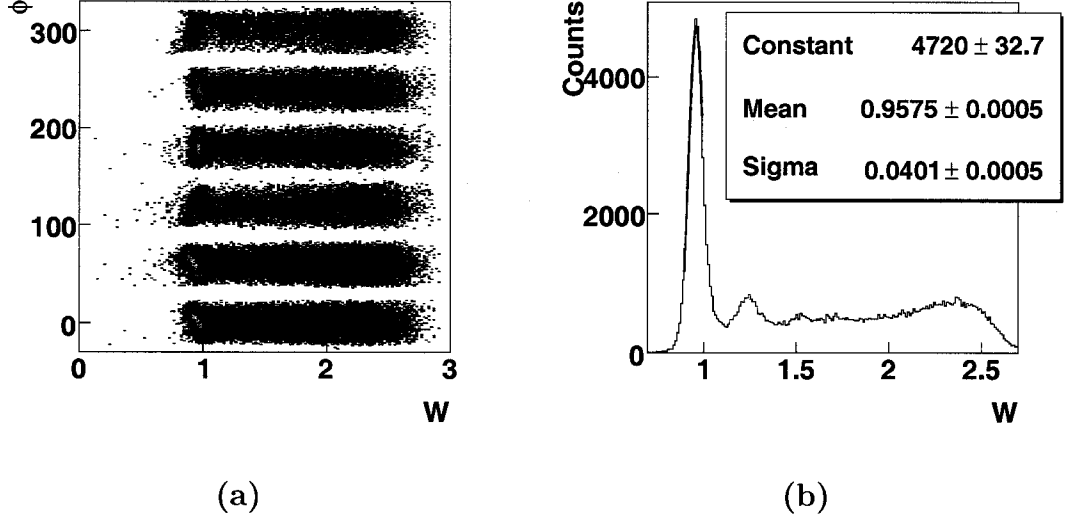
FIG. 38. a) W versus electron polar angle ϕ for ^{1}H(e, e') without electron momentum and angle corrections. b) W of the data without angle and momentum corrections.

where c_1–c_{14} are free parameters of the fit (indexes rec - reconstructed, cor - corrected). B_{torus} is a parametrization of the integral $\int Bdl$ along the path of the track. From the CLAS design

$$B_{torus} = 0.76 \cdot \frac{I_{torus} \sin^2 4\theta}{3375 \cdot \theta/\text{rad}} \quad \text{for} \quad \theta < \pi/8$$

$$B_{torus} = 0.76 \cdot \frac{I_{torus}}{3375 \cdot \theta/\text{rad}} \quad \text{for} \quad \theta > \pi/8$$

Parameters c_1 – c_8 correct for the drift chamber displacements and rotations. These errors cause angle and momentum miscalculation. Parameters c_9 through c_{14} parametrize the magnetic field errors. The parameters were found by minimization of χ^2 by "$Minuit$" for four momentum conservation. Minimization has been done on three reactions:

- Elastic scattering on Hydrogen: $ep \rightarrow e'p$

- Two pion production on Hydrogen: $ep \rightarrow e'p\pi^+\pi^-$

- Pion production on ^{3}He: ^{3}He$(e, e'pppπ^-)$

The two last reactions are needed to ensure the validity of the obtained corrections over the full momentum and angular distribution. As a result of the applied corrections, the H(e, e') resolution improves from 40 MeV to 25 MeV and the peak position is now very close to the proton mass (see Fig. 39). From the picture one can see that W no longer depends on ϕ and is nicely aligned around the proton mass. Table V shows the obtained constants.

| Constant | 3188 ± 34.5 |
| Mean | 0.939 ± 0.000 |
| Sigma | 0.02443 ± 0.00037 |

(a)   (b)
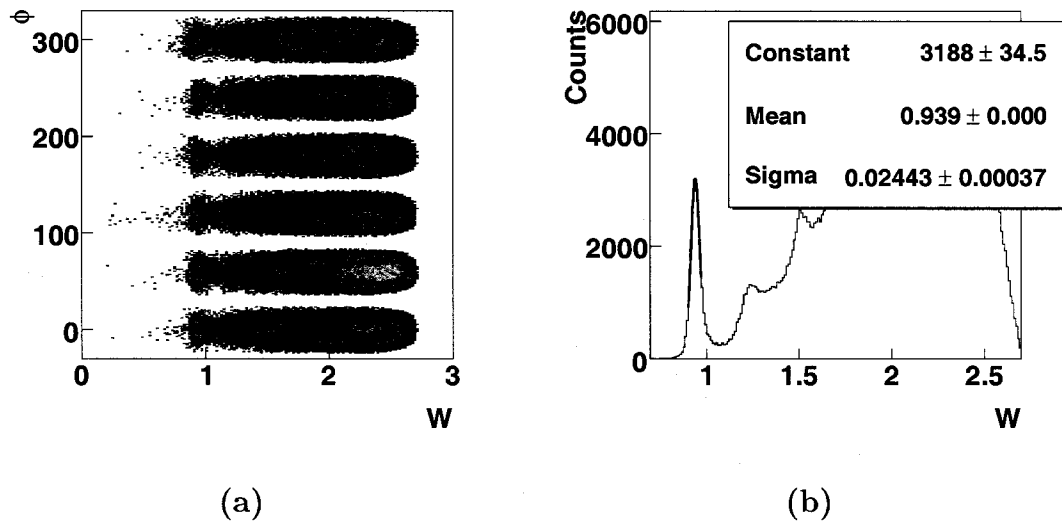
FIG. 39. a) W versus electron polar angle ϕ for ^{1}H(e, e') with electron momentum and angle corrections. b) W of the data with angle and momentum corrections.

4.2.3 Energy Loss corrections

Any charged particle interacts electromagnetically with the material it passes through. These materials include the target, the detectors and air. These interactions cause the particle to lose energy. These energy losses are more significant for lower momentum, heavier particles (ie: protons). The detector simulator (GSIM) was used to simulate the events in the detector (this procedure is explained more precisely in Section 4.4.4). Figure 40(a) shows the difference in energy between the generated

TABLE V. Angle and momentum correction constants.

$\cdot 10^{-5}$	c_1	c_2	c_3	c_4
Sector 1	-9.54655	-27.8829	-141.7	-62.0733
Sector 2	37.9975	88.2697	-229.717	5.31067
Sector 3	-3.05457	-135.789	32.407	18.6973
Sector 4	-40.5349	-2.54204	-124.74	38.9074
Sector 5	-109.628	-128.235	-207.319	-52.331
Sector 6	-157.607	-354.526	-127.554	-52.1634

$\cdot 10^{-5}$	c_5	c_6	c_7	c_8
Sector 1	865.839	-3375.77	-19.0066	4565.19
Sector 2	-505.125	-2529.12	-15.3021	3235.1
Sector 3	938.661	1304.66	-124.297	198.597
Sector 4	-9.97584	911.339	138.498	-1625.4
Sector 5	413.864	-1006.47	414.515	1459.59

$\cdot 10^{-5}$	c_9	c_{10}	c_{11}	c_{12}	c_{13}	c_{14}
Sector 1	546.675	-222.309	64.5633	-310.522	-113.619	-161.956
Sector 2	21.2449	-35.5547	80.9621	-151.382	-167.485	-230.555
Sector 3	86.9729	-133.971	-166.566	-315.323	-146.785	-189.392
Sector 4	681.076	-43.7384	-83.9906	28.5154	-212.511	-123.338
Sector 5	447.952	219.254	115.612	-574.407	-199.147	-296.385
Sector 6	809.07	-74.516	-209.934	165.508	21.6215	129.673

and reconstructed protons as a function of proton momentum. The correction was calculated by fitting the distribution shown in Figure 40(a) with the function $a_1 + a_2/(p + a_3)^2$. Figure 40(b) shows the spectrum after correction with the function

$$dE = 0.0015 + 0.0005/(p + 0.2)^2$$

where p is in GeV/c and dE is in GeV.
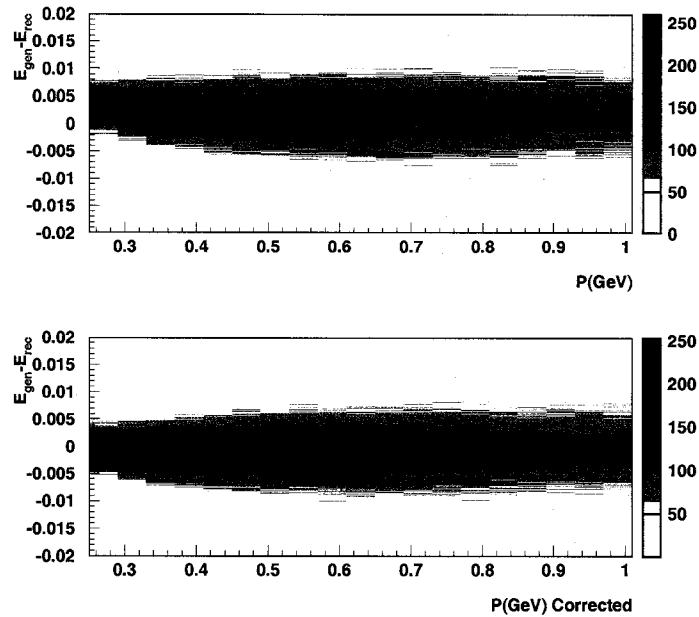
FIG. 40. Energy difference between generated and reconstructed protons plotted versus proton momentum. a) uncorrected, b) corrected.

4.2.4 Vertex Correction and Cut

To avoid events from reactions in the walls of the target, it is necessary to make cuts on the interaction vertex. The identification of the interaction vertex is done by the reconstruction program. Unfortunately, the reconstruction code extrapolates the track to the z axis, while the beam can be offset from there. The effect of this offset can be seen in Fig 41(a) where the ϕ dependence of the reconstructed vertex is shown. The beam is clearly shifted toward sector 6 ($\phi \approx -60°$).

We corrected the data for two effects. First the target was shifted from the center of CLAS by 2 cm downstream. Second, the beam was shifted (in software) by an

(a)   (b)
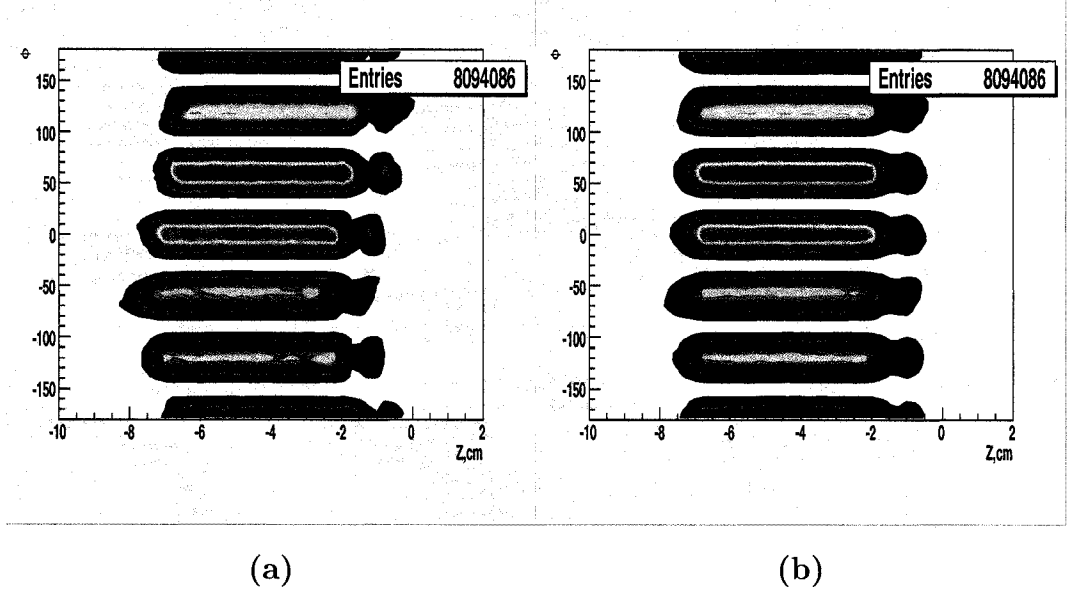
FIG. 41. Azimuthal angle vs interaction vertex along the beam line, z. a) Uncorrected, b) Corrected for the effects of beam displacement.

offset r in the direction ϕ_{off} from the z axis. From this simple geometrical assumption we get the functional form for the correction

$$z_{\text{cor}} = z_{\text{rec}} + \frac{r}{\tan\theta}\cos(\phi - \phi_{\text{off}}) \tag{55}$$

where z_{cor} is the corrected vertex, and θ and ϕ are the polar and azimuthal angles of the scattered particle. The position of the beam (r,ϕ_{off}) was found by fitting the distribution of the average vertex over the 6 sectors. The beam was shifted by $r = 1.624$ mm in the direction of the 6th sector ($\phi_{\text{off}} = -54.5^o$). The corrected vertex distributions are presented in Fig 41(b).

The vertex cut $Z \in [-6.5 : -2.5]$ cm was applied to avoid events coming from interaction with the aluminum walls of the target.

4.2.5 Event Identification

In order to identify $^3\text{He}(e,e'pp)n$ events, we first identified the trigger electrons using the cuts described in sections 4.2.1 and 4.3 to eliminate the pion contribution

and to select the region of the detector with constant efficiency.
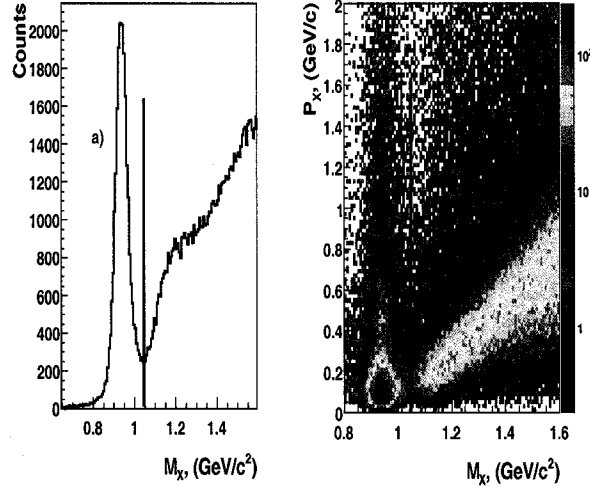
FIG. 42. Missing neutron identification cut. a) Missing mass of $^3\text{He}(e, e'pp)$ system, b) Missing mass of $^3\text{He}(e, e'pp)$ system versus Missing momentum.

To identify the protons we applied a loose cut on the proton velocity

$$|\beta_{rec}/\beta_{cal} - 1| < 0.1 \quad .$$

Figure 43(a) shows $\beta_{rec}/\beta_{cal} - 1$ versus the momentum of the particle, where β_{rec} is the measured velocity of the particle and β_{cal} is the velocity calculated using the measured momentum of the particle assuming it is a proton. Figure 43(a) shows there is still a contribution from high energy pions at high momenta.

Next we plot the $^3\text{He}(e, e'pp)$ missing mass M_X, where

$$M_X{}^2 = (\mathbf{p_e} - \mathbf{p_{e'}} - \mathbf{p_{p_1}} - \mathbf{p_{p_2}})^2$$

and $\mathbf{p_e}, \mathbf{p_{e'}}, \mathbf{p_{p_1}}, \mathbf{p_{p_2}}$ are the four momenta of the initial and scattered electron and the two detected protons. Figure 42 (a) shows the clean neutron mass peak; moreover Figure 42 (b) shows that the separation of the neutron is good even at large missing momenta. The cut on missing mass $M_X < 1.05$ GeV allows us to separate the $^3\text{He}(e, e'pp)n$ events. Figure 43(b) shows $\beta_{rec}/\beta_{cal} - 1$ versus momentum after the missing mass cut. The requirement of exclusivity in the reaction $^3\text{He}(e, e'pp)$ cleans the large momentum protons from pion contamination.

4.3 FIDUCIAL CUTS

We apply fiducial cuts to eliminate regions where the detection efficiency is changing rapidly. We chose a functional form for the cuts which corresponds to the geometry of CLAS. The idea was that if the magnet coil width is d and the distance from the target to the near edge of the magnet coil is R, then from the geometry we can say that

$$d/\sin\varphi = R\sin\theta$$

hence

$$\sin\varphi = d/(R\sin\theta)$$

so that

$$\varphi \approx a_o/\sin(\theta - \theta_o)$$

where φ is the angle occluded by the magnet coil and the θ_o term comes from the curvature of our detector. All cuts will be represented by a function

$$\varphi^+ = 30° - a_o/\sin(\theta - \theta_o)$$

and

$$\varphi^- = -30° + a_1/\sin(\theta - \theta_1)$$

where $30°$ and $-30°$ are the φ limits of each sector. φ is measured relative to each sector. The electron Fiducial Cuts were obtained by Alexei Klimenko and well described in [55]. The function in C and Fortran is included in an Appendix.

4.3.1 Positive Particles

We also needed to establish fiducial cuts for positive (ie: out-bending) particles. To do this, we needed to select good uncorrelated positive particles. To select "good" positive particles we require a good DC track and a hit in the TOF counters. To eliminate angle-correlated quasi-elastic scattering for this analysis, we required $x_B < 0.65$ for the electron in that event. We divided events into bins of proton momentum:

$$p = 0.5, 0.7, 0.9, 1.1, 1.3, 1.5 \pm 0.1 \text{ GeV/c},$$

$$p = 1.8 \pm 0.2, 2.4, 3.2 \pm 0.4 \text{ GeV/c}.$$

Each momentum bin was divided into 70 θ bins in the range from 0 to 140°, and 60 φ bins in the range from -30 to 30° for each sector. For each θ bin, the φ distribution was plotted and fitted with a trapezoid function to determine the limits of the φ acceptance (φ^+ and φ^-) for that (θ, p) bin (see Figures 44–55). In order to get smooth variation of the φ acceptance as a function of θ, we fit the function $f^\pm(\theta)$ to the $\{\varphi^+, \varphi^-\}$ trapezoid fit results.

$$\varphi^\pm = f^\pm(\theta) = \begin{cases} 30° - \frac{4.5}{\sin(\theta-\theta_1)} \longrightarrow \varphi^+ \subset [0:30] \\ -30° + \frac{3.5}{\sin(\theta-\theta_2)} \longrightarrow \varphi^- \subset [-30:0] \end{cases} \text{ for } f(\theta) < 24°$$

If $|\varphi^\pm| > 24°$ then $\varphi^\pm = \pm 24°$. For the backward region ($\theta > 100°$) we used the function

$$\varphi^\pm = \pm \left[\frac{14}{100-c_1}\theta + 24° - \frac{1400°}{100-c_1} \right]$$

to obtain the θ dependence.

In order to get a smooth variation of the φ acceptance as a function of both θ and p, we fit the parameters from the previous step with polynomials (rejecting tracks at $\theta < 12°$)

$$\theta_1 = \frac{a_1}{p} + a_2 + a_3 \cdot p + a_4 \cdot p^2$$

$$\theta_2 = \frac{b_1}{p} + b_2 + b_3 \cdot p + b_4 \cdot p^2$$

$$c_1 = -\frac{1.3}{p} + 140$$
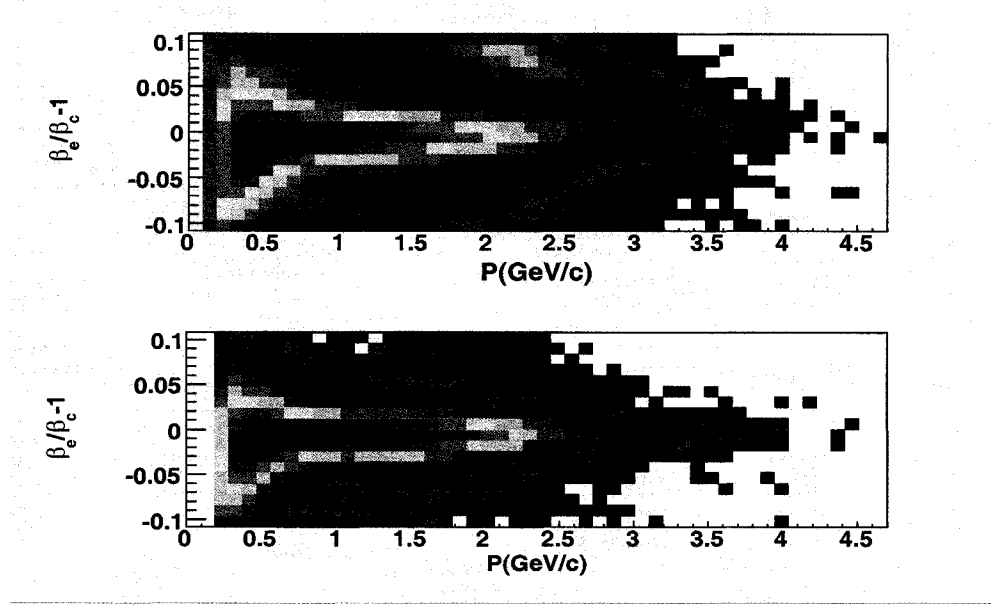
FIG. 43. Proton identification. $\beta_{rec}/\beta_{cal} - 1$ versus momentum a) with loose cut on velocity b) plus additional cut on missing mass of system $^3\text{He}(e, e'pp)$

TABLE VI. Proton Fiducial Cut Parameters for all Sectors.

S\P	a_1	a_2	a_3	a_4	b_1	b_2	b_3	b_4
1	3.167	-2.221	0.8148	-0.06501	4.552	-6.545	5.149	-1.001
2	4.011	-2.665	0.3932	-0.01107	1.082	2.867	-1.737	0.4061
3	6.596	-9.504	2.844	-0.3419	2.364	-0.3386	-0.08948	0.1852
4	2.826	0.8345	-4.739	1.139	2.95	-0.814	0.9138	-0.1422
5	4.5659	-4.1917	-1.2117	0.37767	4.0755	-1.0917	2.7285	-0.45658
6	4.951	-3.372	0.3257	-0.01724	1.463	7.221	-5.461	1.255

FIG. 44. Trapezoid fit for low momenta protons in sector 1. The histogram shows the data, dashed lines the trapezoid fit and the solid vertical lines show the final cut. The histograms show the ϕ distribution for θ bins starting from 17° with two degree increment.

Sector 1 P$_p$=3.2Gev/c

FIG. 45. Trapezoid fit for high momenta protons in sector 1. The histogram shows the data, dashed lines the trapezoid fit and the solid vertical lines show the final cut. The histograms show the ϕ distribution for θ bins starting from 12° with two degree increment.

Sector 2 P$_p$=0.5Gev/c

FIG. 46. Trapezoid fit for low momenta protons in sector 2. The histogram shows the data, dashed lines the trapezoid fit and the solid vertical lines show the final cut. The histograms show the ϕ distribution for θ bins starting from 17° with two degree increment.

FIG. 47. Trapezoid fit for high momenta protons in sector 2. The histogram shows the data, dashed lines the trapezoid fit and the solid vertical lines show the final cut. The histograms show the ϕ distribution for θ bins starting from 12° with two degree increment.
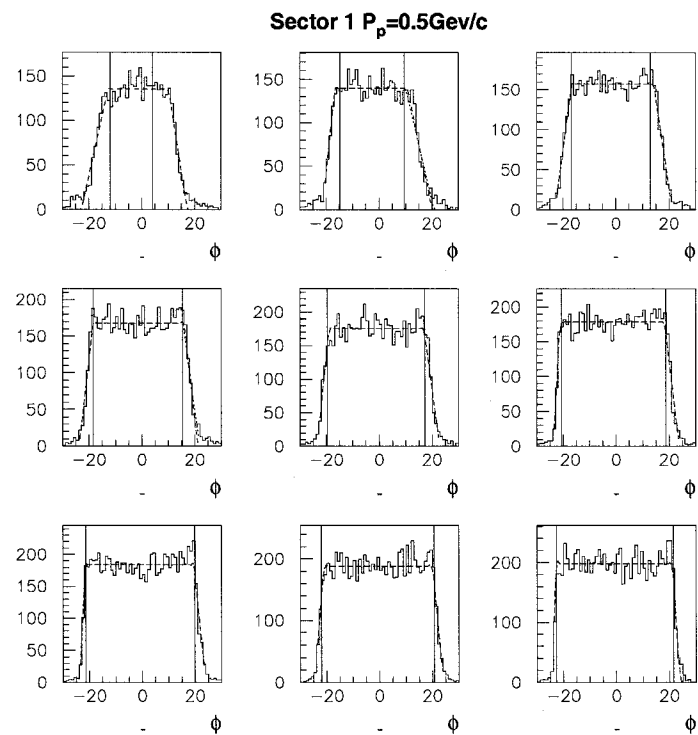
FIG. 48. Trapezoid fit for low momenta protons in sector 3. The histogram shows the data, dashed lines the trapezoid fit and the solid vertical lines show the final cut. The histograms show the ϕ distribution for θ bins starting from 17° with two degree increment.
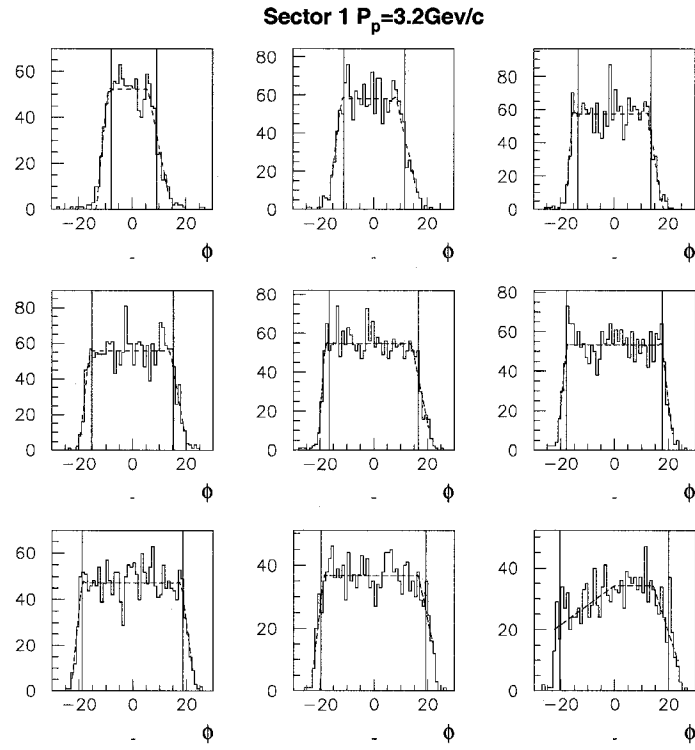
FIG. 49. Trapezoid fit for high momenta protons in sector 3. The histogram shows the data, dashed lines the trapezoid fit and the solid vertical lines show the final cut. The histograms show the ϕ distribution for θ bins starting from 12° with two degree increment.
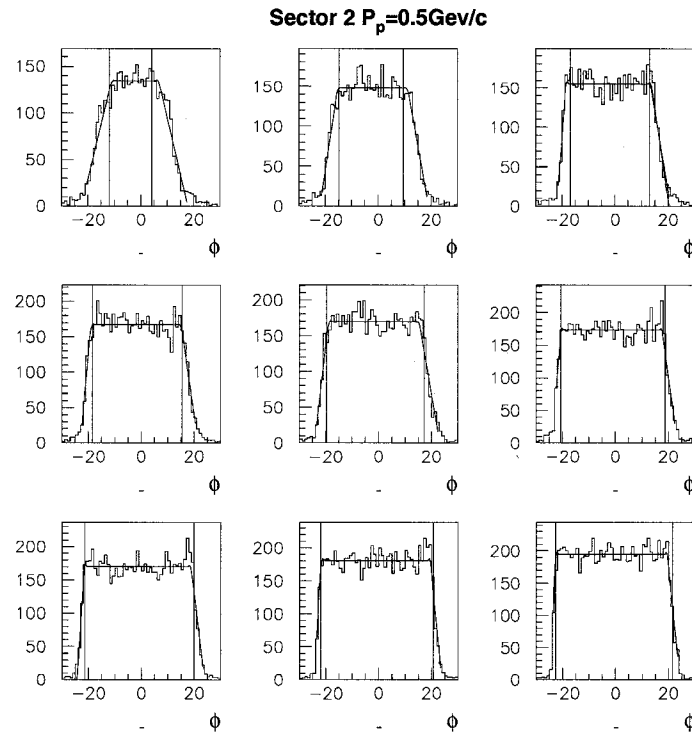
Sector 4 P$_p$=0.5Gev/c

FIG. 50. Trapezoid fit for low momenta protons in sector 4. The histogram shows the data, dashed lines the trapezoid fit and the solid vertical lines show the final cut. The histograms show the ϕ distribution for θ bins starting from 17° with two degree increment.

Sector 4 P$_p$=3.2Gev/c

FIG. 51. Trapezoid fit for high momenta protons in sector 4. The histogram shows the data, dashed lines the trapezoid fit and the solid vertical lines show the final cut. The histograms show the ϕ distribution for θ bins starting from 12° with two degree increment.

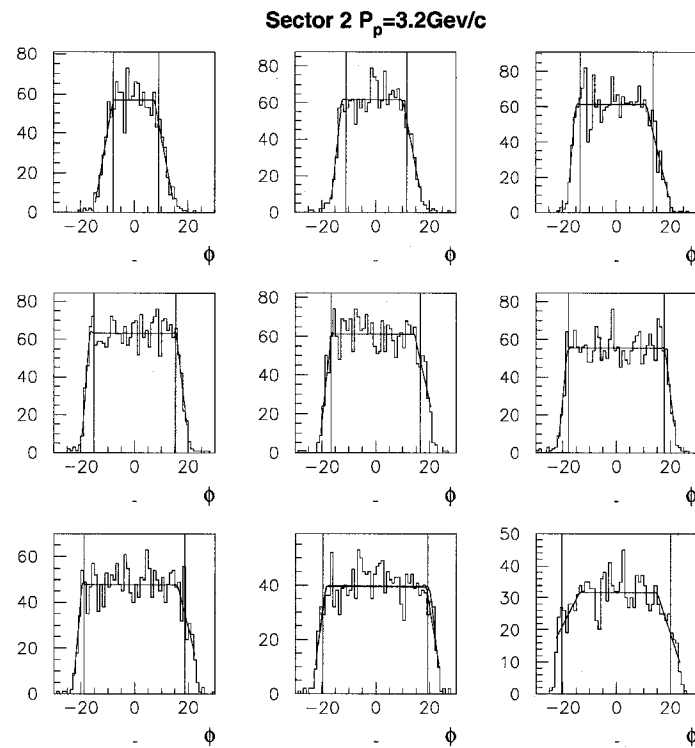**Sector 5 P$_p$=0.5Gev/c**

FIG. 52. Trapezoid fit for low momenta protons in sector 5. The histogram shows the data, dashed lines the trapezoid fit and the solid vertical lines show the final cut. The histograms show the ϕ distribution for θ bins starting from 17° with two degree increment.

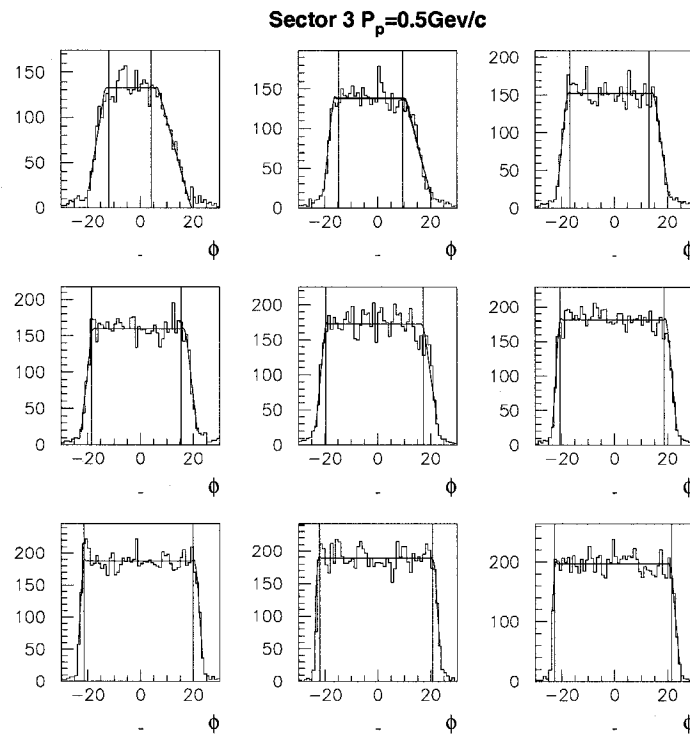
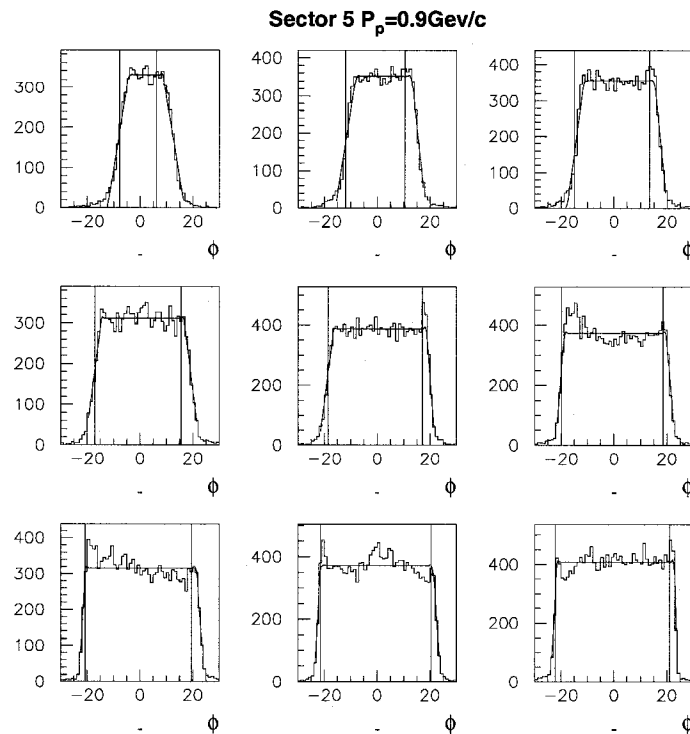
FIG. 53. Trapezoid fit for high momenta protons in sector 5. The histogram shows the data, dashed lines the trapezoid fit and the solid vertical lines show the final cut. The histograms show the ϕ distribution for θ bins starting from 12° with two degree increment.

Sector 6 P_p=0.5Gev/c
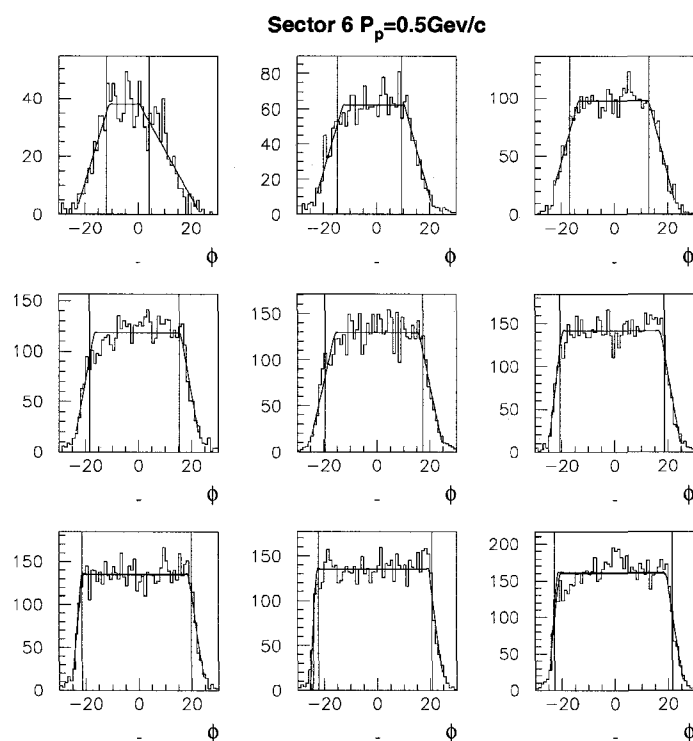
FIG. 54. Trapezoid fit for low momenta protons in sector 6. The histogram shows the data, dashed lines the trapezoid fit and the solid vertical lines show the final cut. The histograms show the ϕ distribution for θ bins starting from 17° with two degree increment.
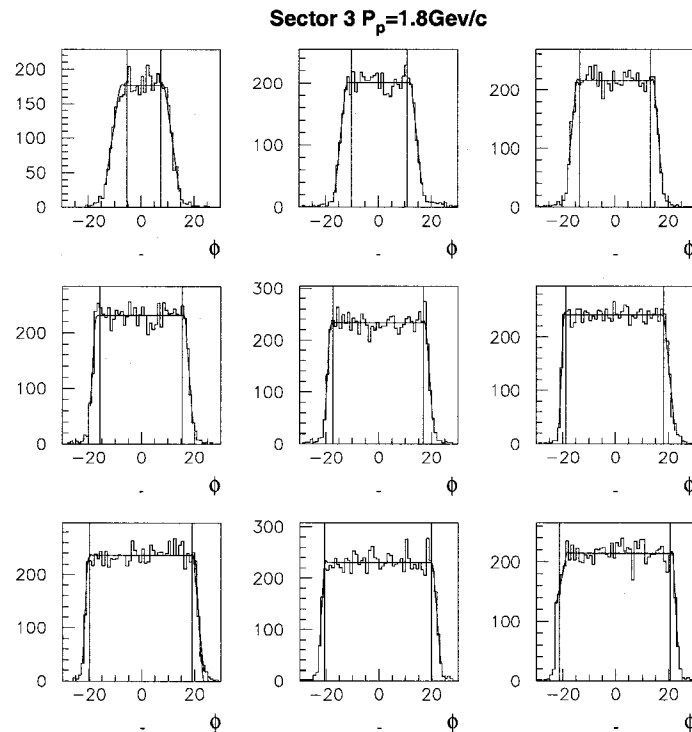
FIG. 55. Trapezoid fit for high momenta protons in sector 6. The histogram shows the data, dashed lines the trapezoid fit and the solid vertical lines show the final cut. The histograms show the ϕ distribution for θ bins starting from 12° with two degree increment.

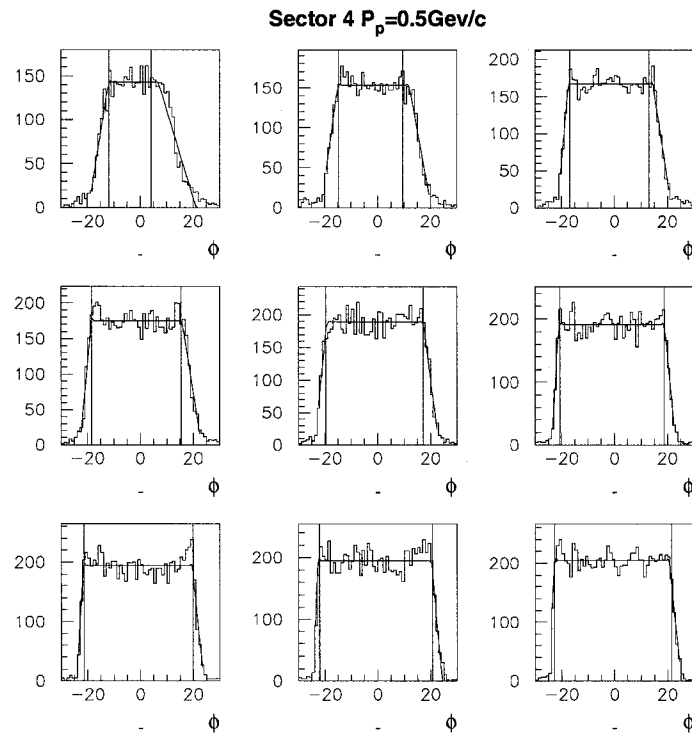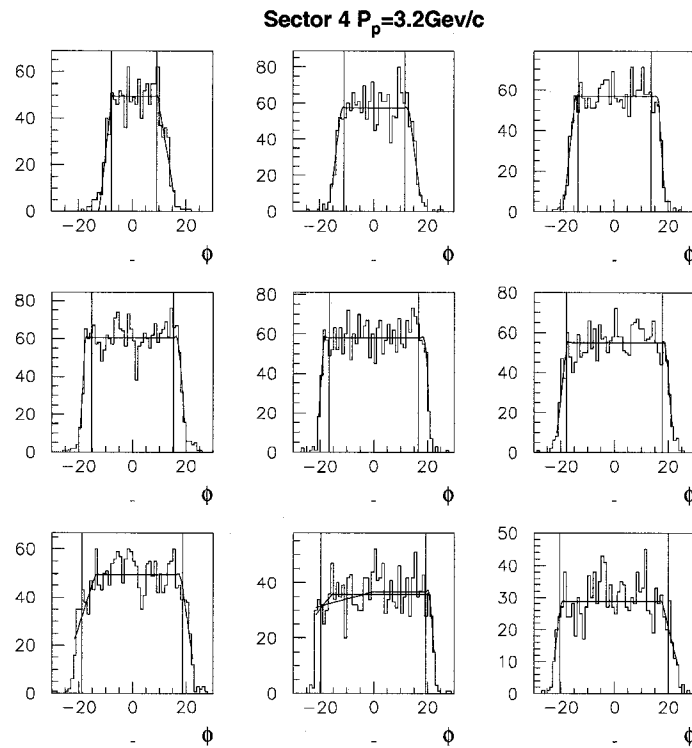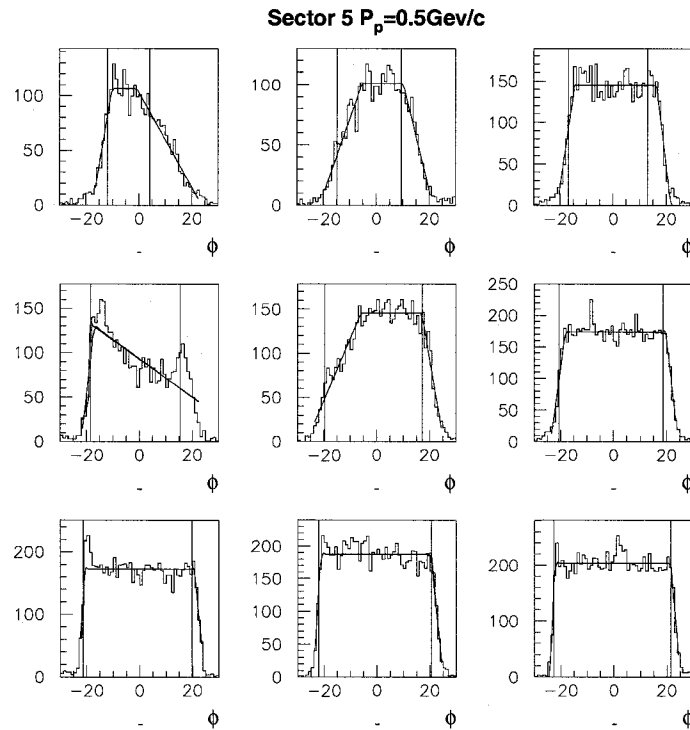**Sector 1**

χ^2/ndf	1.784	/	5
P1			3.167
P2			−2.221
P3			0.8148
P4			−0.6501E−01

χ^2/ndf	3.339	/	5
P1			4.552
P2			−6.545
P3			5.149
P4			−1.001

FIG. 56. Fitted parameters θ_1 and θ_2 for sector 1.

Sector 2

χ^2/ndf	5.214	/	5
P1			4.011
P2			−2.665
P3			0.3932
P4			−0.1107E−01
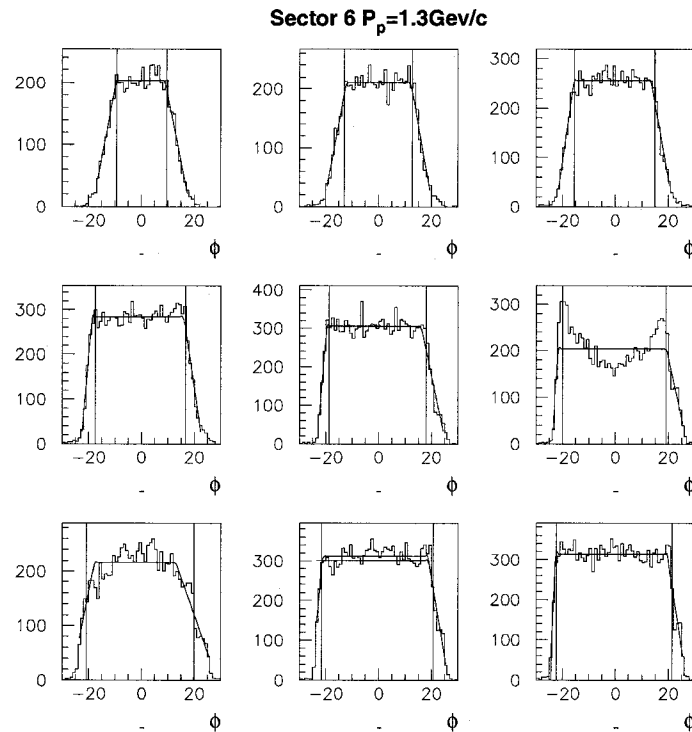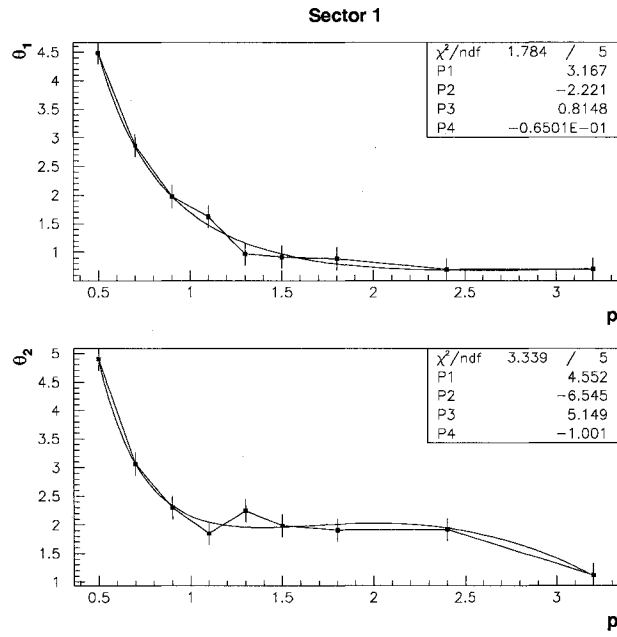
χ^2/ndf	25.08	/	5
P1			1.082
P2			2.867
P3			−1.737
P4			0.4061
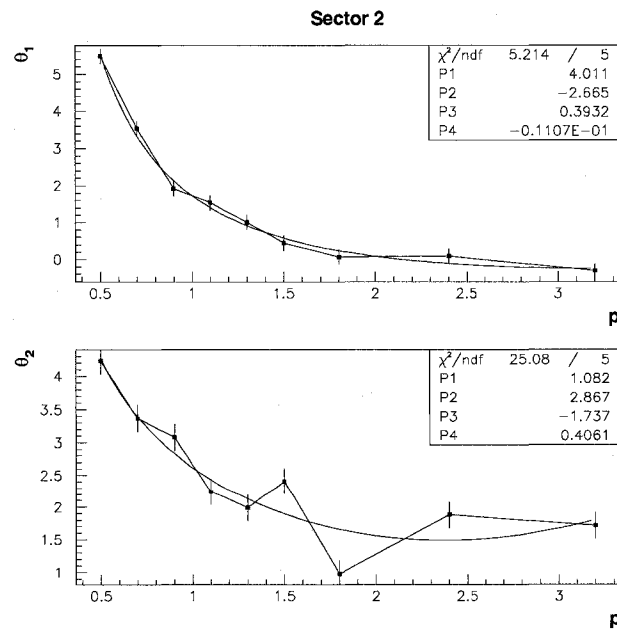
FIG. 57. Fitted parameters θ_1 and θ_2 for sector 2.
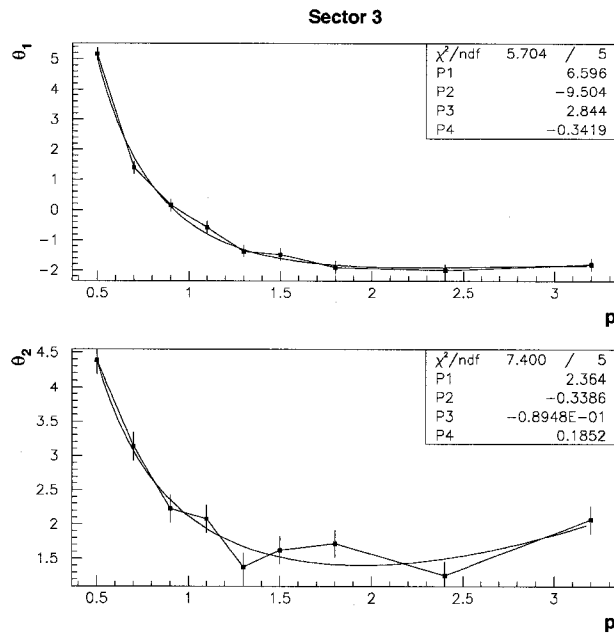
Sector 3

FIG. 58. Fitted parameters θ_1 and θ_2 for sector 3.
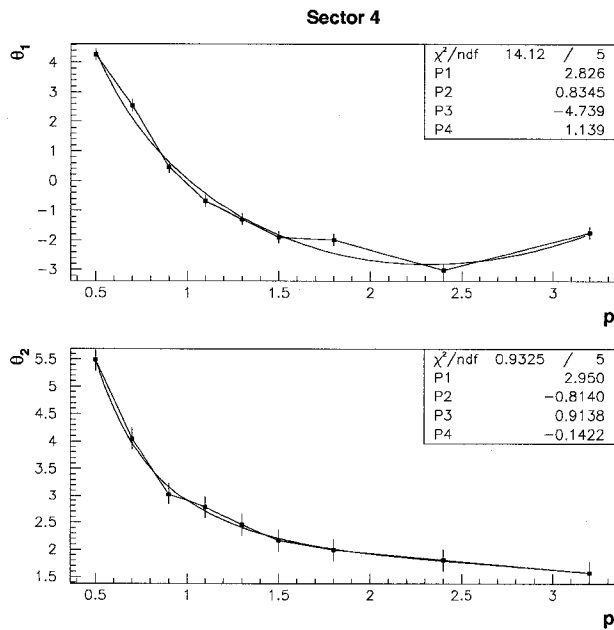
Sector 4

FIG. 59. Fitted parameters θ_1 and θ_2 for sector 4.
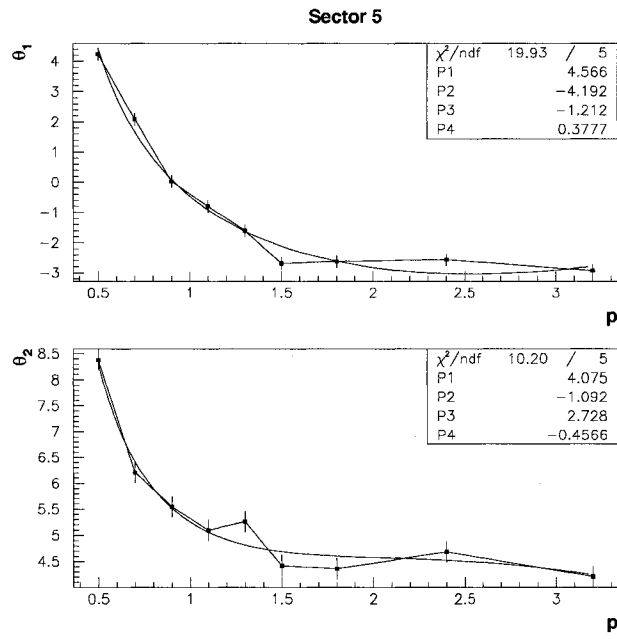
FIG. 60. Fitted parameters θ_1 and θ_2 for sector 5.
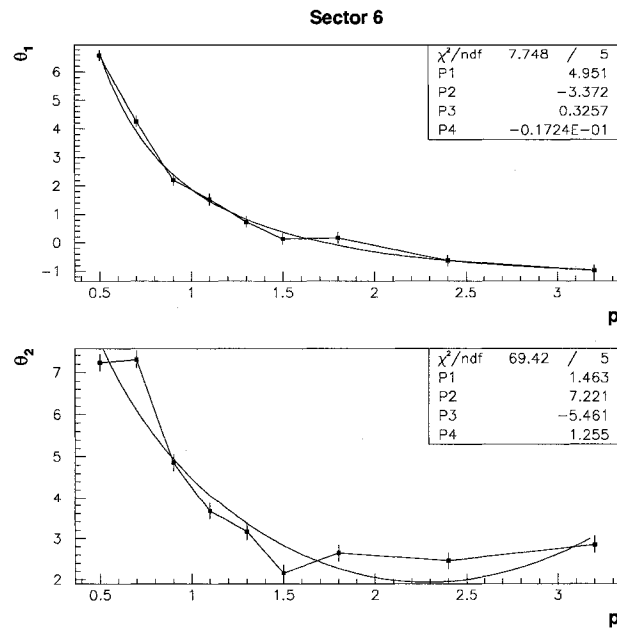
FIG. 61. Fitted parameters θ_1 and θ_2 for sector 6.
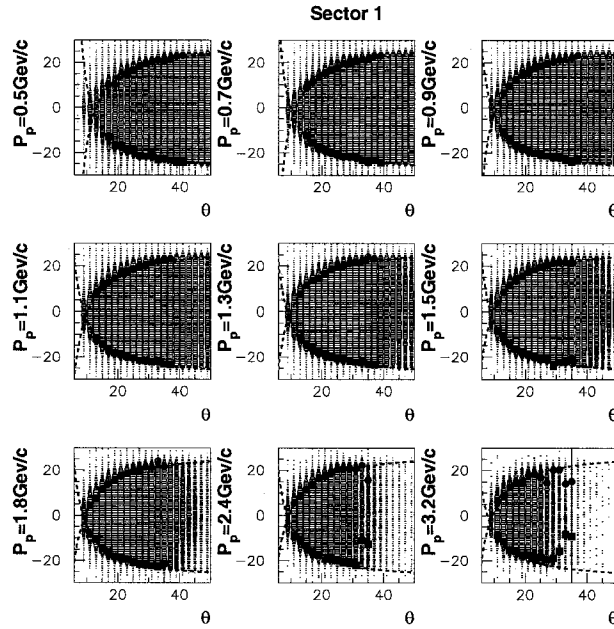
FIG. 62. Proton φ versus θ for sector 1. Green points indicate trapezoid fit limits. Pink lines represent cut corresponding to the function presented above.
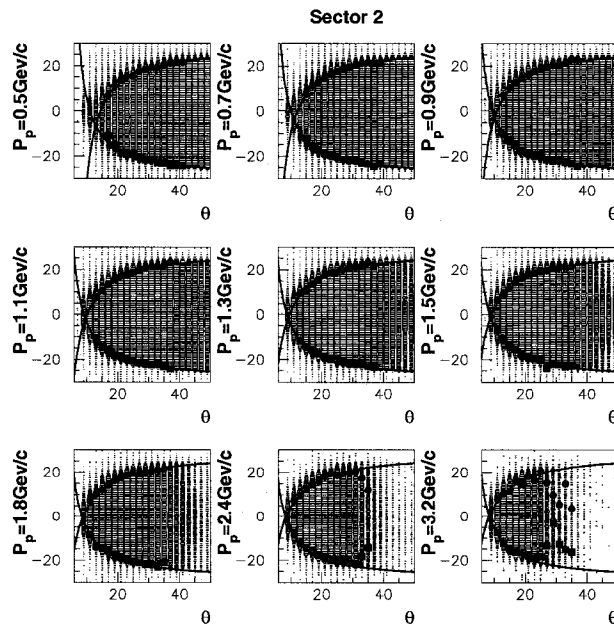
FIG. 63. Proton φ versus θ for sector 2. Green points indicate trapezoid fit limits. Pink lines represent cut corresponding to the function presented above.
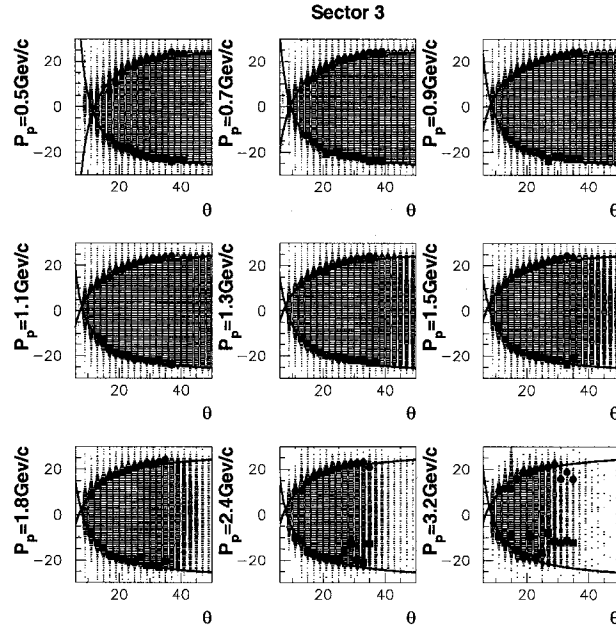
Sector 3

FIG. 64. Proton φ versus θ for sector 3. Green points indicate trapezoid fit limits. Pink lines represent cut corresponding to the function presented above.
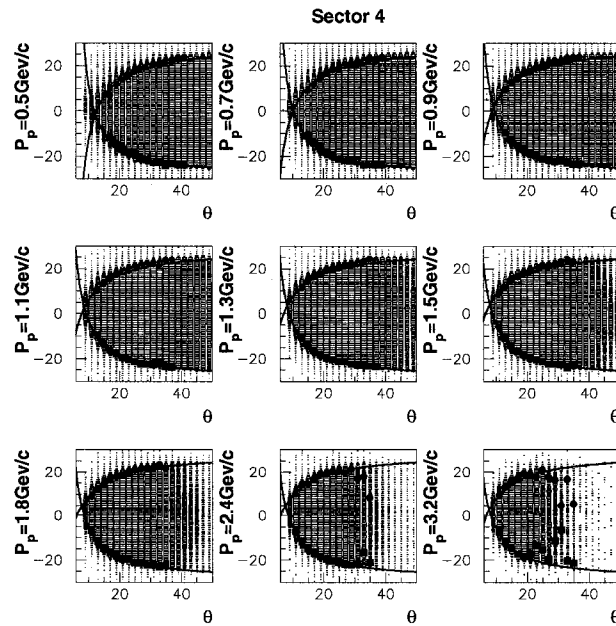
Sector 4

FIG. 65. Proton φ versus θ for sector 4. Green points indicate trapezoid fit limits. Pink lines represent cut corresponding to the function presented above.
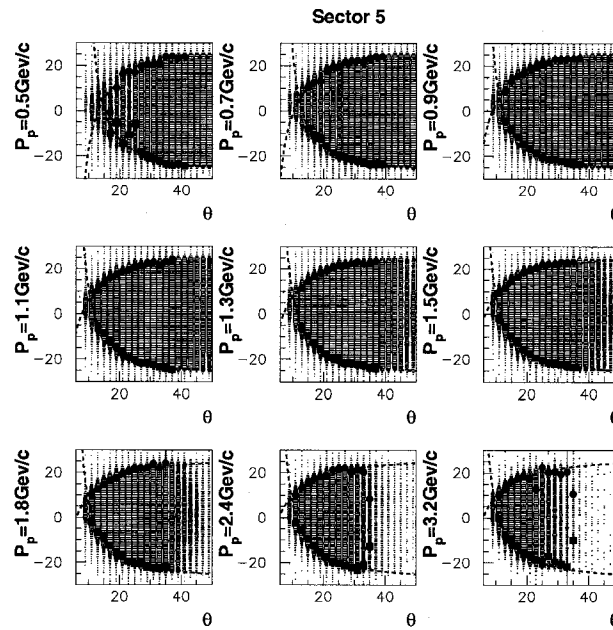
FIG. 66. Proton φ versus θ for sector 5. Green points indicate trapezoid fit limits. Pink lines represent cut corresponding to the function presented above.
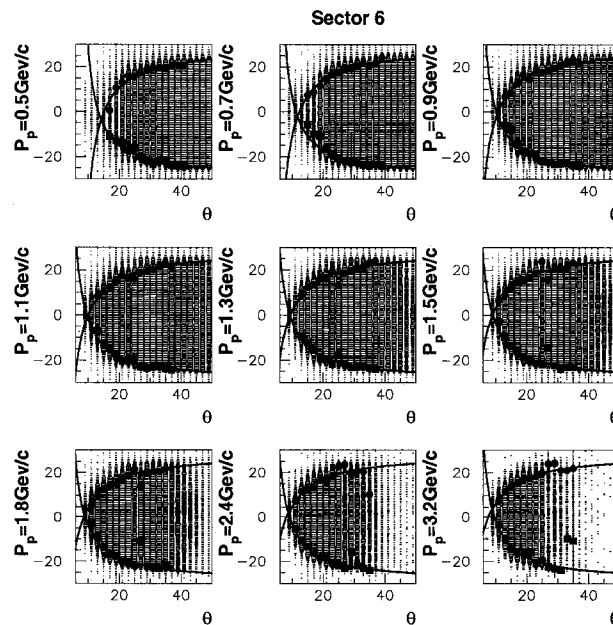
FIG. 67. Proton φ versus θ for sector 6. Green points indicate trapezoid fit limits. Pink lines represent cut corresponding to the function presented above.

4.4 EFFICIENCY

4.4.1 Efficiency of electromagnetic calorimeter cuts

We estimated the efficiency of the electromagnetic calorimeter for identifying electrons using the $^1\text{H}(e, e')$ reaction. We plotted the invariant mass W for each sector for all events and for events with EC cuts

$$EC_{tot}/P > 0.19$$

and

$$EC_{in}/P > 0.05$$

We fit the distributions with a Gaussian function (for elastic scattering) and a 4th order polynomial for the background estimation. The efficiency was calculated as the ratio of the number of events in the elastic peaks N_{all} and N_{cut}

$$\varepsilon_{ECcut} = N_{cut}/N_{all}$$

where N_{cut} is the integrated number of events after EC cuts, and N_{all} is the integrated number of events before EC cuts. Figures 68–70 show the invariant mass distributions before and after the EC cuts. Table VII shows the efficiencies for EC cuts. The efficiencies are about 95% and have uncertainties around 1–1.5% due to the fit uncertainty for the data after EC cuts. All efficiency calculations were done after the Fiducial Cuts.

4.4.2 Efficiency of the event reconstruction

There are situations where the particle which is registered as the trigger electron is not a real trigger electron. The real trigger electron is written into the data table as a secondary particle from the interaction. To estimate the number of events we are losing due to incorrect trigger electron identification, we plotted W for $^1\text{H}(e, e')$ for all other negative particles in the event that passed fiducial and EC cuts.

The non-physical background was fitted as a 4th order polynomial and subtracted from the data. The peak was fit with a Gaussian to give the number of lost electrons (N_{lost}). The same procedure was done for the trigger particles to give N_{trig}. The

Electron efficiency due to EC (in/tot) cuts = 95.27 percent

$EC_{tot}/p > 0.19$ and $EC_{in}/p > 0.05$

The Integral of Gaus = 5484

Electron efficiency due to EC (in/tot) cuts = 93.16 percent

$EC_{tot}/p > 0.19$ and $EC_{in}/p > 0.05$

The Integral of Gaus = 5157

a) a)

The Integral of Gaus = 5756

The Integral of Gaus = 5536

b) b)

(I) (II)
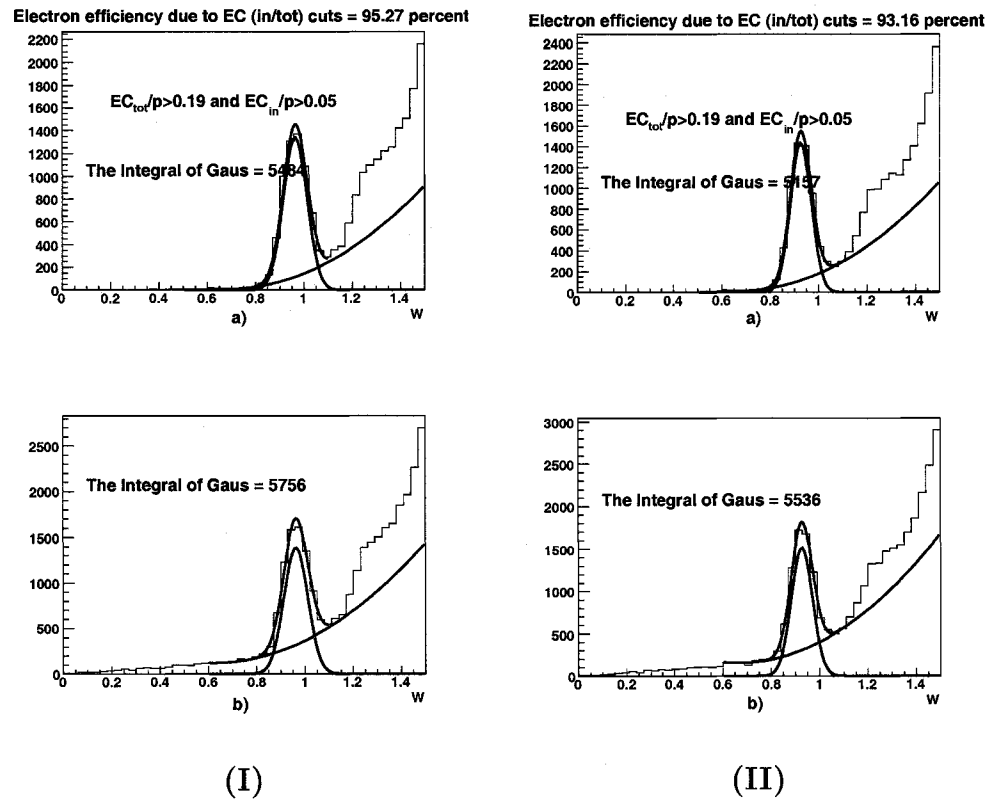
FIG. 68. Invariant mass W distributions. I) Sector 1, II) Sector 2, a) top: with calorimeter cuts b) without calorimeter cuts
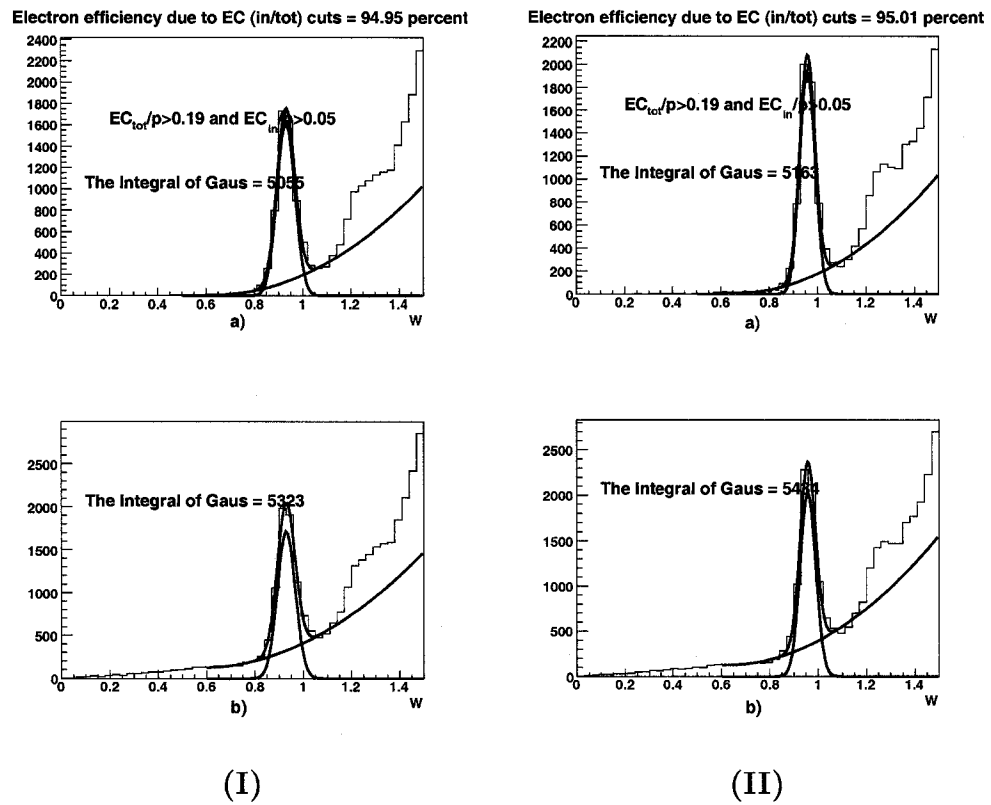
FIG. 69. Invariant mass W distributions. Invariant mass W distribution for I) Sector 3, II) Sector 4, a) top: with calorimeter cuts b) without calorimeter cuts

Electron efficiency due to EC (in/tot) cuts = 95.81 percent

$EC_{tot}/p>0.19$ and $EC_{in}/p>0.05$

The Integral of Gaus = 4575

a)

Electron efficiency due to EC (in/tot) cuts = 97.61 percent

$EC_{tot}/p>0.19$ and $EC_{in}/p>0.05$

The Integral of Gaus = 5083

a)

The Integral of Gaus = 4775

b)

The Integral of Gaus = 5208

b)

(I)

(II)
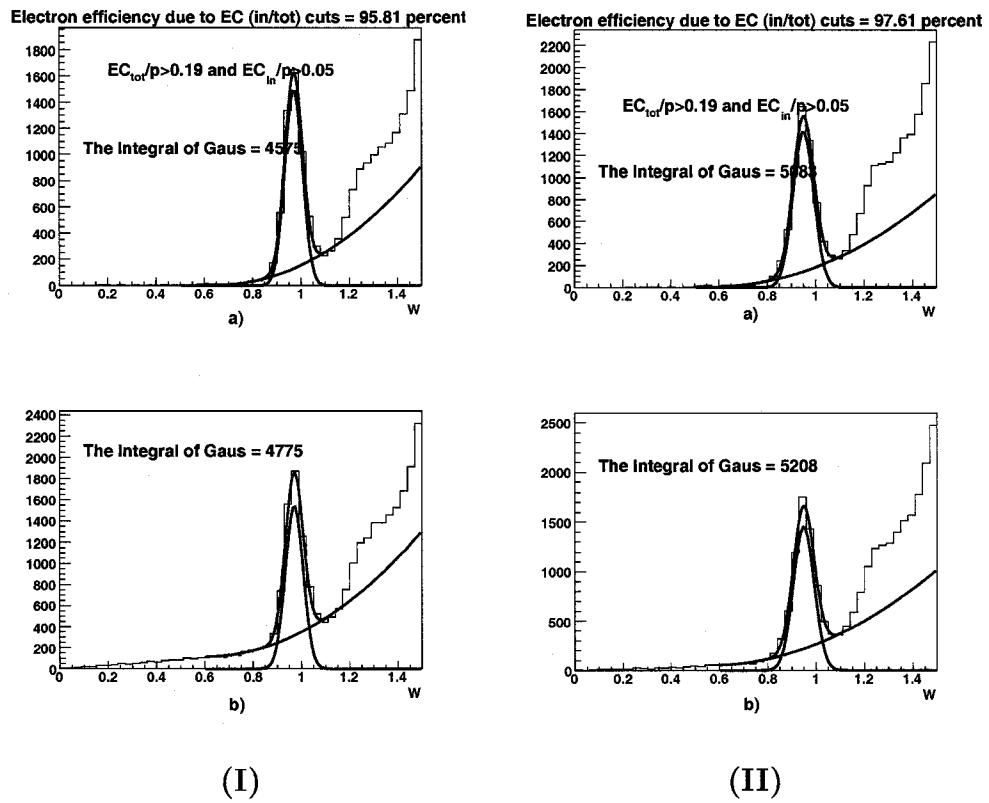
FIG. 70. Invariant mass W distributions. Invariant mass W distribution for I) Sector 5, II) Sector 6, a) top: with calorimeter cuts b) without calorimeter cuts

efficiency was calculated as:

$$\epsilon_{rec} = \frac{N_{trig}}{N_{lost} + N_{trig}}$$

Figure 71–73 shows the invariant mass W distributions for the trigger particle and the misidentified electrons. Table VII shows the efficiencies of the reconstruction. The event reconstruction efficiency is about 97% with an uncertainty of 0.5%.

(I)   (II)
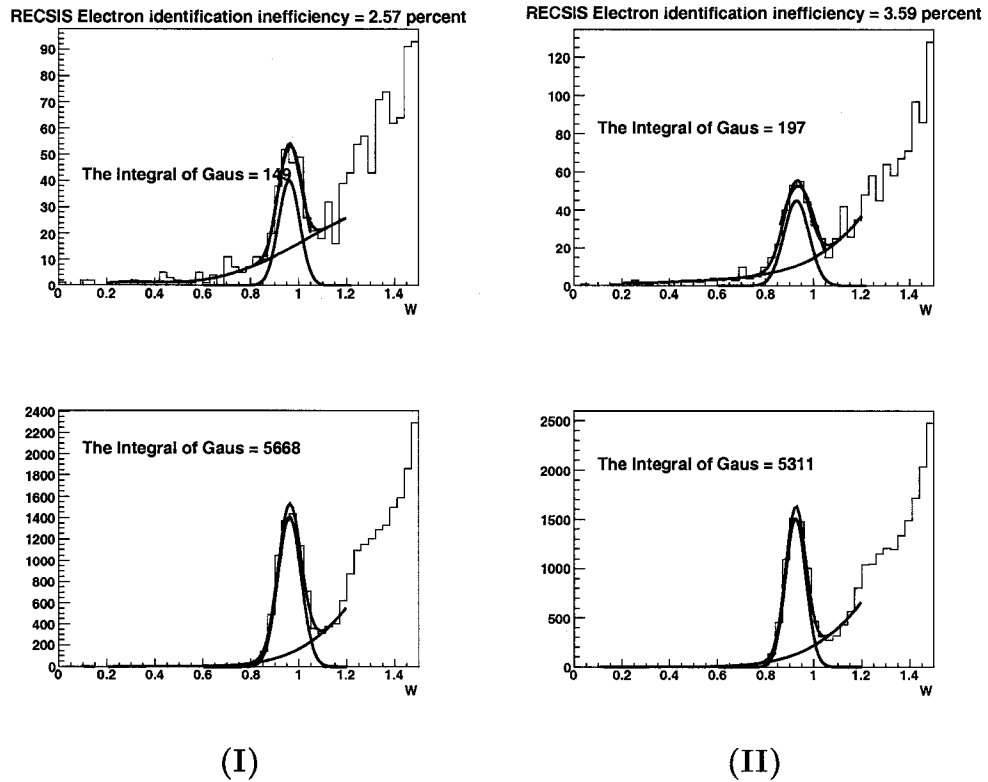
FIG. 71. Invariant mass W distribution for I) Sector 1, II) Sector 2, a) misidentified electrons, b) trigger electrons.

4.4.3 Electron Tracking Efficiency

We used GSIM, the CLAS GEANT simulation, to estimate the electron tracking efficiency, including the effects of bad detector channels. To do this, electrons were generated uniformly in space and in the momentum range from 0.8–4.7 GeV/c. The generated events were used as input into GSIM. The GSIM Post Processor (GPP)
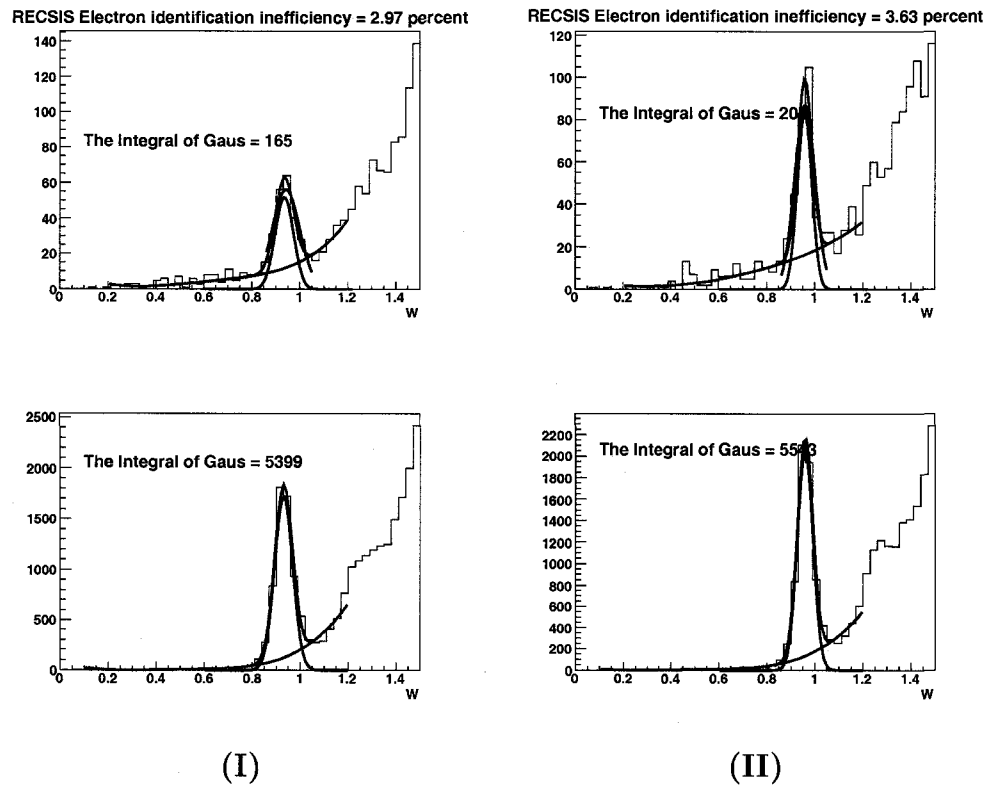
FIG. 72. Invariant mass W distribution for I) Sector 3, II) Sector 4, a) misidentified electrons, b) trigger electrons.

TABLE VII. Efficiency of EC cuts and reconstruction.

Sector	1	2	3	4	5	6
ε_{ECcut}	0.9527	0.9316	0.9495	0.9501	0.9581	0.9761
ϵ_{rec}	0.975	0.965	0.97	0.964	0.98	0.981
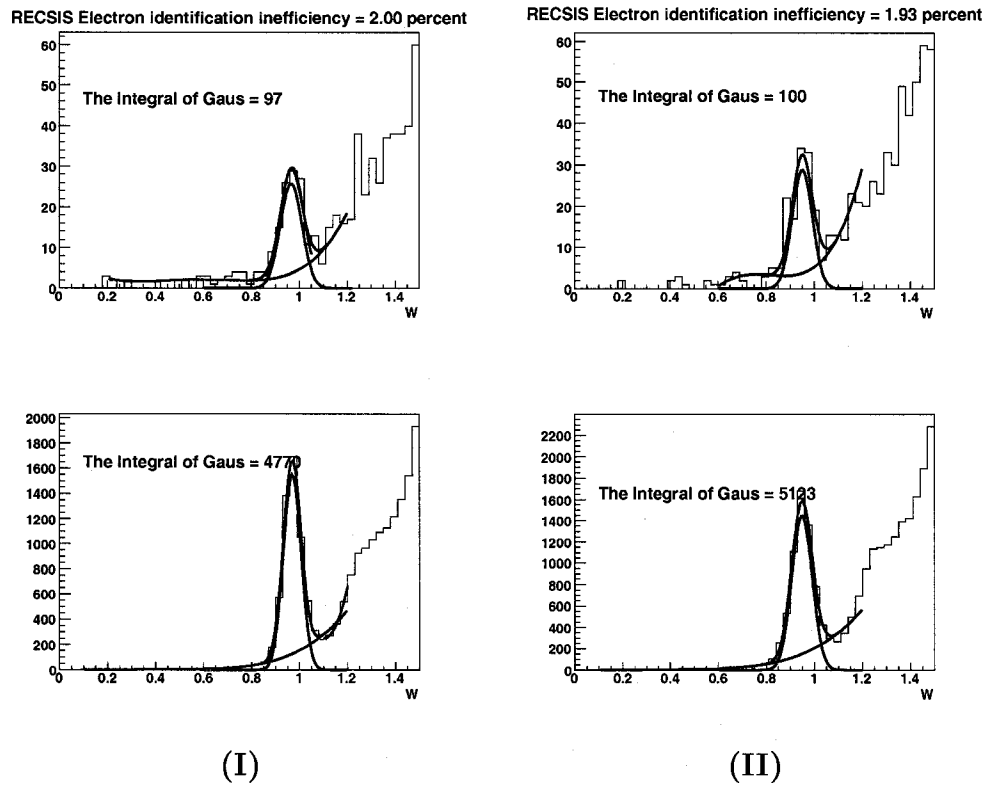
FIG. 73. Invariant mass W distribution for I) Sector 5, II) Sector 6, a) misidentified electrons, b) trigger electrons.

was used to take into account the dead drift chamber wires and scintillators. The events were reconstructed with RECSIS and the data was binned in momentum into bins of size 0.2 GeV/c. For each momentum bin, the scattering angle distribution was plotted within the fiducial cut for generated and for reconstructed events. The tracking efficiency is the ratio of reconstructed to generated events. Figures 74–79 show the normalization factors for the cross section for different sectors and different momentum bins.

To make sure that the tracking corrections are good, the cross section for elastic scattering on hydrogen was compared with the cross section obtained by the parametrization of the world's data [56]. Figure 80 shows the calculated and measured elastic cross section on hydrogen for different sectors after all electron corrections (efficiencies and radiative (explained in next chapter)). Figure 81 shows the ratio between the measured cross sections and the world data parametrization. The efficiency of the first bin in all sectors is highly underestimated because of the edge effect. In sector 3 (Figure 80(c)) there is a dead region in the DC which is not reproduced by GSIM (angular range 20–25 degrees). In sector 6 (Figure 80(f)) there are many dead DC wires which decreases the efficiency. Sector 2 had the highest efficiency.

We determined the final electron efficiency correction in two parts. The angular range was divided, the first part (15–31^0) with good statistics and the second part (31^0 and up) with bad statistics. The efficiency constants for the first region were obtained by taking the ratio between the experimental data and the world cross section at each angle for each sector.

For the second region we assumed that the cross section obtained for sector 2 is perfect. The angular dependence (on Figure 80) of ^{1}H(e, e')X reaction was constructed for each sector and normalized to the angular dependence in sector 2 (Figure 80(b)). Figure 82 shows the experimental cross section after the correction.

4.4.4 Proton Tracking Efficiency

Due to a lack of H$(e, e'p)$ statistics, the proton detection efficiency was calculated by two different ways (Simulation, H$(e, e'p)$ direct calculations). The procedure for

Sector 1

FIG. 74. Sector 1 electron detection correction factor for different momentum ranges (from GSIM).

FIG. 75. Sector 2 electron detection correction factor for different momentum ranges (from GSIM).

FIG. 76. Sector 3 electron detection correction factor for different momentum ranges (from GSIM).

FIG. 77. Sector 4 electron detection correction factor for different momentum ranges (from GSIM).

FIG. 78. Sector 5 electron detection correction factor for different momentum ranges (from GSIM).

FIG. 79. Sector 6 electron detection correction factor for different momentum ranges (from GSIM).
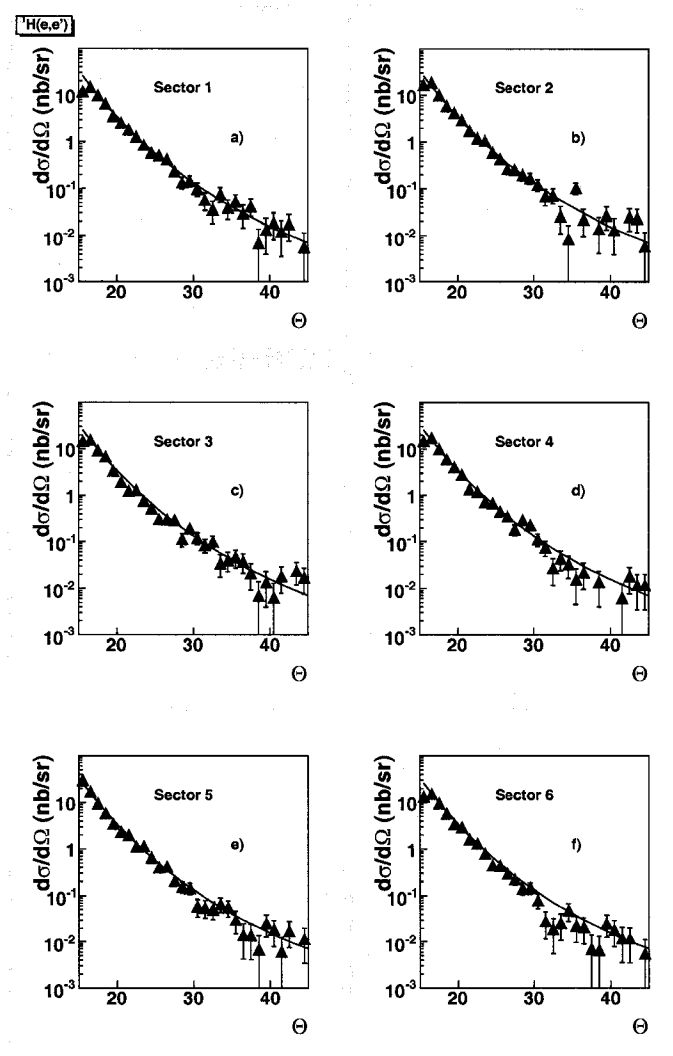
FIG. 80. Measured elastic cross section on hydrogen including electron event reconstruction, EC,tracking and radiative corrections. The curve is the theoretical parametrization; the data is experimental cross section.
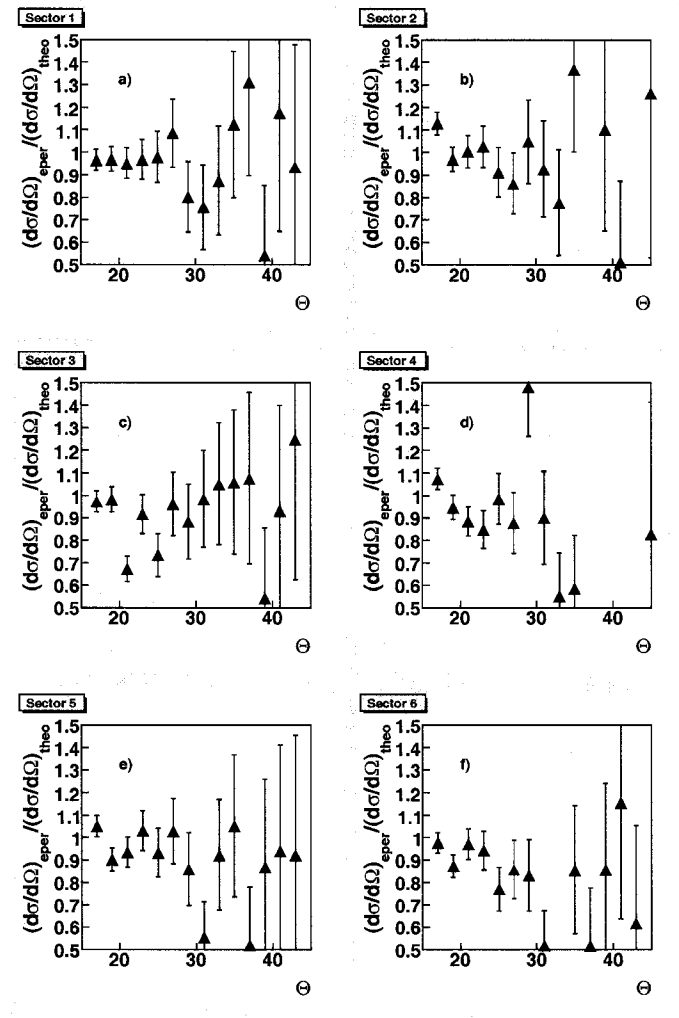
FIG. 81. Ratio between the measured and the theoretical parametrization of $^1\mathrm{H}(e, e')$.
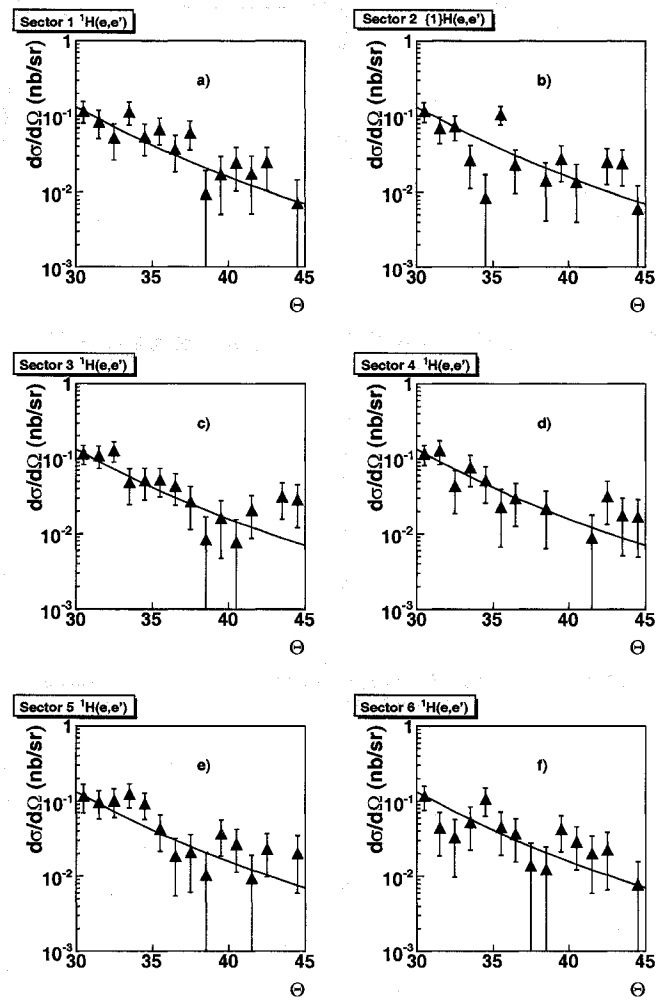
FIG. 82. Measured elastic cross section on hydrogen ^{1}H(e, e') after all corrections. The curve is the theoretical parametrization; the data is the experimental cross section.

obtaining the efficiency from simulation includes

- Generating the events in the phase space of the $^3\text{He}(e, e'pp)n$ reaction (GEN)

- Using GSIM to pass the generated events through the virtual CLAS detector

- Using GPP to include efficiencies and missing detector channels (as dead paddle in SC). GPP smears the data, includes efficiencies for the wires in DC, and removes the dead SC paddles.

- Using the RECSIS reconstruction software to reconstruct the tracks and identify the particles.

Figure 83 shows the simulated and experimental resolutions. The results for simulated events show very good agreement for the resolution of the neutron mass and the speed of the protons (the peaks for the missing mass (MM) for the data are located at 0.9395 GeV/c^2 with $\sigma = 0.03$, for GSIM events MM=0.94 GeV/c^2 with $\sigma = 0.028$).

As a next step, the low momenta protons (250–430 MeV/c) were divided into 9 momentum bins (20 MeV/c each) and 35 angle bins from 0 to 140^0 (4^0 each). The ratio between the number of generated and reconstructed events within the fiducial region was taken as an efficiency. Figure 84–89 shows the correction factors $(1/\epsilon)$ for the low momenta protons. The same procedure was done for higher momentum protons with a momentum bin of 100 MeV/c. The experimental cross sections were corrected event by event for the proton tracking efficiency.

To test the efficiency obtained by GSIM we calculated the efficiency for the protons using the $^1\text{H}(e, e')p$ (expected proton N_{expect}) and $^1\text{H}(e, e'p)$ (detected proton N_{det}) reactions. The ratio between N_{det} and N_{expect} is the efficiency for that angle θ and momentum bin. The kinematics is very restricted therefore the efficiencies are obtained only for large momentum protons (> 1 GeV/c). Figure 90 shows the tracking efficiency for the protons obtained experimentally from hydrogen elastic scattering. Figure 91 shows the tracking efficiency obtained from GSIM for the same kinematics. There is a large discrepancy between the calculated by GSIM and measured efficiencies. The uncertainty in cross section because of the efficiency discrepancy will be entered as systematical errors.
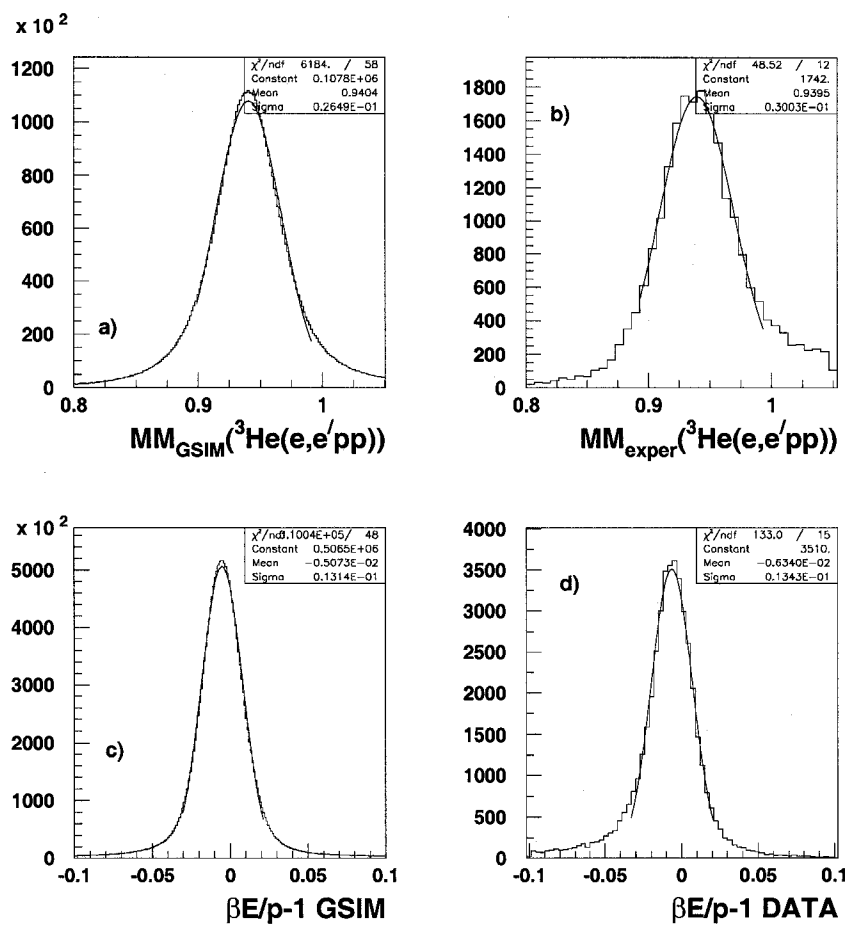
FIG. 83. Missing mass of $^3\mathrm{He}(e, e'pp)$ reaction a) simulated data, b) experimental data. Momentum resolution for the protons c) simulated data, d) experimental data.
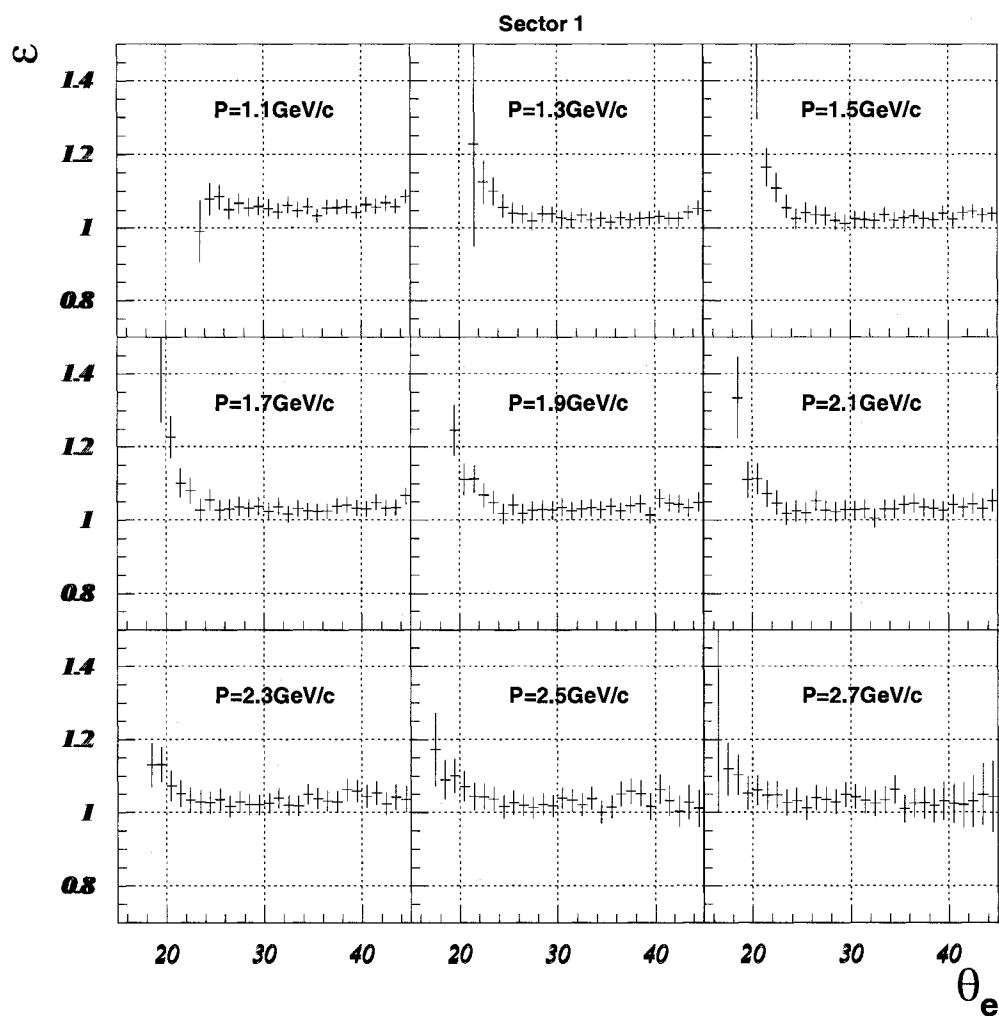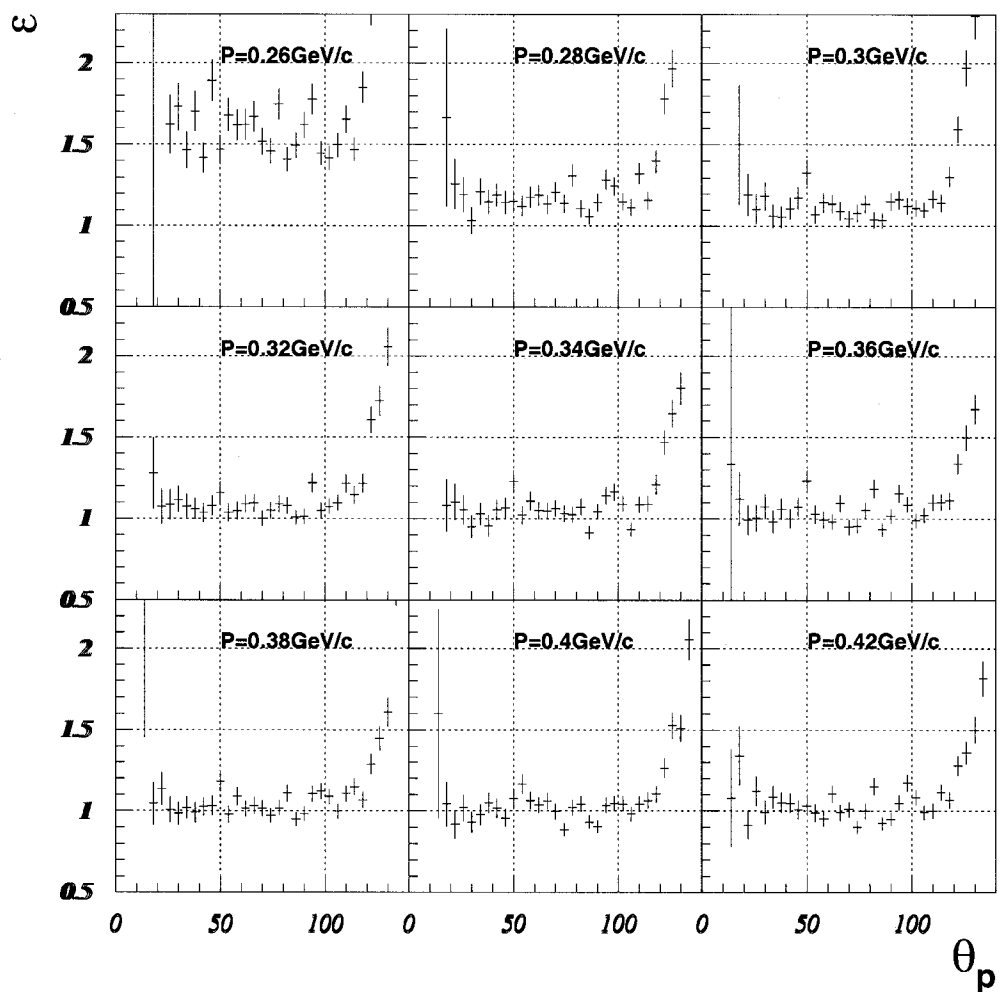
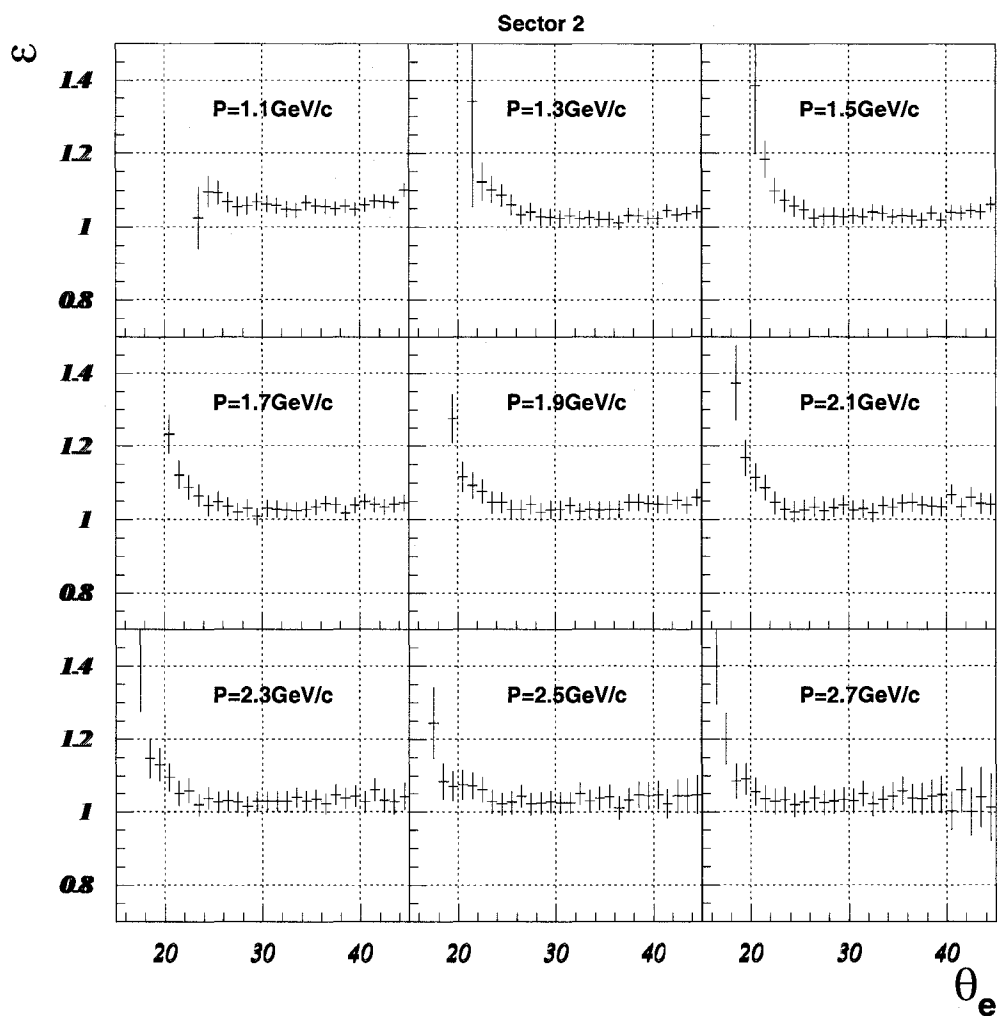FIG. 84. Sector 1 proton detection correction factors for different momentum ranges (from GSIM).
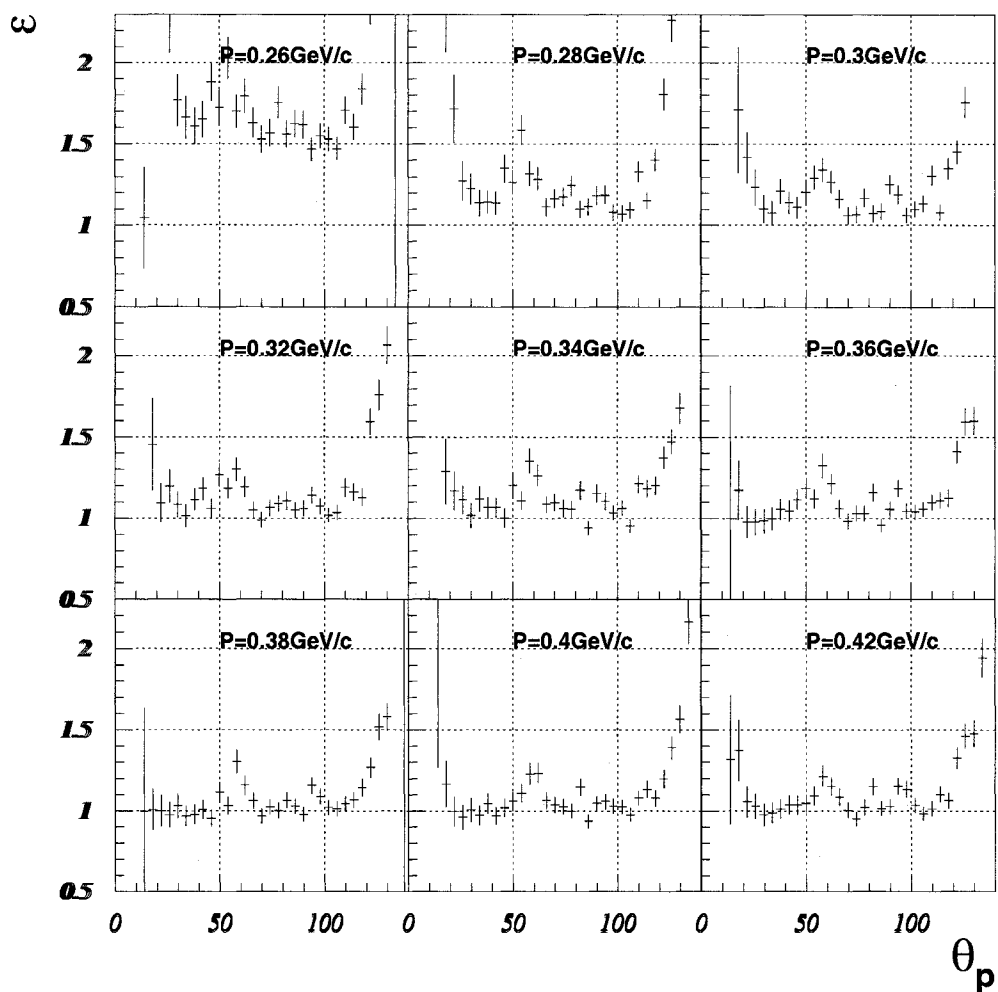
FIG. 85. Sector 2 proton detection correction factors for different momentum ranges (from GSIM).
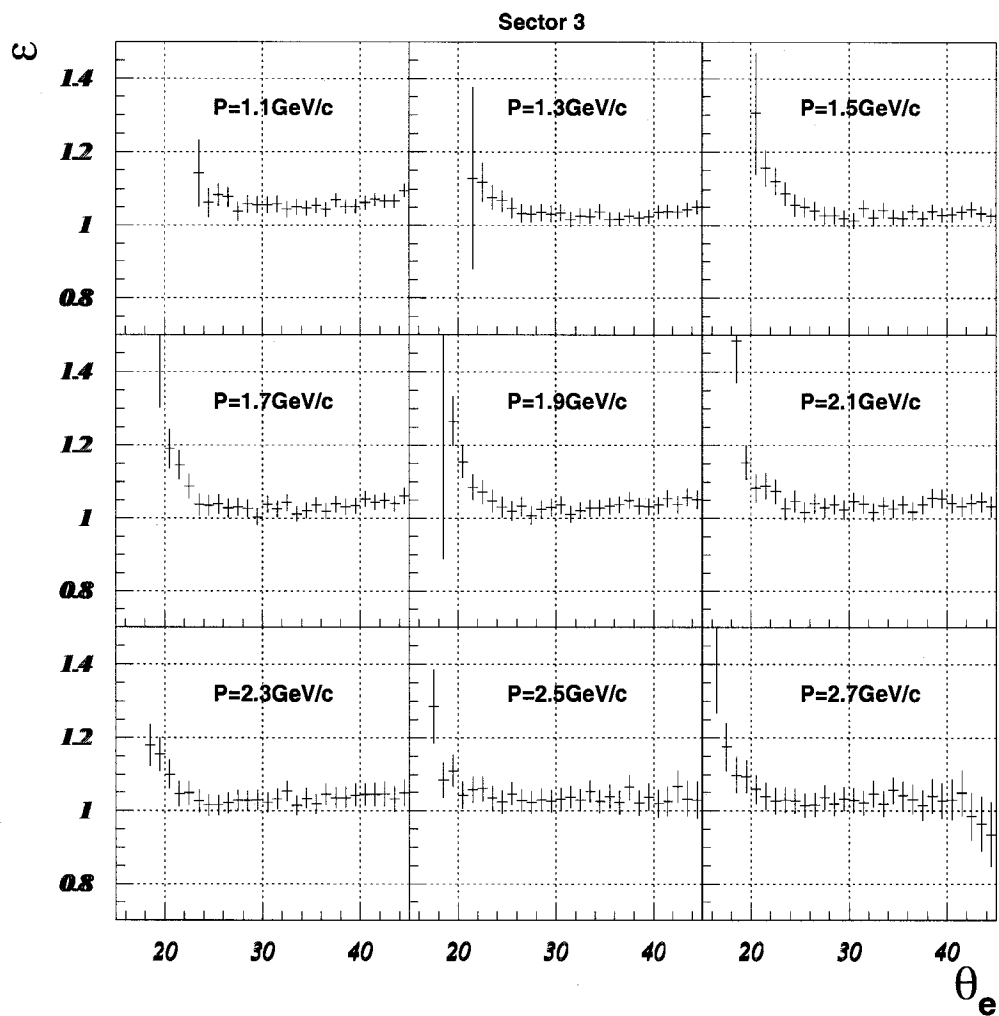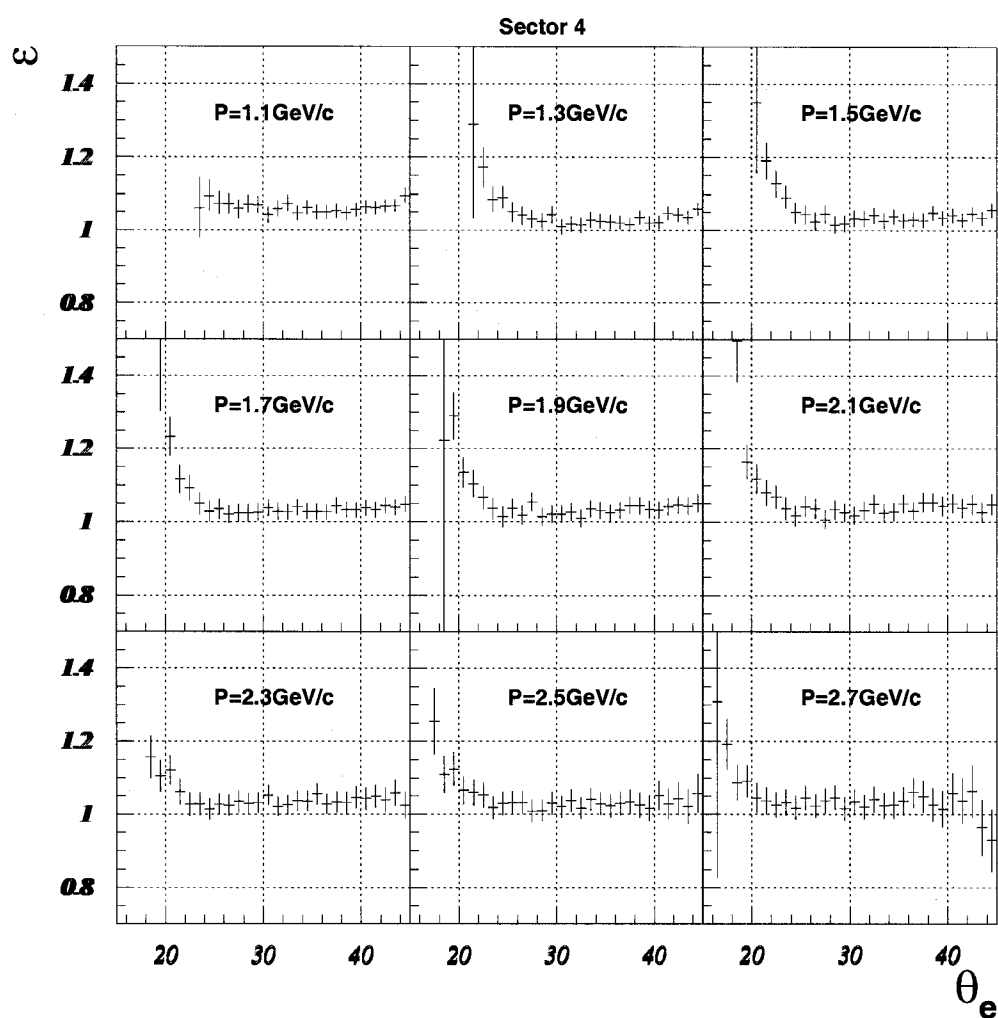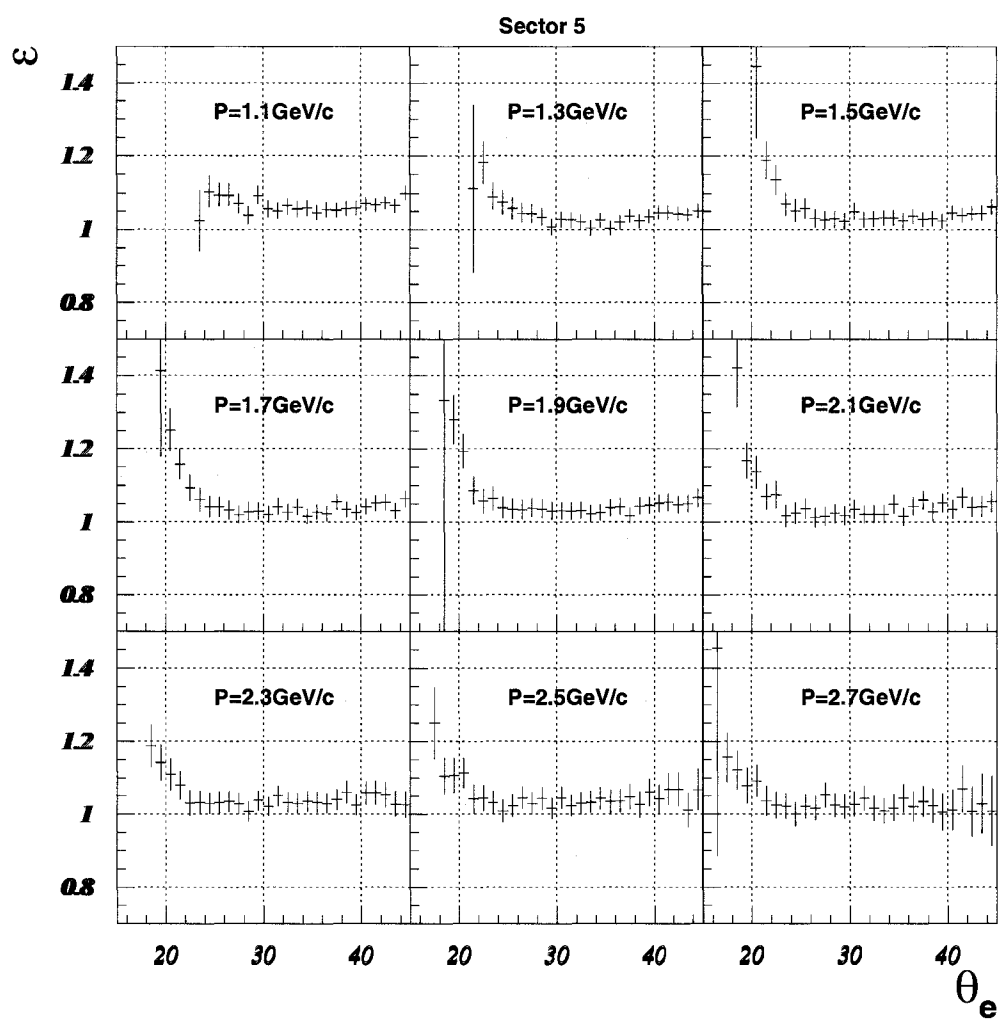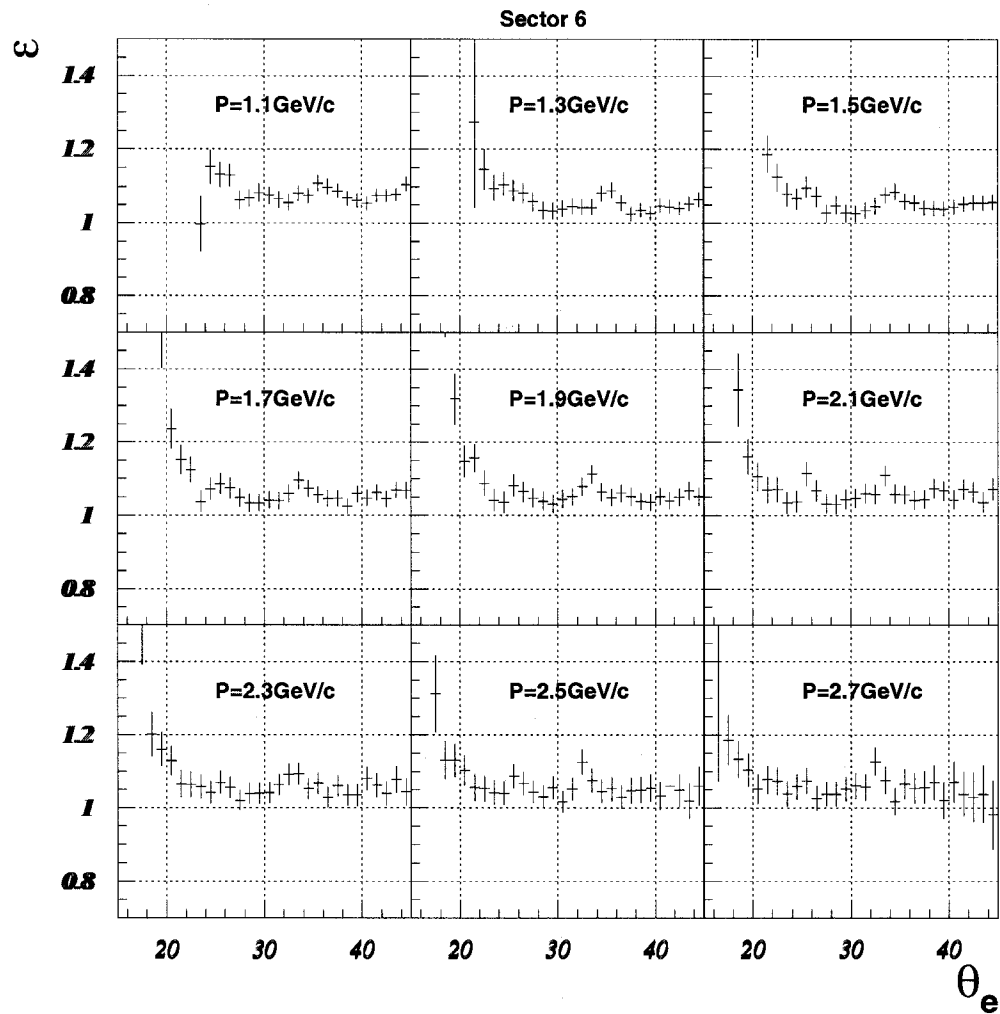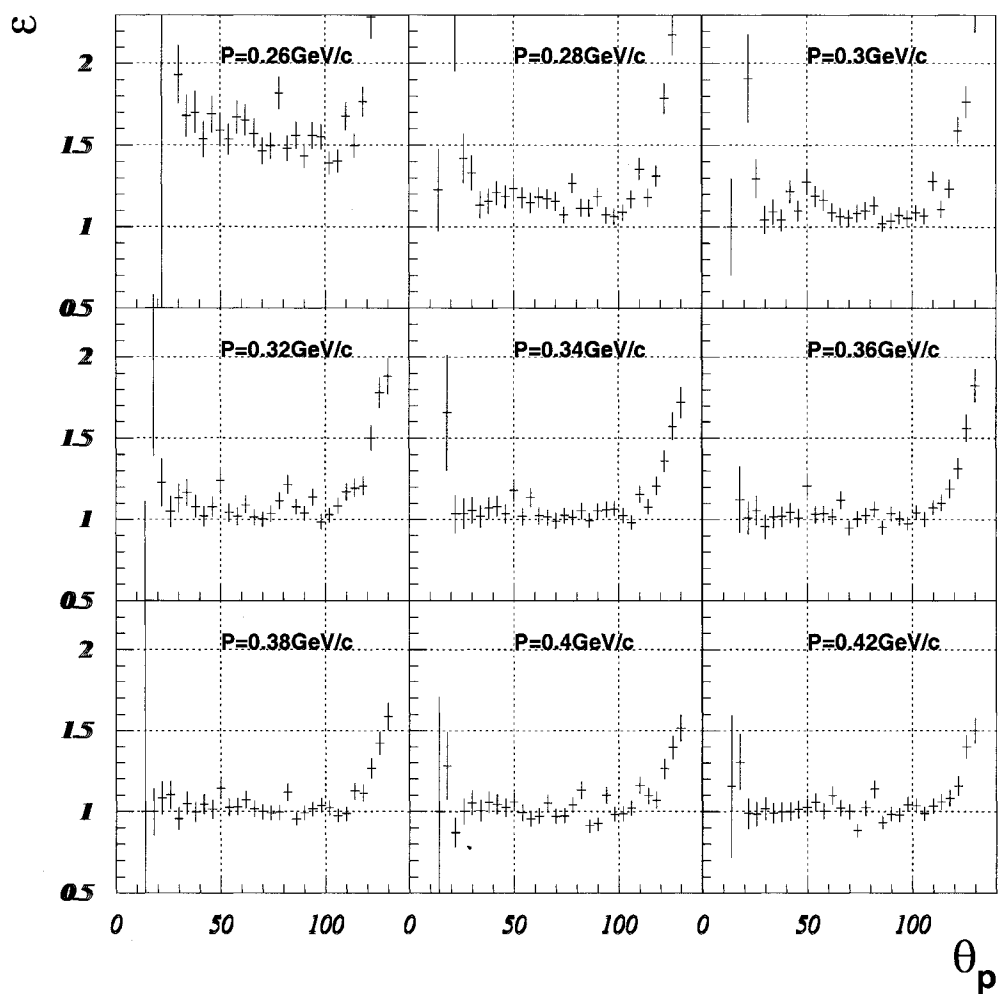
FIG. 86. Sector 3 proton detection correction factors for different momentum ranges (from GSIM).
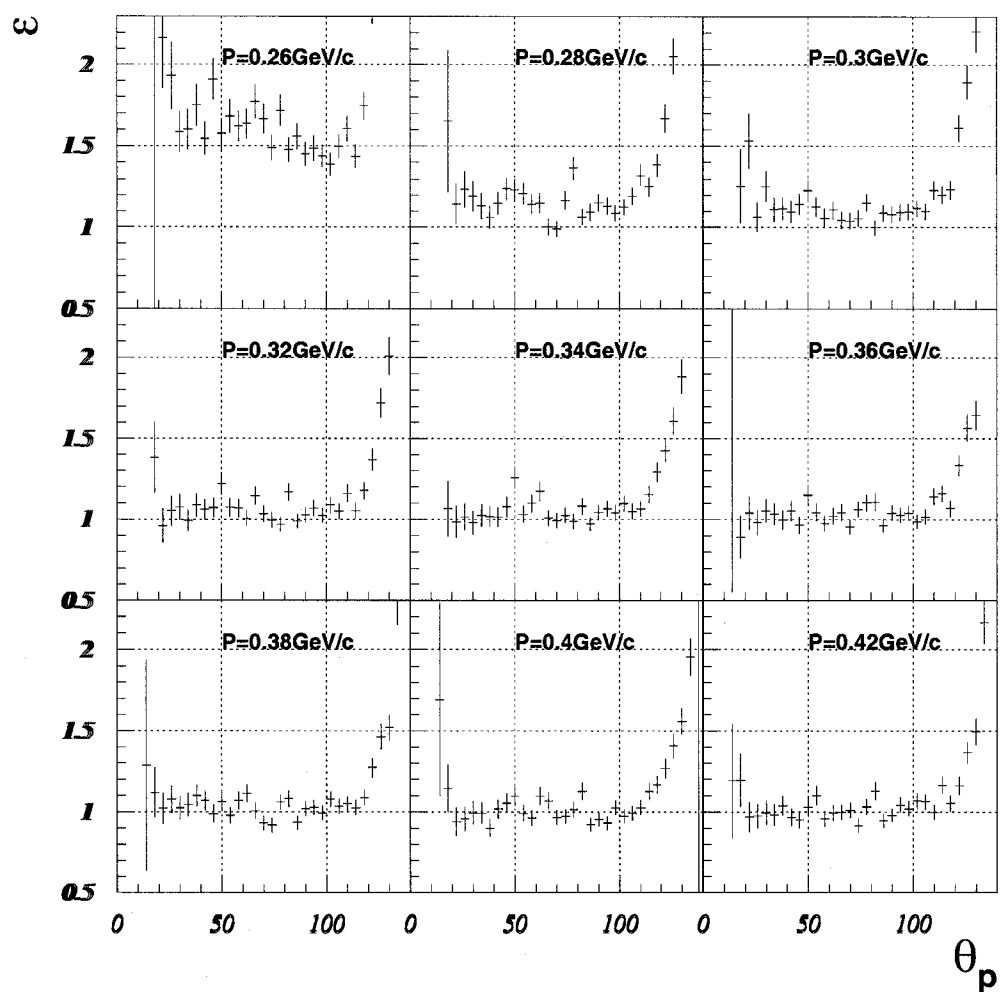
FIG. 87. Sector 4 proton detection correction factors for different momentum ranges (from GSIM).
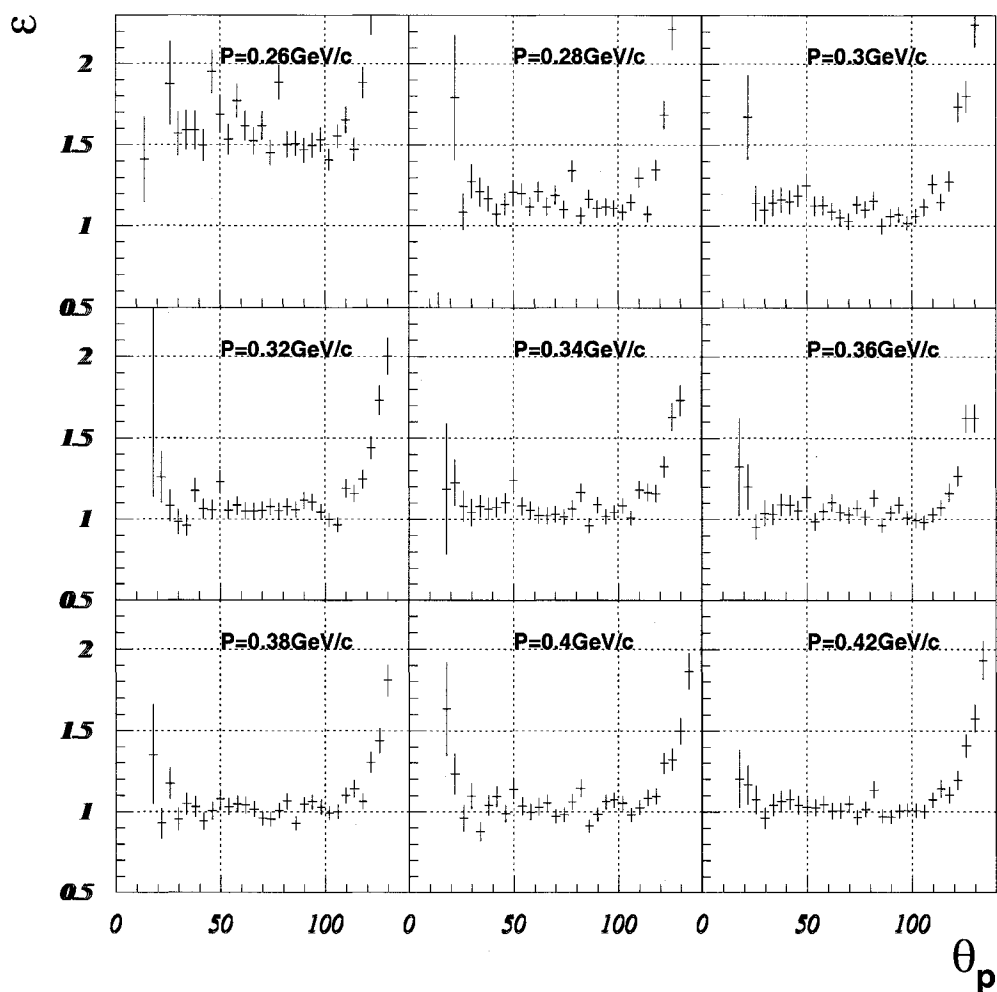
FIG. 88. Sector 5 proton detection correction factors for different momentum ranges (from GSIM).
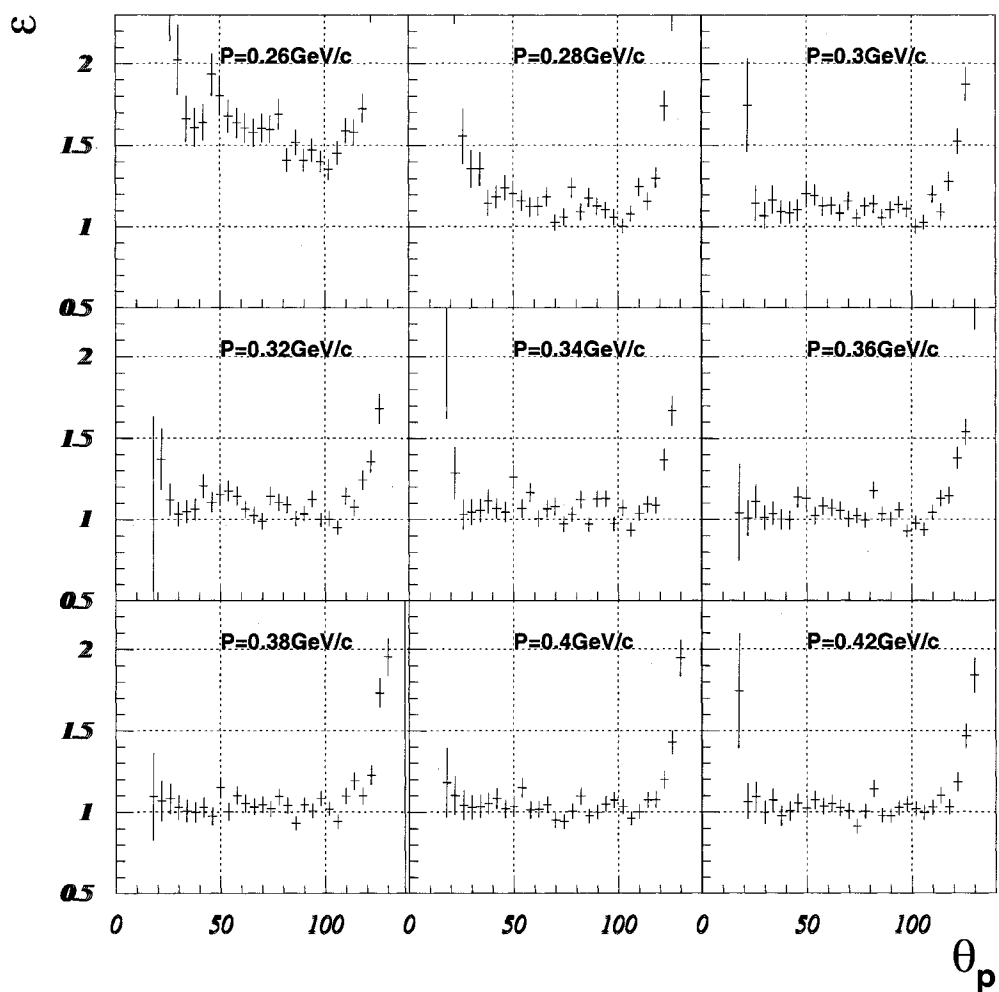
FIG. 89. Sector 6 proton detection correction factors for different momentum ranges (from GSIM).

4.5 DETECTOR MALFUNCTION CUTS

If everything is working well, then the ratio of detected electrons to incident electrons should be constant. In order to eliminate period of detector (or other) malfunction, we histogram

$$\sigma = \frac{N_e}{q \cdot \epsilon_{life} \cdot 100}$$

for 100 second intervals (see Figure 92). q is measured by the Faraday Cup, ϵ_{life} is the electronic and computer lifetime, and N_e is the number of detected electrons. We eliminated events during time intervals when $\sigma < 12$ or $\sigma > 28$.

4.6 RADIATIVE CORRECTIONS

After the cross section is extracted from the data a final correction needs to be applied: radiative unfolding. The electrons radiate photons in the presence of the nuclear electromagnetic fields which changes of the cross section. Electrons can radiate real or virtual photons either in the electromagnetic (Coulomb) field of the nucleus involved in the reaction (internal bremsstrahlung) or in the electromagnetic field of the other nuclei (external bremsstrahlung). Also the electron-target interaction followed by the ionization of the target atoms results in electron energy losses (Landau straggling).

Internal bremsstrahlung, which was first calculated by Schwinger [57] and later improved by Mo and Tsai [58] [59], has the largest overall contribution to the radiative correction. These processes are shown in Figure 93. We apply corrections to our data accounting for internal and external bremsstrahlung only, neglecting the Landau straggling corrections. The external bremsstrahlung correction to the cross section is $\approx 2\%$ and the Landau straggling correction is less than 0.001% (see Section 4.6.1).

The corrections were applied by multiplying the observed cross section by the Schwinger factor [58], [60]

$$f_{Schw} = \frac{e^{\delta(\Delta E)}}{1 + \delta'} \tag{56}$$
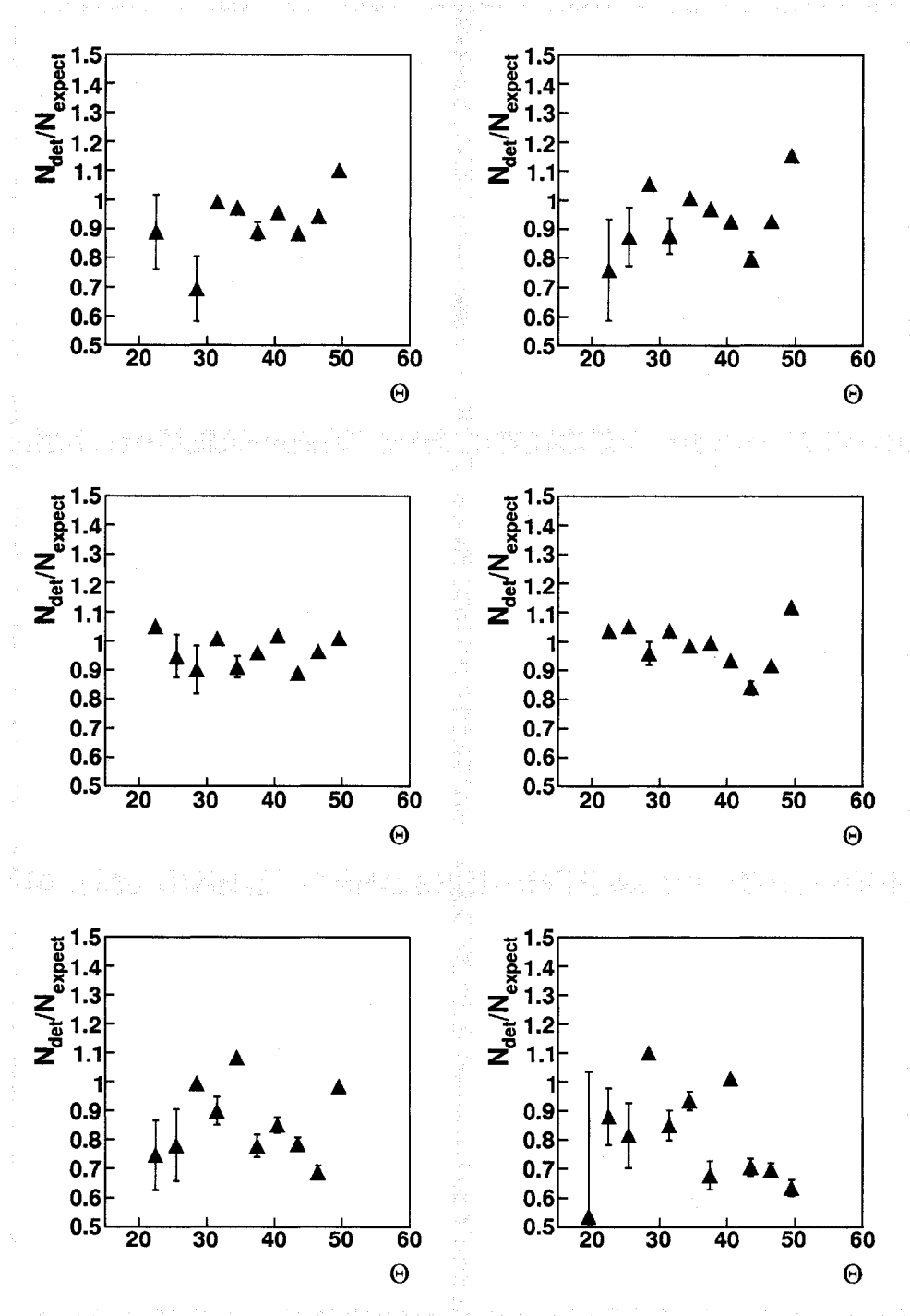
FIG. 90. Experimentally obtained proton tracking efficiency. a) Sector 1, b) Sector 2, c) Sector 3, d) Sector 4, e) Sector 5, f) Sector 6.
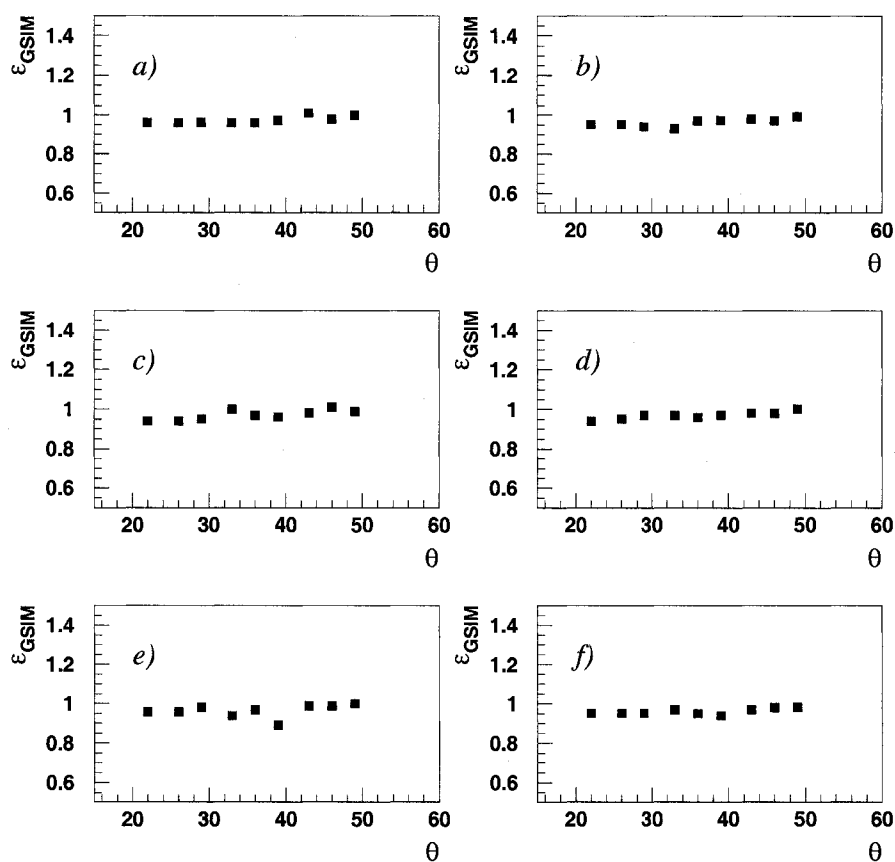
FIG. 91. Proton tracking efficiency obtained from GSIM for the kinematics corresponding to elastic scattering on hydrogen. a) Sector 1, b) Sector 2, c) Sector 3, d) Sector 4, e) Sector 5, f) Sector 6.
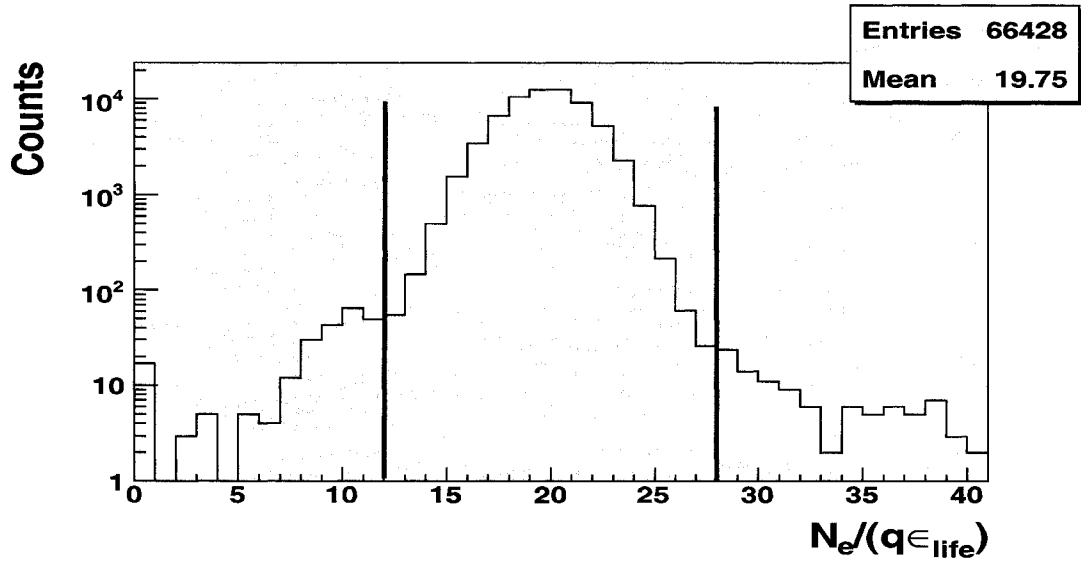
FIG. 92. Detector stability check. Ratio of detected electrons to incident electrons (corrected for computer dead time) for 100 second intervals. Unstable data (outside the red lines) was eliminated by cut.

$$\delta(\Delta E) = \frac{\alpha}{\pi} \ln\left(\frac{E_B E_f b}{\eta^2 (\Delta E)^2}\right) \left(\ln\frac{Q^2}{m_e^2} - 1\right) \tag{57}$$

with

$$b = 1 + \frac{2\omega}{M_p} \sin^2(\frac{\theta_e}{2}) \tag{58}$$

$$\eta = 1 + \frac{2E_B}{M_p} \sin^2(\frac{\theta_e}{2}) \tag{59}$$

$$\delta' = \frac{\alpha}{\pi}\left(\frac{13}{6}\left[\ln\frac{Q^2}{2} - 1\right] - \frac{17}{18} - \frac{\pi^2}{6} - \frac{1}{2}\ln^2(\frac{E_B}{E_f}) + \Phi(\cos^2\frac{\theta_e}{2})\right) \tag{60}$$

where $\Delta E = 80$ MeV is a cut off energy that was determined from half of the ^{3}He$(e, e'pp)$ missing mass width (experimental resolution), α is the fine structure constant, m_e and M_{He3} are, respectively, the electron and ^{3}He masses, E_B and E_f are the energies of incoming and outgoing electrons, and θ_e is the electron scattering angle. The Spence function $\Phi(x)$ is
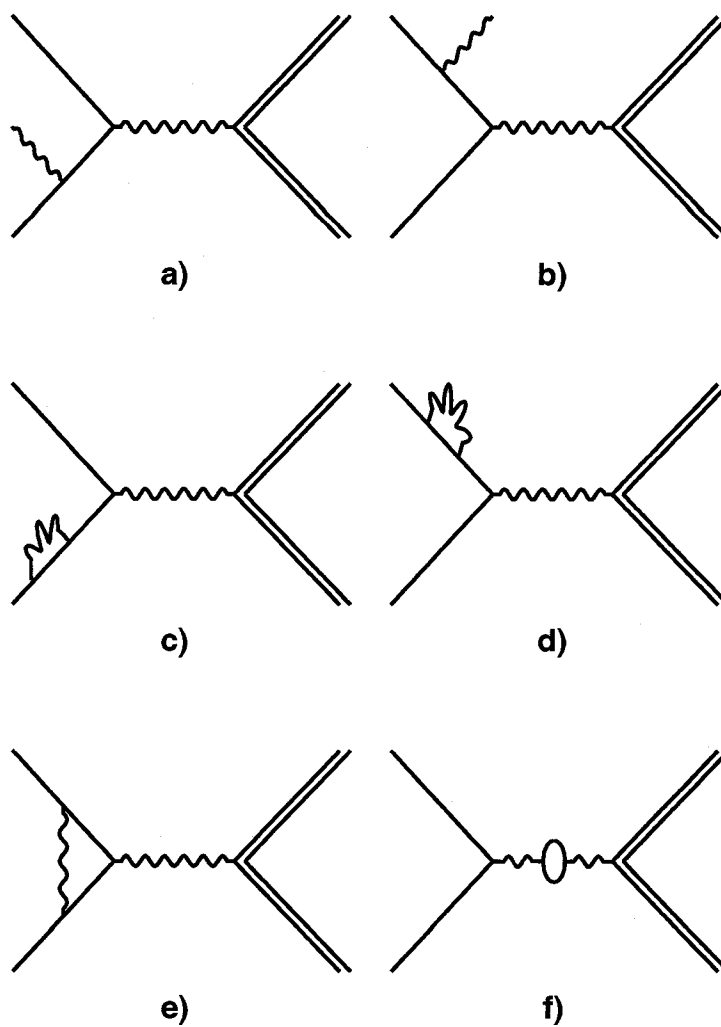
FIG. 93. Feynman diagrams for internal bremsstrahlung. a) and b) correspond to the emission of a real photon from the electron before and after the interaction, respectively. c) and d) result in renormalization of the electron mass. e) corresponds to an overall renormalization of the vertex. f) results in the renormalization of the virtual photon due to the vacuum polarization.

$$\Phi(x) = \int_0^x \frac{-\ln(1-y)}{y} dy \tag{61}$$

The correction is about 20%.

4.6.1 Other Radiative Effects

We also want to estimate the contribution from the other radiative processes: external bremsstrahlung and Landau straggling. Both processes, since they are caused by external nuclei and atoms, have an effect on the cross sections proportional to the target thickness. The correction formula for these effects are taken from [61]. The correction factor for cross section loss due to external bremsstrahlung is e^{δ_B}, where

$$\delta_B = \frac{t}{x_0 \ln 2} \ln\left(\frac{\Delta E}{E_B}\right) \tag{62}$$

where t is the target thickness, E_B is the energy of the incident electrons and x_0 is the radiation length of the target nuclei. This equation holds for $\frac{t}{x_0 \ln 2} \ll 1$. $t = 0.268$ g/cm^2 for the 4 cm long ^{3}He target.

$$x_0 = \frac{A}{4\alpha N_A Z(Z+1)r_e^2 \ln(183 Z^{-1/3})} \tag{63}$$

where Z and A are the charge and atomic number of the nuclei respectively, $N_A = 6.02 \times 10^{23}$ and the electron radius $r_e = 2.818 \times 10^{-13}$ cm. Using Eq. 63 for ^{3}He we get $x_0 = 71.95$ g/cm^2. The correction factor due to external bremsstrahlung at 4.7 GeV beam energy is 0.978.

The correction factor for cross section loss due to Landau straggling is $1 - \delta_I$, where

$$\delta_I = \frac{\lambda}{\lambda(\lambda + \ln\lambda + C)} \tag{64}$$

where $C = 0.577$ is the Euler-Mascheroni constant,

$$\lambda = \frac{\Delta E - e_0}{\xi}, \tag{65}$$

$$\xi = 0.0154 \frac{\text{MeV}}{\text{gm/cm}^2} \times t, \tag{66}$$

$$e_0 = \xi\left(\ln\frac{\xi}{e'} + 1 - C\right) \tag{67}$$

is the most probable energy loss,

$$e' = 2.718\frac{(1 - \beta^2)I^2}{2m_e},$$ (68)

and

$$I = 13.5 \times 10^{-6}Z \text{ MeV}$$ (69)

is the average ionization potential. This correction is negligible. The final average radiative correction is about $20 - 25\%$.

4.6.2 Cross Section Calculations

For kinematics bin ΔK of variable K the cross section is

$$\left(\frac{d\sigma}{dK}\right)_{data} = \frac{N_{\Delta K}}{N_e N_T \Delta K \epsilon_{EC}\epsilon_{trig}\epsilon_{track}\epsilon_{RAD}}$$ (70)

where $N_{\Delta K}$ is the number of events in the bin, N_e is the total number of electrons hitting the target, N_T is the number of target nuclei, ΔK is the bin size, ϵ_{EC} is the EC cut efficiency, ϵ_{trig} is the trigger efficiency, ϵ_{track} is the tracking efficiency for electron and proton and ϵ_{RAD} is the radiative correction. The number of electrons is calculated from the Faraday Cup measurements of the integrated beam charge $(Q_{FCup} = 4224.6 \text{ mC})$

$$N_e = \frac{Q_{FCup}}{e} = \frac{4224.6 \times 10^{-6} \text{ C}}{1.6 \times 10^{-19} \text{ C/e}} = 2.64 \times 10^{16}e$$ (71)

and the number of target nuclei is

$$N_T = \frac{N_A\rho L_T}{A} = \frac{6.02 \times 10^{23} \frac{\text{nuclei}}{\text{mol}^{-1}} \cdot 0.067 \frac{\text{gm}}{\text{cm}^3} \cdot 4 \text{ cm}}{3 \text{ mol}^{-1}} = 5.38 \times 10^{-17} \frac{\text{nuclei}}{\text{fb}}$$ (72)

The cross section is corrected for the detector and cut efficiency. The cross section is not corrected for detector acceptance. All experimental and theoretical cross sections will be presented within our detector acceptance. The fiducial cuts (detector acceptance cuts) provided as C and FORTRAN functions in Appendix A–B for use by anyone.

4.7 SYSTEMATIC ERROR EVALUATION

This section describes the systematic errors in determining the cross section. The systematic errors can come from different cuts, corrections, algorithms and calibrations. The systematic errors due to the vertex cut, EC cuts, radiative corrections, fast proton detection and electron detection are presented below.

- Systematic errors due to electron identification cuts.
  Due to EC Cuts and Event reconstruction we have uncertainty for the efficiency 1.5% and 0.5% which needed to be included into systematic errors.

- Systematic errors due to electron vertex cuts.
  The cross section was calculated for several slightly different vertex cuts (3.8,4.,4.2 cm). The uncertainty in the cross section due to the cut is less 1%.

- Systematic errors due to proton detection efficiency
  We estimated the proton detection efficiency using several methods. We used GSIM to simulate the detection efficiency (see Section 4.4.4). This resulted in large inefficiencies for very low momentum protons ($p < 350$ MeV/c) and small inefficiencies for $p > 350$ MeV/c. These results did not agree with the measured inefficiencies using $^1H(e, e'p)$ (see Section 4.4.4). Unfortunately, the efficiencies measured with $^1H(e, e'p)$ fluctuated rapidly and cover a very small part of the detection phase space.

  We used two methods to apply the measured efficiencies to the data. First we computed an average proton detection efficiency for each sector. Second we assumed that the measured efficiencies depend only on angle. Cross sections calculated with these two methods differed by 10% indicating that the systematic error due to proton detection efficiency is 10%.

- Systematic errors due to radiative corrections
  The small radiative effects like the external bremsstrahlung correction and Landau straggling were disregarded in the calculations. Therefore systematical error on the order of 2% should be taken into account.

Table VIII shows the summary of systematic errors.

TABLE VIII. Summary of systematic errors.

Uncertainty source	Uncertainty at 4.71 GeV
Electron identification	1.6%
Electron Vertex Cuts	1%
Proton detection efficiency	10%
Radiative corrections	2%
Total	11%

CHAPTER 5

PHYSICS RESULTS

Our major goal is to understand the ^{3}He$(e, e'pp)n$ reaction where two or more nucleons are active with momentum $p > p_{fermi}$. This restriction comes from the definition of a Short Range Correlation (SRC) given in Chapter 1 **the effect when one nucleon's momentum is balanced by the momentum of only one other nucleon is called an SRC**. In the Plane Wave Impulse Approximation (PWIA) a single nucleon absorbs the virtual photon and is ejected from the nucleons without further interaction. Thus, events with two or more active nucleons need to be explained by some combination of SRC, Final State Interaction (FSI), Meson Exchange Currents (MEC) and Isobar Configurations (IC). We will try to explore all kinematics of ^{3}He$(e, e'pp)n$ and determine in which kinematical regions the different effects dominate. We hope to find a region dominated by SRC (ie: where FSI and MEC/IC are small) and characterize SRC.

The virtual photon kinematical range is shown in Figure 94. The line on Figure 104 represents quasi-elastic kinematics or $x_B = 1$. The events are spread over a wide kinematic range, from $Q^2 = 1$ to 2.5 GeV^2, centered at $< Q^2 >= 1.5$ GeV^2. The events also peak at $x_B \approx 1$.

5.1 SEARCH FOR SRC

In order to better understand the three nucleon break up of ^{3}He, we use a Dalitz plot to show the energy distribution among the nucleons. Figure 95 shows the kinetic energy of the first proton divided by the energy transfer, T_1/ω, versus that of the second proton[1]. Events in the three corners of the resulting triangle correspond to reactions where one nucleon has almost all of the kinetic energy. Events along the edges correspond to the reaction where two nucleons share the energy. Events in the middle correspond to the reaction where all three nucleons share the energy of the virtual photon. We also need to mention a few interesting features of the plot:

---

[1]Remember that the minimum detected proton momentum is 250 MeV/c and there is no minimum neutron momentum.
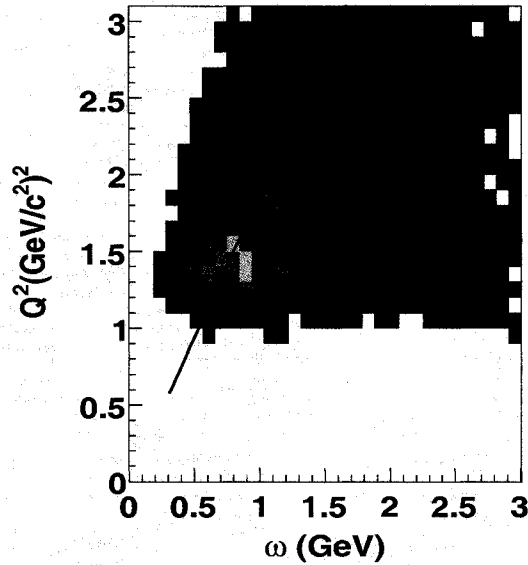
FIG. 94. Q^2 vs ω for $^3\text{He}(e, e'pp)n$ events for 4.71 GeV/c beam energy. The line shows the quasi-elastic condition $\omega = Q^2/2m_p$ or $x_B = 1$

- There is a small peak which corresponds to a leading neutron (the neutron carries most of the energy of the virtual photon) when T_1/ω and T_2/ω are less than 0.2.

- There are large peaks at the corners corresponding to a leading proton. These peaks are more pronounced than the peak in region 1 because of the restriction on proton momentum detection (there is no restriction on neutron momentum).

- There is a ridge stretching from upper left to lower right corresponding to two fast protons and a low momentum neutron.

Figure 95 b) and c) shows Dalitz plots of the kinetic energies of the two protons divided by the virtual photon energy with the requirement that the neutron momentum $p_n < 200$ MeV/c for experiment and calculation respectively. In both cases we observe peaks on the edges.
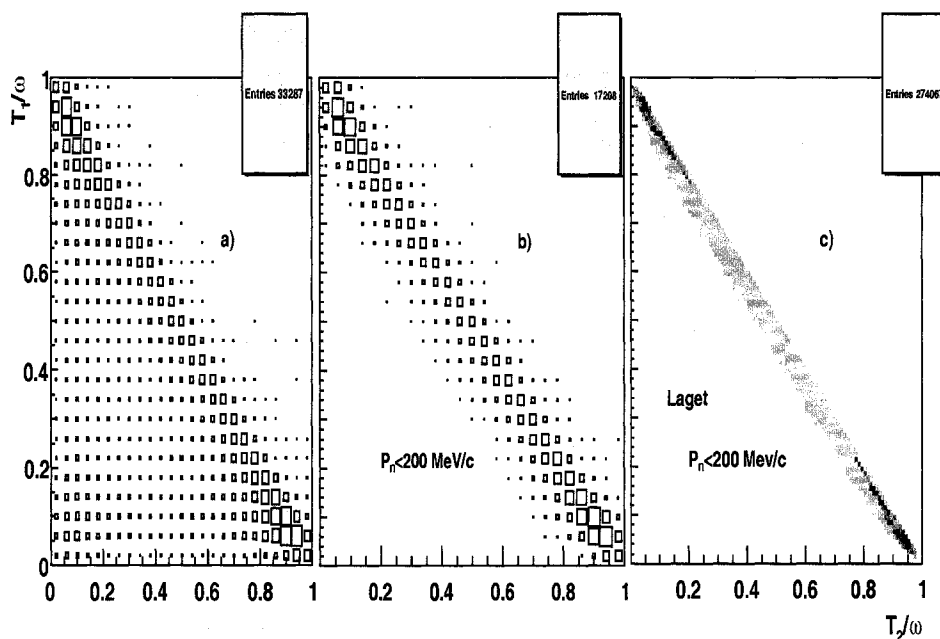
FIG. 95. Dalitz plot of the lab frame kinetic energy of proton 1 divided by the energy transfer plotted versus the same for proton 2. a) data without cuts, b) data cut on neutron momentum $p_n < 200$ MeV/c, c) Full calculations provided by Laget with cut on neutron momentum $p_n < 200$ MeV/c

If two of the nucleons in ^{3}He are in an SRC, then the virtual photon can probe the SRC in one of two ways:

1. it can be absorbed on one nucleon of the pair. The other nucleon recoils and we observe two active nucleons.

2. it can be absorbed on the third nucleon. The spectator correlated pair flies apart and we observe three active nucleons.

In both cases the struck particle carries almost all the energy of virtual photon. These reactions are contaminated with:

1. Rescattering. The leading particle rescatters with one of the nucleons and in the final state we have two active nucleons or double rescattering occurs and finally we have three active nucleons (see Figures 10–11).
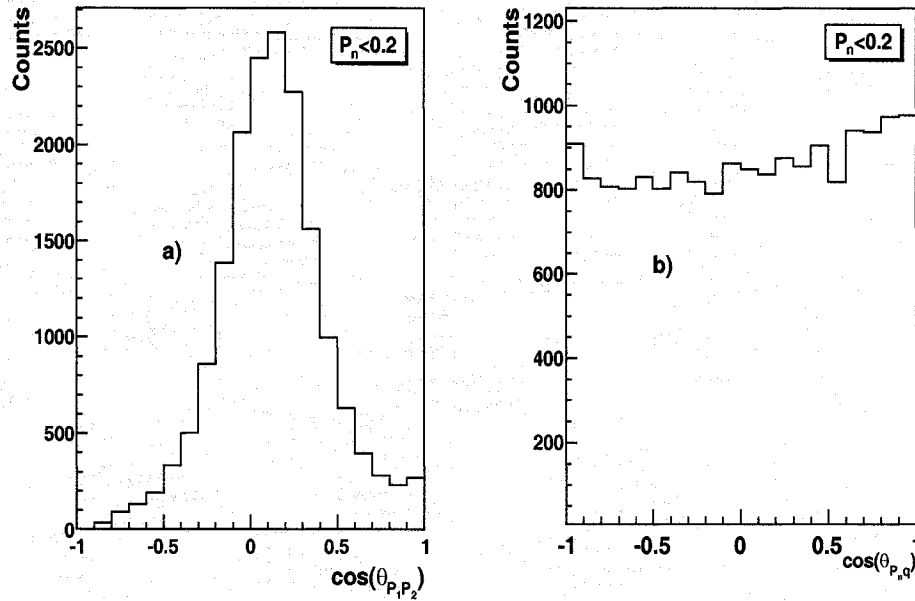
FIG. 96. The angular distributions for $p_n < 200$ MeV/c a) $\theta_{p_1 p_2}$ angle between the two protons and b) $\theta_{p_n q}$ angle between the neutron and the virtual photon .

2. MEC and IC. The leading particle emits a meson which is absorbed by one or two nucleons (see Figure 8).

In next two sections we will investigate the effect of SRC in the two ways described above. The first method will be applied only to proton-proton SRC as all the protons have detection limitations on momentum (250 MeV/c) but the neutron can have any momentum. For the second method we will take all three particles to be active ($p_N > 250$ MeV/c).

5.2 EVENTS WITH TWO ACTIVE NUCLEONS

In this section we consider events where the two protons are active and the neutron is not (see Figure 95 b)). The momentum of the neutron is chosen to be less than 200 MeV/c as the Fermi momentum of the nucleon inside the ^{3}He is around 150 MeV/c. Figure 96 b) shows the opening angle between the neutron and the virtual photon, $\theta_{p_n q}$. The distribution of $\theta_{p_n q}$ is flat, indicating that the neutron is a
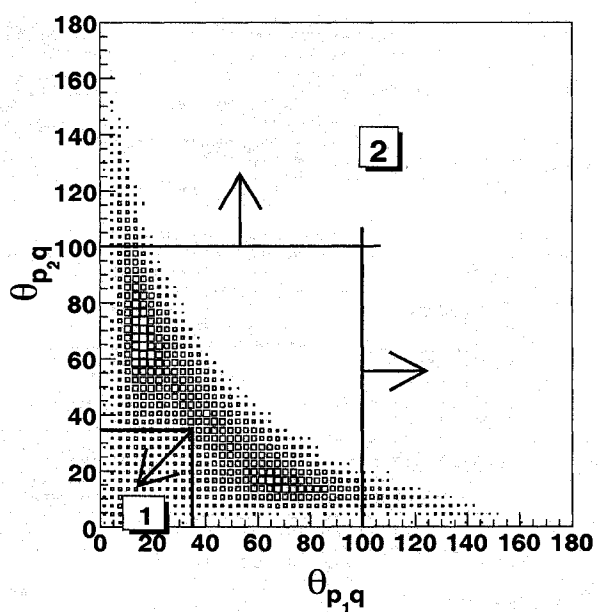
FIG. 97. Angles of the protons relative to the virtual photon for momentum $p_n < 200$ MeV/c. Region 1 is forward kinematics and region 2 is backward kinematics.
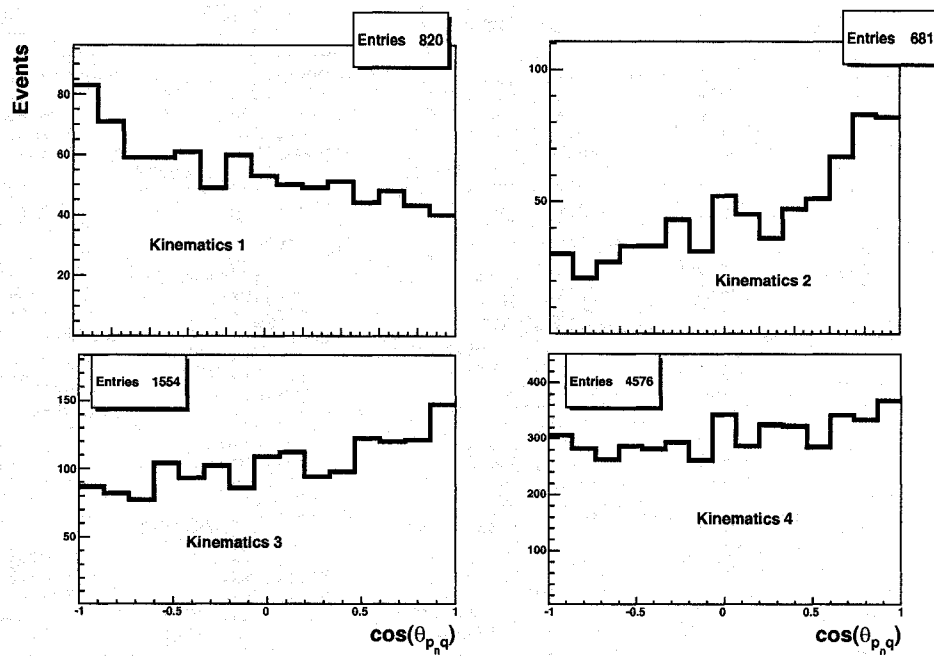
FIG. 98. Neutron angle relative to the virtual photon for $p_n < 200$ MeV/c. a) forward kinematics $\theta_{p_1 q} < 35°$ and $\theta_{p_2 q} < 35°$, b) backward kinematics $\theta_{p_{slow} q} > 100°$, c) kinematics $0.25 < p_{slow} < 0.35$ GeV/c, d) kinematics $0.4 < p_{slow} < 0.6$ GeV/c.
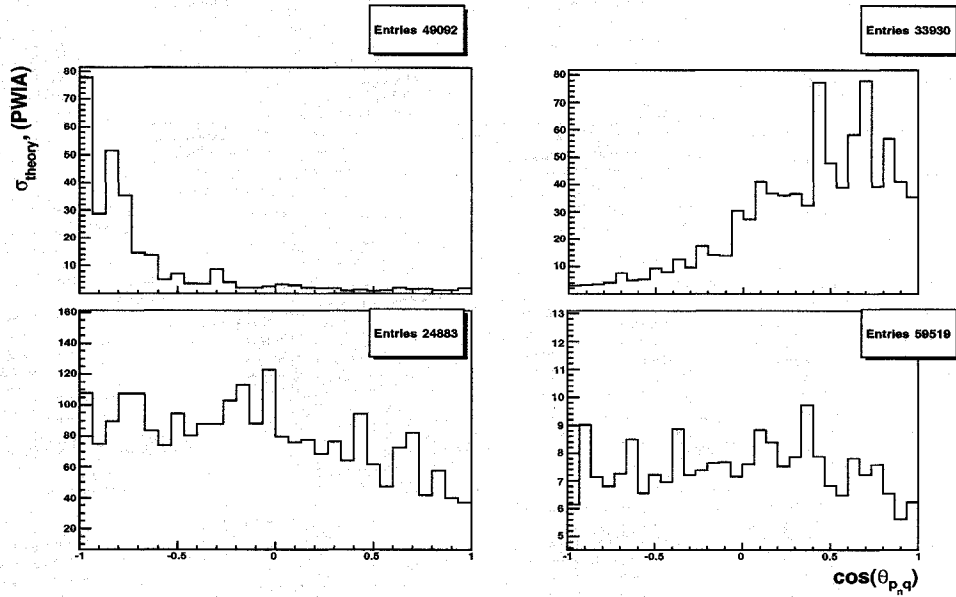
FIG. 99. Calculated (PWIA) angle of the neutron relative to the virtual photon for $p_n < 0.2$ GeV/c by Laget. a) forward kinematics $\theta_{p_1 q} < 35°$ and $\theta_{p_2 q} < 35°$, b) backward kinematics $\theta_{p_{slow} q} > 100°$, c) kinematics $0.25 < p_{slow} < 0.35$ GeV/c, d) kinematics $0.4 < p_{slow} < 0.6$ GeV/c.
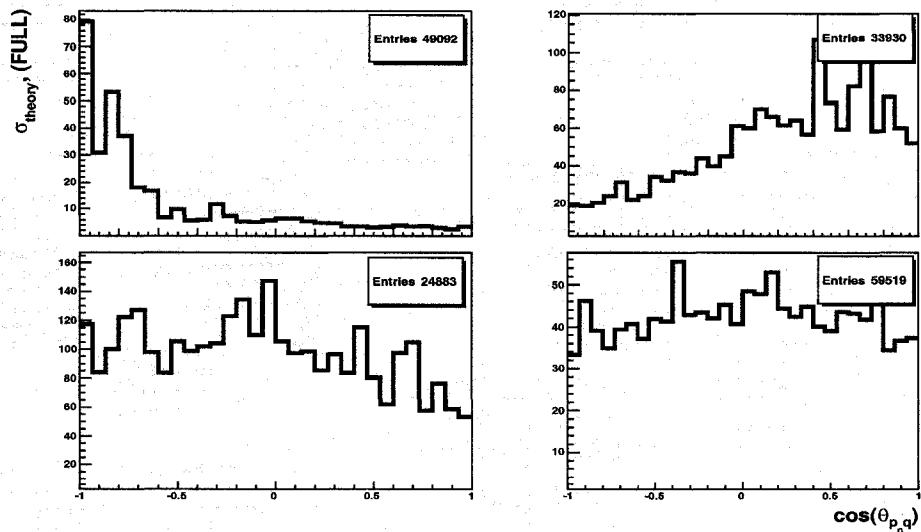
FIG. 100. Calculation (FULL) of the neutron angle relative to the virtual photon for $p_n < 200$ MeV/c by Laget. a) forward kinematics $\theta_{p_1 q} < 35°$ and $\theta_{p_2 q} < 35°$, b) backward kinematics $\theta_{p_{slow} q} > 100°$, c) kinematics $0.25 < p_{slow} < 0.35$ GeV/c, d) kinematics $0.4 < p_{slow} < 0.6$ GeV/c.

spectator. Figure 96 a) shows the angular distribution of the opening angle between the two protons, $\theta_{p_1 p_2}$. Note that it peaks sharply at a little less than 90°. A peak at 90° is the classical signature of rescattering. Thus it will be a challenge to find regions where rescattering effects do not dominate.

Figure 97 shows the distribution of the angles of the two protons (relative to the direction of the virtual photon). Several features of this plot should be stressed here:

- the enhancement around $\theta_{p_1 q} + \theta_{p_2 q} = 90°$. This is the region where FSI dominates.

- the tails at $\theta_{p_1 q}$ or $\theta_{p_2 q} > 100°$ (region 2) "Backward kinematics".

- the low probability region where $\theta_{p_1 q}$ or $\theta_{p_2 q} < 35°$ "Forward kinematics".

As we are trying to investigate possible NN correlations between the two protons, the only regions of the interest can be regions 1 and 2. Here the two protons each have momentum larger than the typical momentum in ^{3}He so one of the condition of SRC is satisfied.

In the forward kinematics (Region 1),

$$\theta_{p_1 q} < 35° \quad \text{and} \quad \theta_{p_2 q} < 35° \tag{73}$$

both protons are moving forward. One way to produce this is if there is a short range correlated pair with one proton moving forward and the other backwards. If the backward proton absorbs the virtual photon, then both protons will go forward in the final state. This kinematics corresponds to the $x_B > 1$ kinematics when the correlated proton initially in the nucleus has momentum opposite to the virtual photon direction. After scattering, both protons travel forward along the direction of the virtual photon. Figure 98 (a) shows that in this case the neutron–virtual photon angle peaks at backward angles, indicating that the neutron might not be a simple spectator. Figures 99 and 100 show the calculated neutron angles. The calculations are more strongly backward peaked in the forward kinematics even for FULL calculations. The distributions on Figures 99 and 100 have the same features but different cross section magnitude because of the effects of FSI and MEC.

The "backward kinematics" (suggested by [62]) occurs when the opening angle between one of the protons and the virtual photon is greater than 100° (Figure 97

region 2)

$$\theta_{p_{slow}q} > 100°. \tag{74}$$

Since it is difficult for photon absorption, FSI or MEC to produce a backward going proton, this is a favorable kinematics to look for SRC effects. In this kinematics the struck proton has its initial momentum directed along the virtual photon direction and therefore corresponds to $x_B < 1$. Figure 98 (b) shows the neutron angle is peaked in the direction of the virtual photon. This is qualitatively reproduced by the calculations. We will later compare with calculation to see if these regions are SRC dominated.

As the main interest of our studies is the effect of SRC, we need to be able to correctly estimate the contribution of different processes like FSI and MEC. Final state interactions will play a very big role when the momenta of the two protons are comparable. When the momentum of the slow proton is much smaller than the momentum of the struck proton, the effect of SRC should be smaller. That is why we are interested in the angle between the slow proton and the virtual photon for two momenta of the slower proton

$$0.25 < p_{slow} < 0.35 \text{ GeV/c} \tag{75}$$

and

$$0.4 < p_{slow} < 0.6 \text{ GeV/c} \tag{76}$$

We expect that for $0.25 < p_{slow} < 0.35$ GeV/c the protons are almost spectators and should therefore be isotropic in $\theta_{p_{slow}q}$ and the effect of FSI should be small. For $0.4 < p_{slow} < 0.6$ GeV/c, the protons are unlikely to be spectators. The angular distribution should be peaked at around 90° in $\theta_{p_1p_2}$ or about 70° in $\theta_{p_{slow}q}$. Figure 98 (c) and (d) show that the neutron angle distribution is almost flat. This indicates that the neutron is mostly a spectator in these kinematics.

Figure 101 shows the virtual photon distribution of each domain of interest. Note that the forward kinematics is concentrated at lower energy transfer ($x_B > 1$) and the backward kinematics is concentrated at higher energy transfer ($x_B = \frac{Q^2}{2m\omega} < 1$). The other two kinematics are peaked at $x_B = 1$, indicating that they are dominated by quasi-elastic knockout, perhaps followed by rescattering.
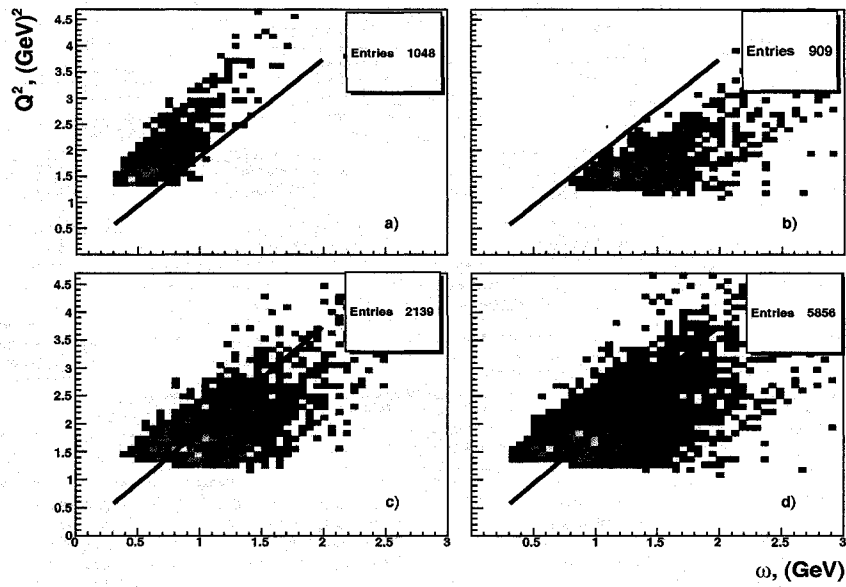
FIG. 101. Q^2 vs ω for $^3\mathrm{He}(e, e'pp)n$ events with $p_n < 200$ MeV/c. a) forward kinematics $\theta_{p_1 q} < 35°$ and $\theta_{p_2 q} < 35°$, b) backward kinematics $\theta_{p_{slow} q} > 100°$, c) kinematics $0.25 < p_{slow} < 0.35$ GeV/c, d) kinematics $0.4 < p_{slow} < 0.6$ GeV/c. The lines are drawn at $x_B = \frac{Q^2}{2m\omega} = 1$.

Figure 102 shows the cross-sections for the four kinematic regions presented in Eqs.[73,74,75,76]. One interesting observable is the (model dependent) relative momentum of the pair before the collision defined as

$$\vec{p}_{rel} = (\vec{p}_{fast} - \vec{q} - \vec{p}_{slow})/2$$

(assumes PWIA). The points and histogram present the cross section with and without radiative corrections respectively. If the "backward" and "forward" kinematics are both dominated by SRC, then the momentum distributions p_{rel} should have the same behavior for Figure 102 a) and b). The difference indicates the large contribution from other processes. In Figure 102 c) and d) the angular distributions are peaked at 80° and 70°, indicating the dominance of FSI, specially for $0.4 < p_{slow} < 0.6$ GeV/c.

Figure 103 shows the same pictures with all corrections and theoretical calculations. The black points present the experimental results, magenta and red points are the calculations provided by Laget, integrated by Monte Carlo over the experimental acceptance. The red squares show Plane Wave Impulse Approximation calculations (PWIA) and magenta inverted triangles show the PWIA+FSI+ two and three body Meson Exchange Currents (MEC2)and (MEC3) calculations.

5.2.1 Events with two active nucleons, discussion and summary

When we select ^{3}He$(e, e'pp)n$ events with a slow neutron, $p_n < 200$ MeV/c, the reaction is dominated by FSI (see Figure 96 (a)). The neutron angular distribution is isotropic indicating that it is a spectator to the reaction The proton–proton opening angle is sharply peaked at 90°, indicating that the events are dominated by virtual photon absorption on one proton followed by proton–proton rescattering.

To see if we understand the rescattering, we selected events with proton momenta $< p >= 0.3$ GeV/c where we expect little FSI and $< p >= 0.5$ GeV/c where we expect FSI to dominate. In both these cases, the neutron angular distribution is isotropic and Laget's calculations reasonably reproduce the data.

At $< p >= 0.3$ GeV/c, the measured slower proton angular distribution is several times smaller than the calculation. However, as expected, the calculation shows almost no effect from FSI or MEC.
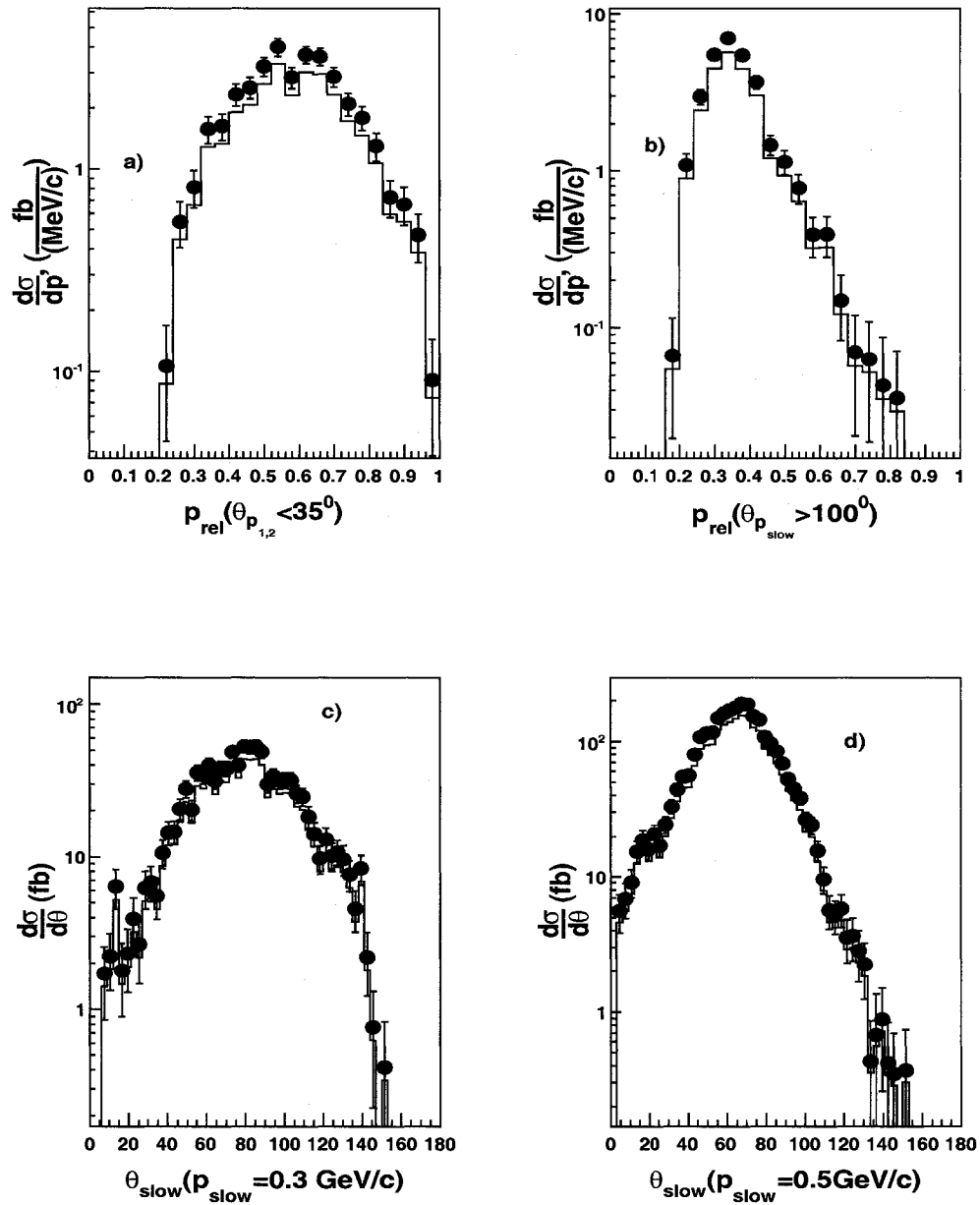
FIG. 102. Cross section with (points) and without (histogram) radiative corrections in slow neutron kinematics with all corrections: a) vs relative momentum of proton-proton pair $\vec{p}_{rel} = (\vec{p}_{fast} - \vec{q} - \vec{p}_{slow})/2$ in forward kinematics $\theta_{p_1q} < 35°$ and $\theta_{p_2q} < 35°$, b) vs relative momentum of proton-proton pair in backward kinematics $\theta_{p_{slow}q} > 100°$, c)vs slow proton-virtual photon angle θ_{slow} for $0.25 < p_{slow} < 0.35$ GeV/c, d) vs θ_{slow} for $0.4 < p_{slow} < 0.6$ GeV/c.
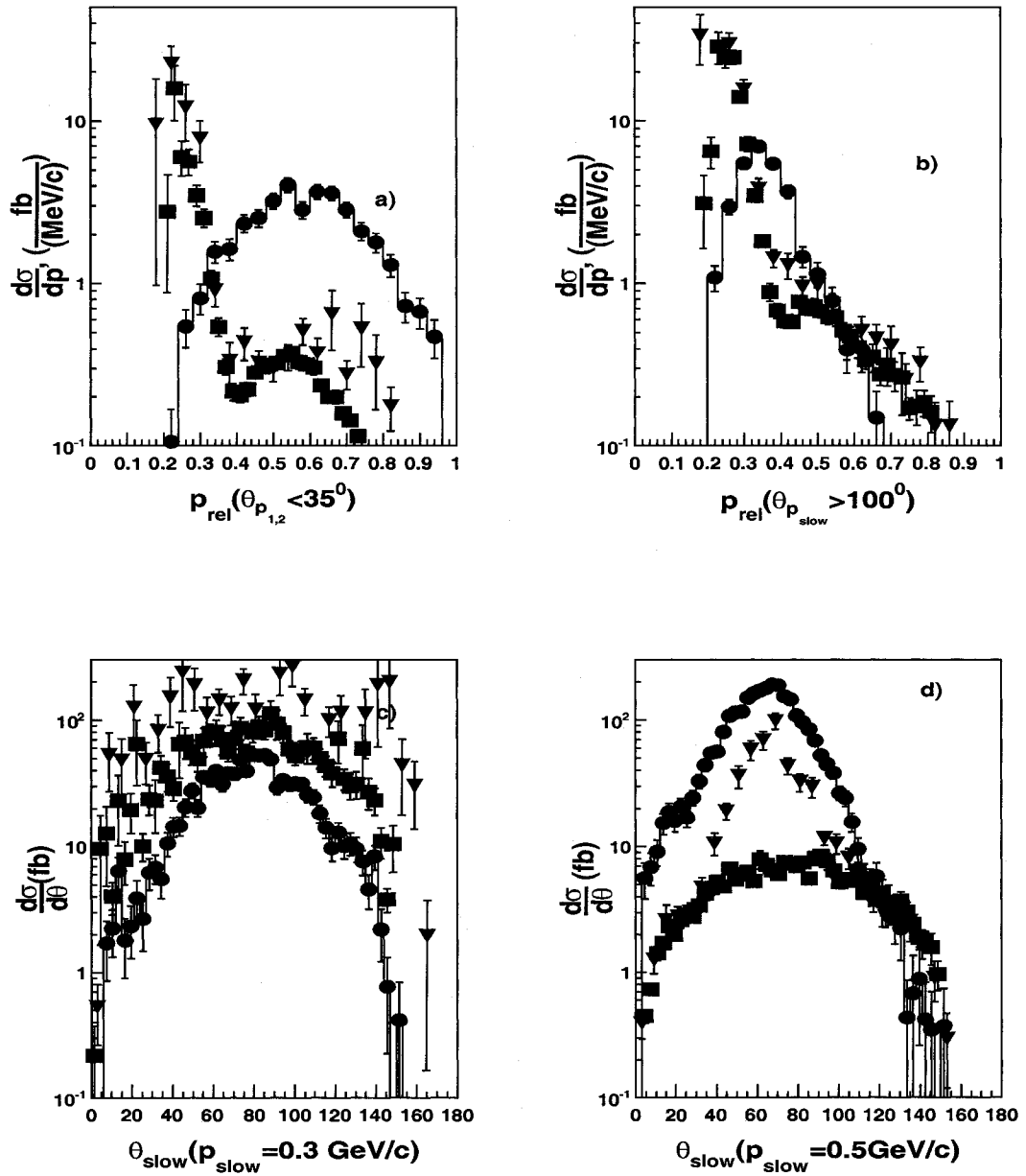
FIG. 103. Cross section in slow neutron kinematics with all corrections: a) vs relative momentum of the proton-proton pair $\vec{p}_{rel} = (\vec{p}_{fast} - \vec{q} - \vec{p}_{slow})/2$ in forward kinematics $\theta_{p_1q} < 35°$ and $\theta_{p_2q} < 35°$, b) vs p_{rel} in backward kinematics $\theta_{p_{slow}q} > 100°$, c) vs slow proton-virtual photon angle θ_{slow} for $0.25 < p_{slow} < 0.35$ GeV/c, d) vs θ_{slow} for $0.4 < p_{slow} < 0.6$ GeV/c. Black circles–data, red squares–PWIA, magenta inverted triangles–PWIA+FSI+MEC)

At $<p>=0.5$ GeV/c, the measured and calculated slower proton angular distribution are both the peaked at 70°, although the calculation underestimates the data for the small angles. The peak in the calculation is due to entirely to rescattering (FSI) as expected. We also observe good qualitative and quantitative agreement for the larger angles.

Thus, we have at least a qualitative understanding of the reaction mechanism when we have only two active nucleons.

We then looked at forward proton kinematics, $\theta_{p_1 q} < 35°$ and $\theta_{p_2 q} < 35°$, and at backward kinematics $\theta_{pq} > 100°$. In the absence of FSI and MEC, the relative momentum distributions should have the same shape. Clearly, they do not. The forward kinematics has p_{rel} broadly peaked at 300 MeV/c. MEC are much less important.

For the forward kinematics, the calculation disagrees with both the neutron angular distribution and the proton p_{rel} distribution.

For the backward kinematics, the calculation describes the neutron forward peaking and describes the slope of the p_{rel} distribution for larger relative momentum. We observe differences between calculation and data for $400 < p_{rel} < 600$ MeV/c.

The main conclusion is that the two active nucleon kinematics is dominated by FSI. The calculation shows that the best region to investigate SRC is backward kinematics where the contribution of FSI is small.

5.3 THREE ACTIVE NUCLEONS

Now that we have examined kinematics with two active nucleons, we will next examine kinematics where all three nucleons are active. In this kinematics all final particles have momentum larger than 250 MeV/c. Figure 104 shows the electron kinematical coverage with the cut on particles momentum $p_N > 250$ MeV/c. The line on Figure 104 represents quasi-elastic kinematics or $x_B = 1$. The events are spread over a wide kinematics region, mostly between $Q^2 = 1$ and 2.5 GeV^2 and peaked at $Q^2 \approx 1.5$ GeV^2.

In order to picture the energy distribution of the three nucleons, we constructed a Dalitz plot of the kinetic energy of the two detected protons. Figure 105 shows the kinetic energy of the two protons divided by the energy transfer (T_{prot}/ω) plotted
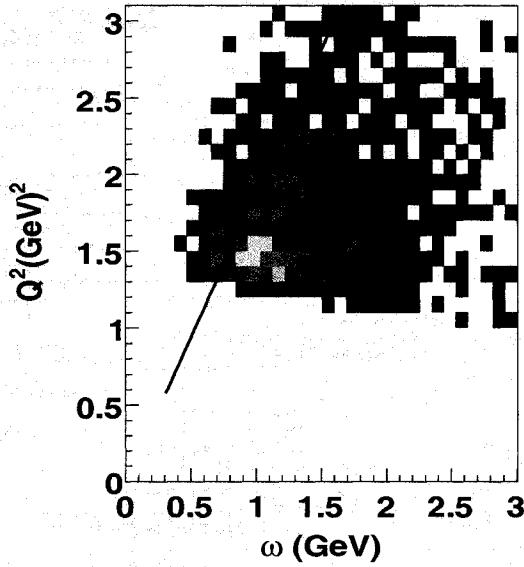
FIG. 104. Q^2 vs ω for $^3\text{He}(e, e'pp)n$ events for 4.71 GeV/c beam energy and $p_n > 250$ MeV/c. The line shows the quasi-elastic condition $\omega = Q^2/2m_p$ or $x_B = 1$

versus each other. Note the peaks at the corners of the triangle. These peaks correspond to kinematics where one particle is taking almost all the energy of the virtual photon. The cuts shown on Figure 105 select regions [1] - when the neutron has most of the kinetic energy and each proton has less than 20% of the energy of the virtual photon

$$T_{p_1}/\omega < 0.2 \quad \text{and} \quad T_{p_2}/\omega < 0.2$$

and [2] - when one of the protons has most of the kinetic energy and the neutron and other proton each have less than 20% of the energy of the virtual photon

$$T_n/\omega < 0.2 \quad \text{and} \quad (T_{p_1}/\omega < 0.2 \quad \text{or} \quad T_{p_2}/\omega < 0.2)$$

where ω is the energy of the virtual photon. We will investigate these regions further.

Figure 106 shows the opening angle between the non-leading nucleons (pp or pn) for regions [1] and [2] respectively (blue curve). The interesting feature is the peak
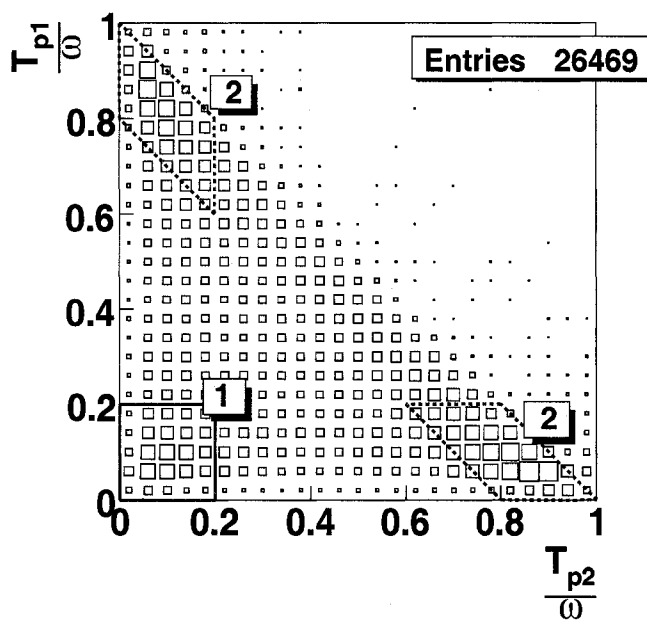
FIG. 105. Dalitz plot of the kinetic energies of two protons divided by the virtual photon energy. Region [1] correspond to the leading neutron and pp-pair, Regions [2] correspond to the leading proton and pn pair.
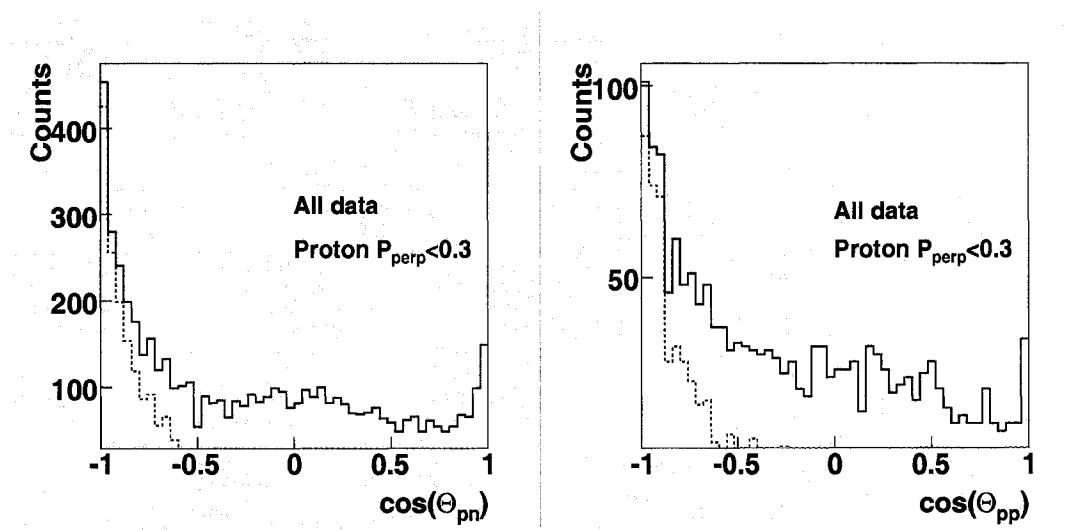
FIG. 106. The opening angle of the NN pair. a) pn pairs (cut [2]), b) pp pairs (cut [1]). Blue solid line corresponds to all data, magenta dashed line has a cut on the momentum of leading proton perpendicular to the virtual photon, $P_{N_t} < 300$ MeV/c

observed at 180^0. In this case the NN pair emerges back to back. The background under the peak can have several origins such as rescattering of the leading nucleon (FSI), Meson Exchange (MEC) or the leading nucleon might have been in an SRC with one of the other nucleons (in both cases the leading nucleons should have large momentum perpendicular to the momentum of virtual photon P_{N_t}). In order to remove the effects of FSI, we cut on $P_{N_t} < 300$ MeV/c. Figure 107 shows the dependence of P_{N_t} with the opening angle of the NN pair. As expected, large values of P_{N_t} correspond to smaller opening angles of the NN pair. Requiring $P_{N_t} < 300$ MeV/c reduces rescattering and decreases the background (see Figure 106).

Now that we have identified back to back NN pairs, we need to see if they are not involved in absorbing the virtual photon (i.e., they are spectators). If the pair is a spectator, then the opening angle of one of the non-leading nucleons with respect to $\vec{q}$ (Θ_{Nq}) should be isotropic. Figure 108 shows the Θ_{Nq} angular distributions for non-leading protons and neutrons. Note that the neutron distribution is almost isotropic but that the proton distribution is distorted by the CLAS angular acceptance (especially at back angles).

Another good observable to test if the pair is a spectator is the total momentum of the pair along the direction of the virtual photon, $P_{tot}^{\|q}$. Figure 109 shows $P_{tot}^{\|q}$ for pp and pn pairs. The average pair momentum parallel to the virtual photon is 140 MeV/c, which is approximately the Fermi momentum of a nucleon in ^{3}He. Also, $P_{tot}^{\|q}$ is much smaller than the momentum of the virtual photon. Thirdly, $P_{tot}^{\|q}$ does not increase with q, as would be expected if the pair was involved in absorbing the virtual photon (see Figure 109 (c) and (d)). These indicate that the NN pair was not involved in the reaction.

To investigate further the non-zero $P_{tot}^{\|q}$, we plotted the angle between the total momentum of the spectator pair and $\vec{q}$ (Θ_{tot}^q) (see Figure 110 a) and b)). The enhancement close to 0^0 comes from the larger x_B (see Figure 110 c) and d)) and is responsible for the large $P_{tot}^{\|q}$. This agrees with the results from [4] where the effect of SRC was observed at large x_B but in this case the leading nucleus should be in SRC and initially should have large momentum opposite to the direction of the virtual photon. As the two spectator particles are almost back to back this can be an indication of three nucleon correlations.

5.3.1 Spectator pair momentum distributions

The combination of all these observables gives us a good argument that what we observe is actually two nucleon spectator correlated pairs (two or maybe even three body SRC). The next investigated observables will be the relative and total momenta of the spectator pair. The relative momenta for the spectator pair is:

$$\vec{p}_{rel} = (\vec{p}_{N_1} - \vec{p}_{N_2})/2$$

and the total momentum is

$$\vec{p}_{tot} = (\vec{p}_{N_1} + \vec{p}_{N_2})$$

Figure 111 shows the distribution of relative and total momenta for pp and pn spectator pairs. The relative momentum of the pair starts from 250 MeV/c due to the minimum momentum of all particles of 250 MeV/c. The total momentum distribution peaks around 300 MeV/c. Figure 112 shows the cross section plotted versus relative and total momentum for pn and pp spectator pairs in comparison with the PWIA+Pair Distortion (PWIA+PD) calculation by Golak et $al.$ and the PWIA+PD+FSI calculation of Sargsian et $al..$ Figure 113 shows the same data compared with the calculations by Golak et $al.$ and the diagrammatic calculation of Laget. The Golak model includes exact wave functions of both the ^{3}He and the continuum NN state. The calculation is several times smaller than the experimental data. Sargsian's calculations include the SAID parametrization for the continuum NN state and the generalized eikonal approximation for leading nucleon FSI. Sargsian's calculation gives some description of the relative momentum of pn spectator pairs but his cross sections are lower than the experimental results. The ratio of σ_{pn}/σ_{pp} differs a lot from the data. Laget's calculation provides some agreement for the pp spectator pair (see Figure 113) but the cross sections for the pn spectator pair are larger than the experimental results. The ratio of σ_{pn}/σ_{pp} differs a lot from the data.

The next step is to examine the Q^2 dependence by comparing to the 2.2 GeV results [22]. In this case the kinematic region is different (Q^2 range is from 0.5–1 GeV^2) but the naive expectation is that the effect of the SRC should not depend on the energy of the probe. Figure 114 shows the cross section for the relative and total momentum of the pp and pn pairs with the 2.2 GeV incident beam. The 4.7 and 2.2

GeV cross sections have similar isospin dependence:

$$\frac{\sigma_{pn}}{\sigma_{pp}}(2.2 \text{ GeV}) = 3.14 \pm 0.71$$

$$\frac{\sigma_{pn}}{\sigma_{pp}}(4.7 \text{ GeV}) = 4.5 \pm 0.7$$

where the error includes the systematical errors of both experiments. The closest calculated $\frac{\sigma_{pn}}{\sigma_{pp}}(4.7 \text{ GeV})$ ratio is obtained from Golak *et al.* and equal to 2.9 and $\frac{\sigma_{pn}}{\sigma_{pp}}(2.2 \text{ GeV})$ is 4.3. Table IX shows the integrated cross sections for the calculations and experimental results. The ratios between 2.2 GeV and 4.7 GeV data are

$$\frac{\sigma_{pp}(2.2 \text{ GeV})}{\sigma_{pp}(4.7 \text{ GeV})} = 6.33 \pm 1.2$$

and

$$\frac{\sigma_{pn}(2.2 \text{ GeV})}{\sigma_{pn}(4.7 \text{ GeV})} = 4.36 \pm 0.86$$

Laget's calculation describes these ration well, although its pn/pp ratios are about
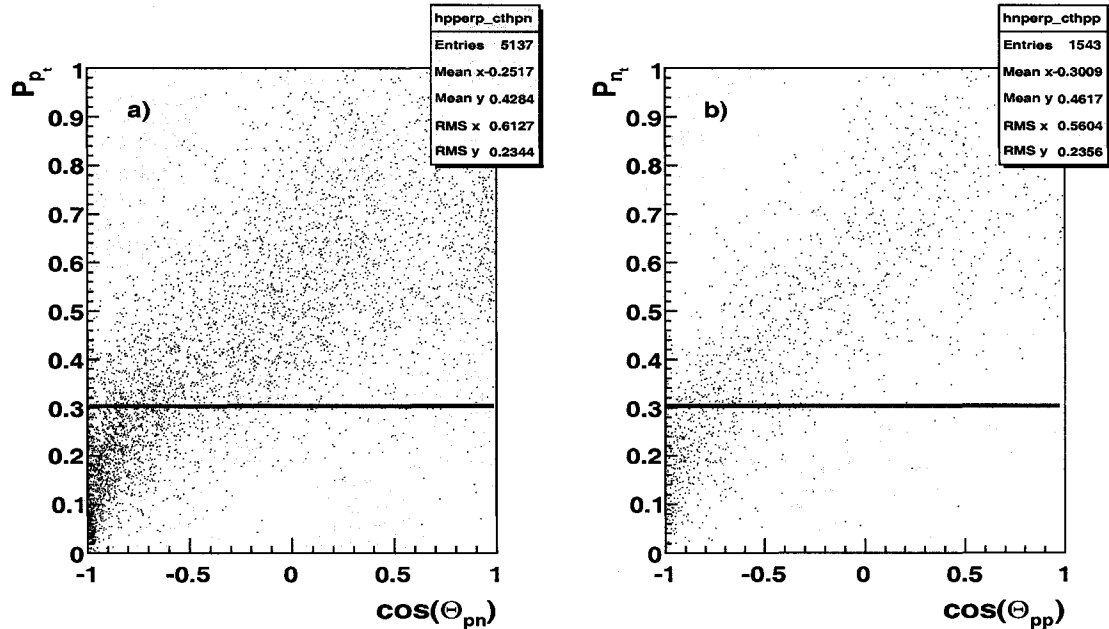
FIG. 107. Momentum of the leading nucleon perpendicular to the virtual photon versus opening angle of NN pair. a) leading proton and pn pair, b) leading neutron and pp pair.

TABLE IX. Integral cross sections for experiment and calculations.

		$\sigma(2.2\text{ GeV})$	$\sigma(4.7\text{ GeV})$	$\sigma(2.2)/\sigma(4.7)$
	pp	171	27	6.3±1.2
Data (fb/MeV)	pn	537	123	4.4±0.8
	pn/pp	3.1±0.7	4.5±0.7	−
	pp	200	30	6.7
Laget (FULL)	pn	925	228	4
	pn/pp	4.6	7.6	−
	pp	77	8.7	9
Golak (PWIA+PD)	pn	334	25	13
	pn/pp	4.3	2.9	−
	pp	550	89	6.2
Golak (PWIA)	pn	12350	750	16.5
	pn/pp	22.9	16.8	−
	pp	−	2.9	−
Sargsian (FULL)	pn	−	40	−
	pn/pp	−	13.7	−
	pp	−	4.2	−
Sargsian (PWIA+PD)	pn	−	89.5	−
	pn/pp	−	21.4	−

50% too high.

Figure 115 shows a direct comparison between the 4.7 GeV and the 2.2 GeV data. The cross section for 4.7 GeV was multiplied by 5.3 in Figure 115. The comparison shows very good agreement in both sets of data with each other. Even the shapes are similar. Figure 115 shows a small difference in the relative momentum. The difference between the p_{rel} plots probably comes from the extra kinematic coverage at 4.7 GeV. Since $T_p/\omega < 0.2$, this limits the maximum momentum accessible. Tables XI and X in Appendix C shows the cross section for relative and total momentum for 2.2 and 4.7 GeV.

The Golak (PWIA+PD and Golak (PWIA) calculations (see Table IX) show that Pair Distortion reduces the pp and pn pair cross sections by an order of magnitude. Laget sees similar effects.
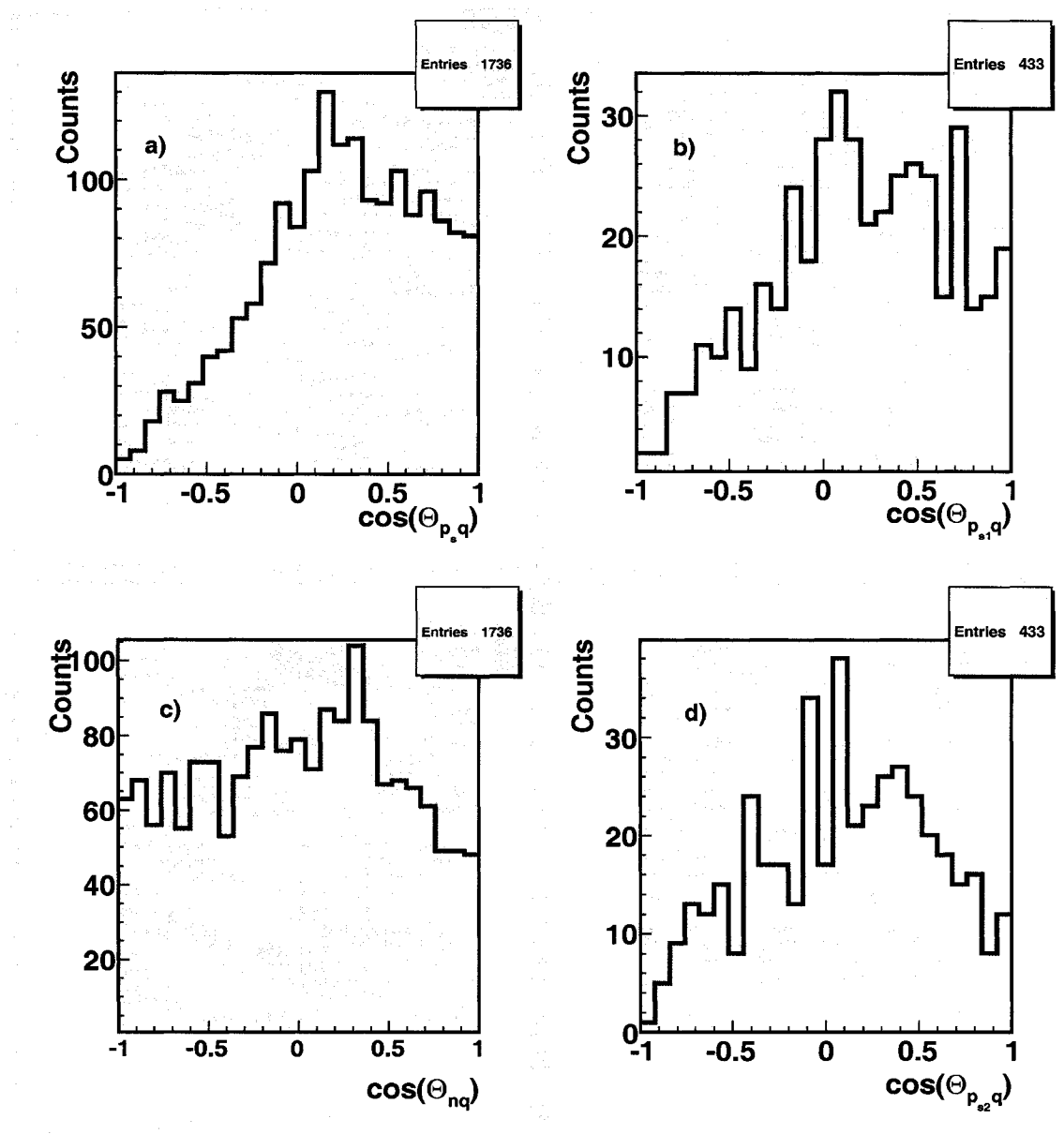
FIG. 108. Angle between a non leading nucleon and $\vec{q}$. a) proton in pn pair c) neutron in pn pair , b) and d) protons in pp pair.
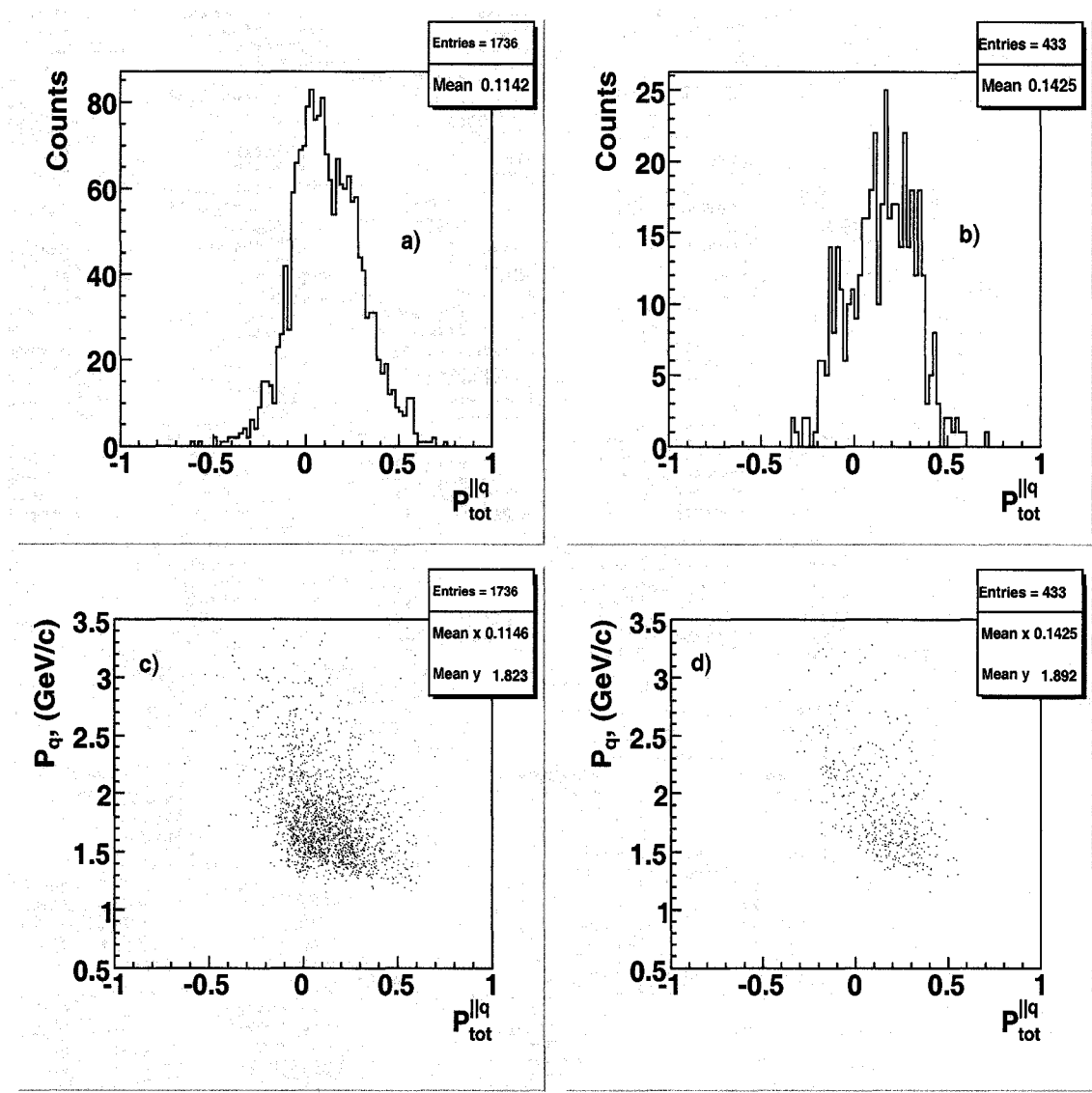
FIG. 109. Total momentum of the NN pair parallel to the direction of virtual photon, $P_{tot}^{\|q}$ a) pn pair, b) pp pair. $P_{tot}^{\|q}$ versus photon momentum q c) pn pair and d) pp pair.
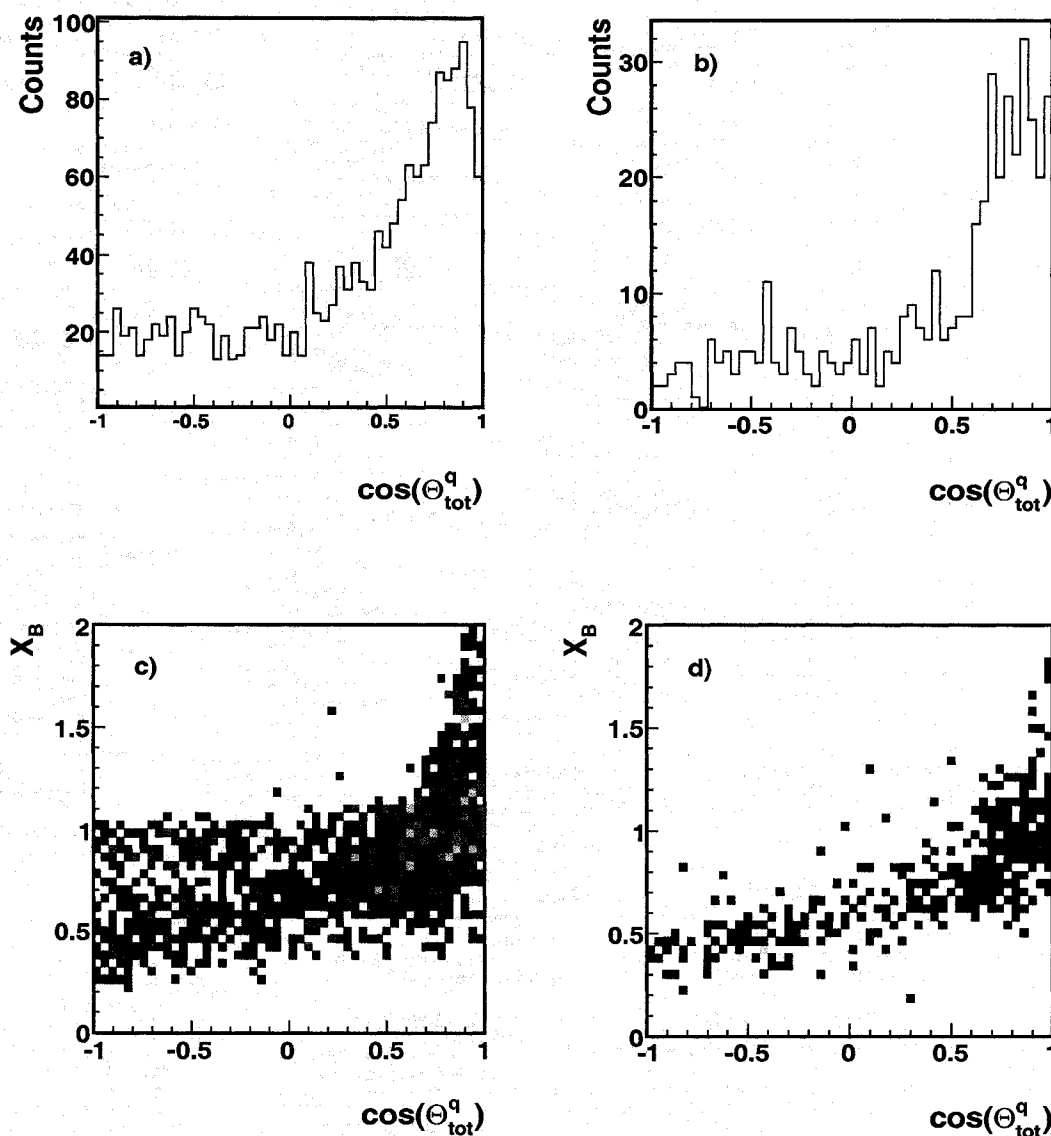
FIG. 110. Angle between the total momentum of the spectator pair and $\vec{q}$. a) and c) pn spectator pair, b) and d) pp spectator pair. c) and d) shows dependence on Bjorken x_B.
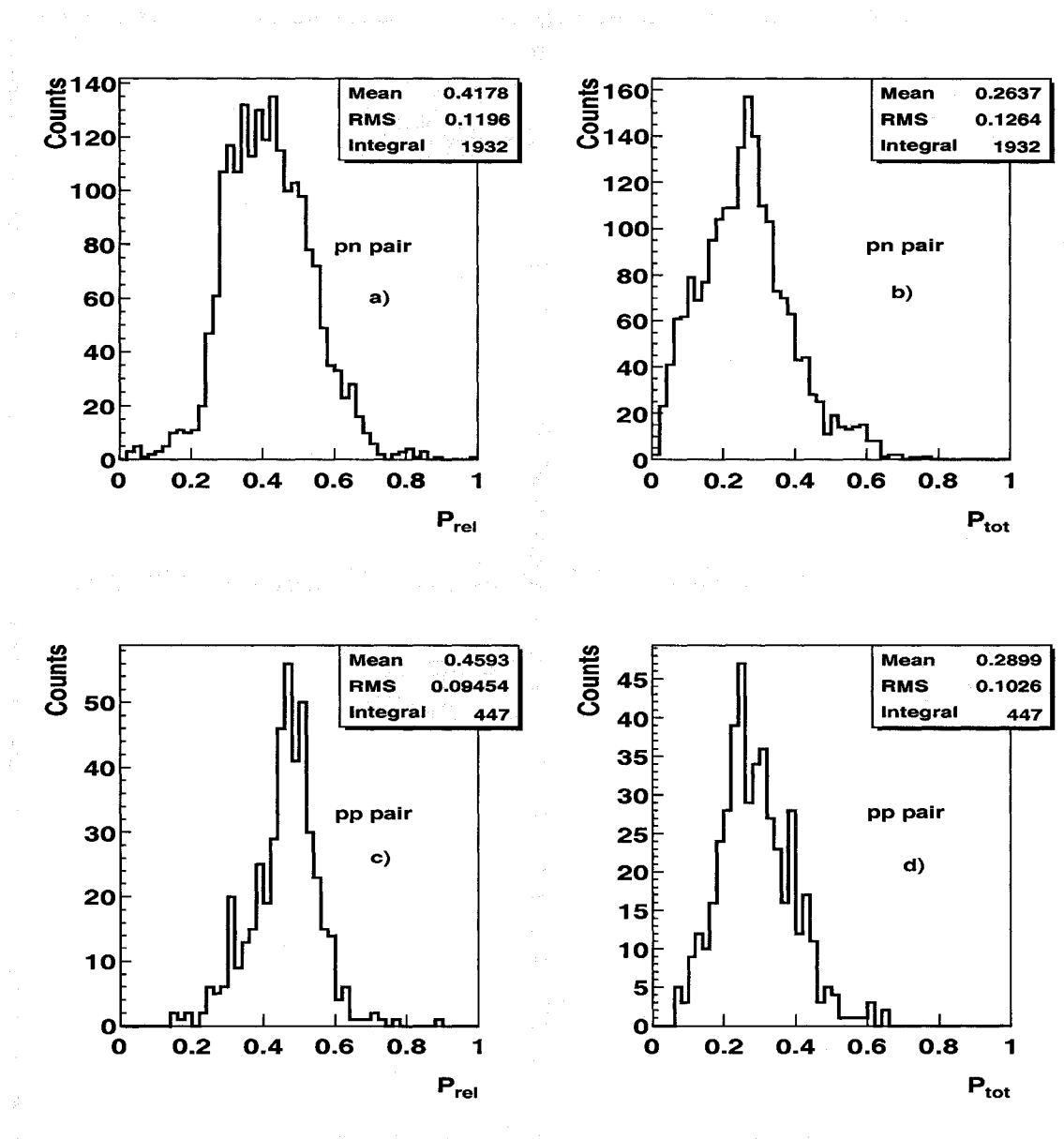
FIG. 111. Relative and total momentum distributions a) and b) p_{rel} and p_{tot} for pn pair (4.7 GeV beam), c) and d)p_{rel} and p_{tot} for pp pair.
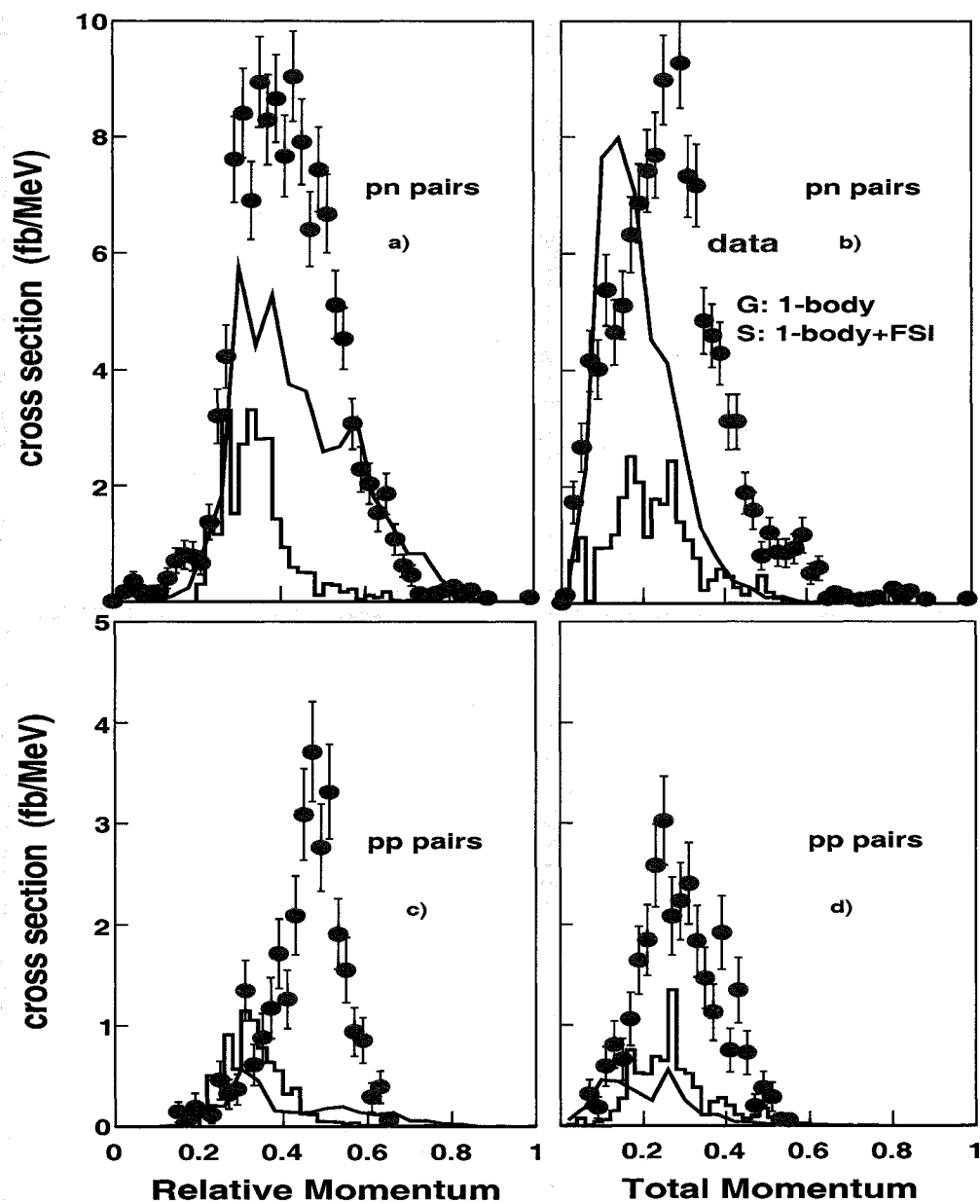
FIG. 112. Cross section vs relative and total momentum a) and b) for pn spectator pair, c) and d) for pp spectator pair. Blue line shows calculations by Golak *et al.* (Golak FULL), magenta line shows calculations by Sargsian *et al.* (Sarg FULL).
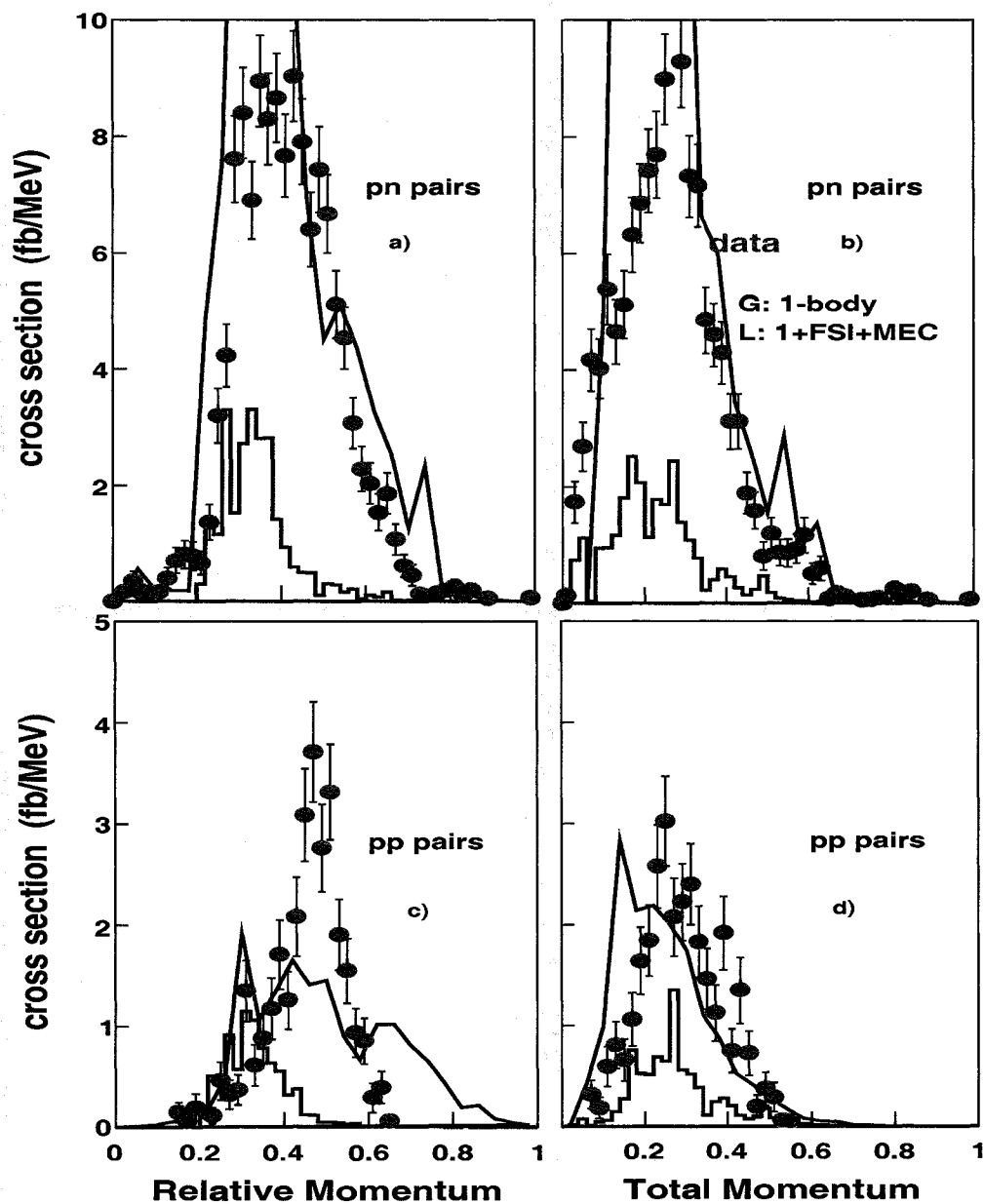
FIG. 113. Cross section vs relative and total momentum a) and b) for pn spectator pair, c) and d) for pp spectator pair. Blue line is calculations by Golak *et al.* (Golak FULL), red line calculations by Laget (Laget FULL).
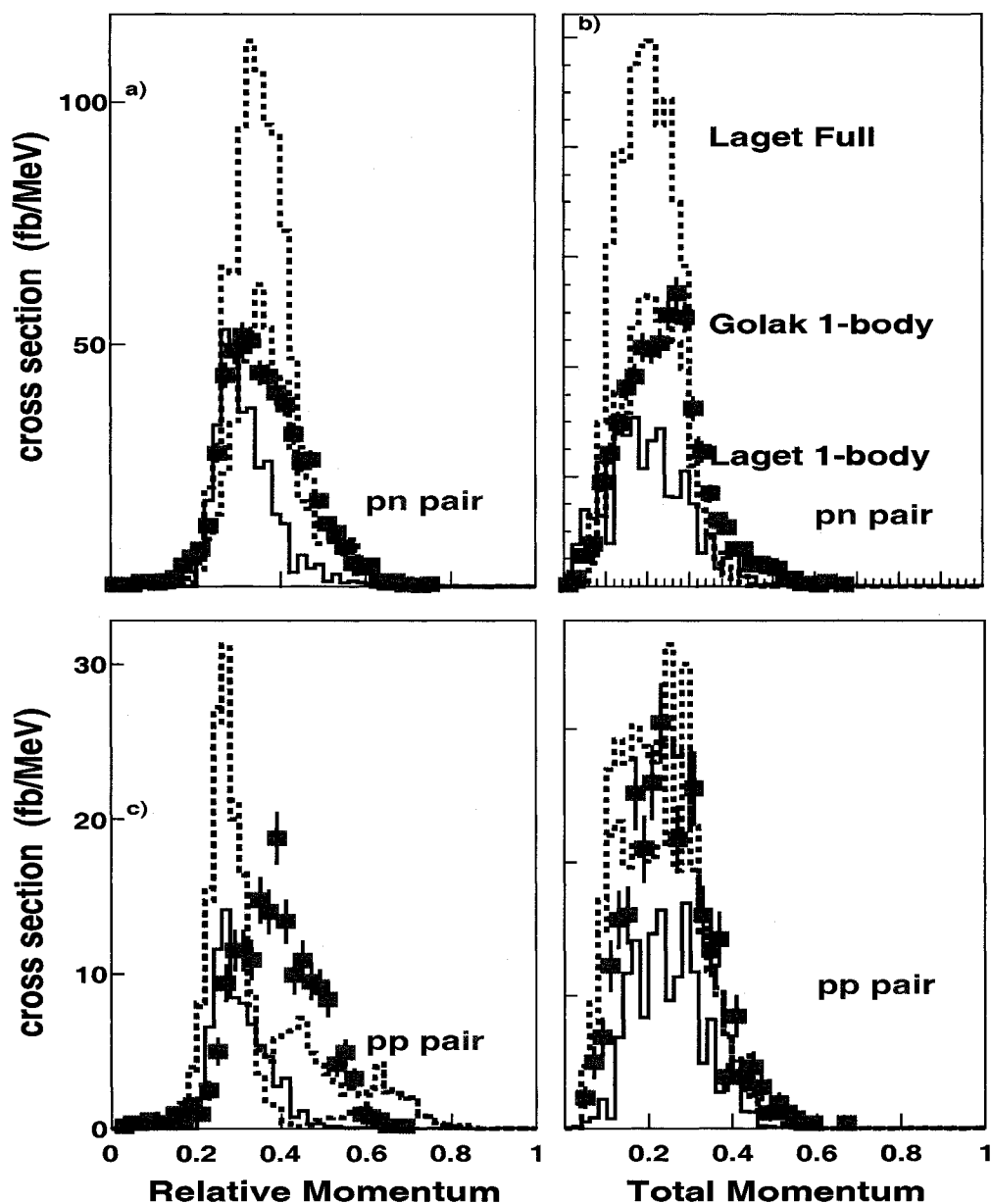
FIG. 114. Cross section vs relative and total momentum for 2.2 GeV beam (data by Niyazov *et al.*) a) and b) for *pn* spectator pair, c) and d) for *pp* spectator pair. Blue solid line shows calculations by Golak *et al.*, red line calculations by Laget 1-Body+FSI+MEC2,3, black - Laget 1-Body (PWIA+PD).
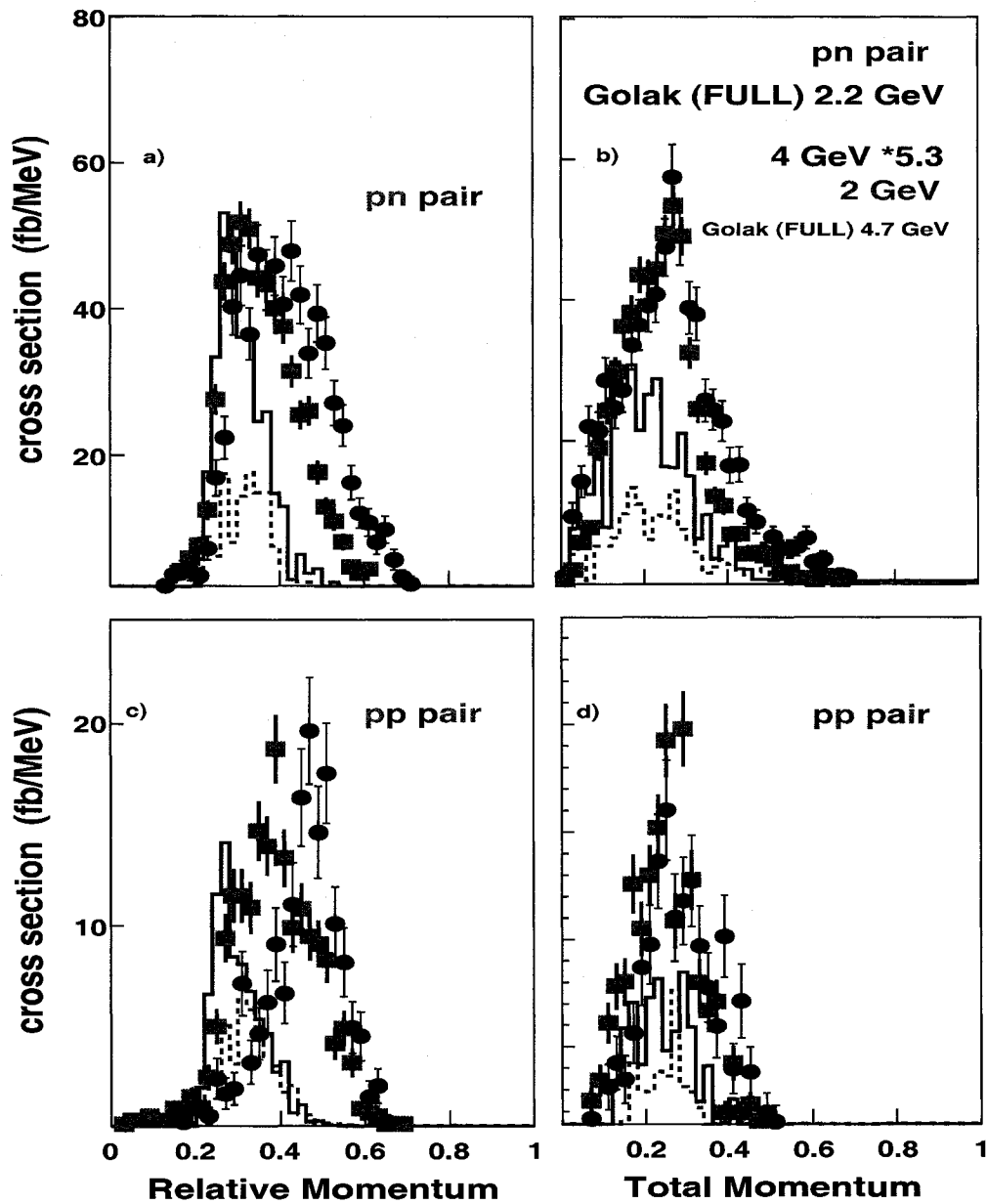
FIG. 115. Relative and total momentum cross section a) and b) for pn spectator pair (2.2 GeV beam (Niyazov *et al.*) in green boxes 4.7 GeV in red circles), c) and d) for pp spectator pair. Blue solid and magenta dashed lines are calculations by Golak *et al.* for 2.2 GeV and 4.7 GeV respectively.

5.3.2 Discussion and Summary

- When all three nucleons are active we see peaks at the corners of the Dalitz plot, where the leading nucleon has most of the transferred energy ω and the other two share less than 20% of ω.

- The residual pair is emitted primarily back to back. When we require that $P_{N_t} < 0.3$ GeV/c (to minimize the effect of FSI) the residual pair is almost entirely back to back.

- These residual pairs are spectators to the reaction.

    - the neutron is emitted isotropically.

    - the total momentum of the pair along $\vec{q}$ ($P_{tot}^{\|q}$) is small (140 MeV/c) and much less than $|\vec{q}|$.

    - $P_{tot}^{\|q}$ is uncorrelated with $|\vec{q}|$.

- Since the residual nucleons are spectators and have initial momenta larger than the typical nucleon momentum in ^{3}He, we conclude that they come from two- or three- nucleon Short Range Correlations.

- The shapes of the cross section versus relative and total momentum for 2.2 GeV and 4.7 GeV are similar.

CHAPTER 6

SUMMARY

Experiment E2b was performed May 2 through June 23 of 2002 using the CE-BAF Large Acceptance Spectrometer (CLAS) in Hall-B at the Thomas Jefferson National Accelerator Facility. The data were collected on two targets (^{3}He and ^{56}Fe) at different energies of the incident electron beam (0.98, 4.462 and 4.71 GeV).

Obtained experimental data were:

- Calibrated

- Corrected for the misaligned detectors and magnetic fields (Angle and Momentum Corrections)

- Corrected for off center beam position (Vertex corrections)

- Corrected for energy loss

To eliminate regions where the detection efficiency is changing rapidly we applied the fiducial cuts.

Also to correct the cross section we calculated:

- the efficiency of the electromagnetic calorimeter cuts

- the efficiency of the reconstruction

- electron and proton efficiencies

- the radiative correction

We studied the ^{3}He$(e, e'pp)n$ reaction at a beam energy of 4.71 GeV and compared our data to previous results at 2.2 GeV.

Two kinematical regions were studied. The first had two protons with momentum $p_p > 250$ MeV/c and a slow neutron with momentum $p_n < 200$ MeV/c. this kinematics was dominated by final State Interactions. When we compared kinematics where both protons went forward ($\theta_{pq} < 35\circ$) to kinematics with one backward

proton ($\theta_{pq} > 100\circ$), the shape of the relative momentum distribution was very different. Calculation by Laget, although they describe the FSI–dominated region well, do not describe the forward or backward regions well.

The second kinematical region had three active nucleons, $p_N > 250$ MeV/c. This region is dominated by events where one nucleon has most of the kinetic energy and the oter two each have less than 20%. When we require that the leading nucleon has less than 300 MeV/c perpendicular momentum with respect to q, then the other two nucleons are predominantly back-to-back. Angular and momentum distributions indicate that this back-to-back pair was not involved in absorbing the virtual photon. We calculates the relative and total momentum distributions for pp and pn pairs. Unfortunately, although different calculations discribe different aspects of the data, none describe all of it well. The pair relative and total momentum distributions are very similar for 4.7 GeV and 2.2 GeV data, with relative scale factor of 5.3. This also indicates that we have measured distorted joint NN pair momentum distribution.

It is very important to improve the theoretical descriptions.

Previous experiments showed the importance of SRC and measured their magnitude. These ^{3}He($e, e'pp$)n measurements (this thesis and work done by Niyazov *et al.*) are the first to measure the joint distorted momentum distribution of the correlated pairs.

BIBLIOGRAPHY

[1] H. Feldmeier, T. Neff, R. Roth, J. Schnack Nucl.Phys. **A632** 61-95(1998).

[2] A. Nogga *et al*, Phys. Rev. C **67**,034004 (2003).

[3] C. Ciofi *et al.*, Phys. Rev. C **53**, 4 (1996).

[4] K. Egiyan *et al.*, Phys. Rev. C 68, 014313 (2003).

[5] L.L. Frankfurt, M.I. Strikman, D.B. Day, M.M. Sargsyan, Phys. Rev. C **48**, 2451, (1993).

[6] I. Bobeldijk *et al*, Phys. Rev. Lett. **73** 2684 (1994).

[7] V. R. Pandhripande and S. C. Pieper, Nucl. Phys. **A507** 167c (1990).

[8] Z. Y. Ma and J. Wambach, Phys. Lett. **B256** 1 (1991).

[9] C. Mahaux and R. Sartor, Adv. Nucl. Phys. **20** 1 (1991).

[10] E. N. Quint, Ph.D. thesis, University of Amsterdam unpublished (1998).

[11] J. J. Kelly, Phys. Rev. C **60**, 044609 (1999).

[12] J. Ryckebusch *et al.*, Nucl. Phys. **A624**, 581 (1997).

[13] J. Ryckebusch *et al.*, Nucl. Phys. **A476**, 237 (1988).

[14] J. Ryckebusch *et al.*, Nucl. Phys. **A503**, 694 (1989).

[15] S. Janssen *et al.*, Nucl. Phys. **A672**, 285 (2000).

[16] J.P. Jeukenne and C. Mahaux, Nucl. Phys. **A394**, 445 (1983).

[17] N. Liyanage *et al.*, Phys. Rev. Lett. **86**, 5670, (2001).

[18] R. Starink *et al.*, Phys. Lett. **B474**, 33 (2000).

[19] C. Giusti *et al.*, Phys. Rev. C **57** 1691 (1998).

[20] D. L. Groep *et al.*, Phys. Rev. Lett. **83**, (1999).

[21] L.Machenil *et al.*, Phys. Lett. **B316**, 17 (1993).

[22] R. Niyazov, L. Weinstein, Phys. Rev. Lett. **92** 052303 (2004).

[23] M. M. Sargsian private communications.

[24] M. M. Sargsian, T. V. Abrahamyan et. all arXiv:nucl-th 0406020.

[25] L.L. Frankfurt, W.R. Greenberg, G.A. Miller, M.M. Sargsian and M.I. Strikman, Z.Phys. **A352** 97 (1995).

[26] L.L. Frankfurt, M.M. Sargsian and M.I. Strikman, Phys. Rev. **C56** 1124 (1997).

[27] M. M. Sargsian, Int. J. Mod. Phys. E **10**, 405 (2001).

[28] G. Brown and A.D. Jackson, *The Nucleon Nucleon Interaction*, North-Holland Publishing Company, (1976).

[29] R. A. Arndt, I. I. Strakovsky and R. L. Workman, Phys. Rev. C **62** 034005 (2000).

[30] T. V. Abrahamyan, *Master's Thesis*, unpublished, FIU, (2003).

[31] J. M. Laget, nucl-th/0407072, (2004).

[32] L.L. Frankfurt, J.A. Miller and M.I. Strikman, *Ann. Rev. Nucl. Part. Sci.* **44**, 501 (1994).

[33] W. Glöckle,J. Golak, R. Skibiński, H. Witała, arXiv:nucl-th 0312006.

[34] H. Witała *et al.*, Few-Body Syst. **3** 123 (1988).

[35] R. B. Wiringa *et al.*, Phys. Rev. C **51** 38 (1995).

[36] D. O. Riska, Phys. Scr. **31** (1985) 107 (1985); **31** 471 (1985).

[37] R. Schiavilla *et al.*, Phys. Rev. C **41** 309 (1990).

[38] A. Nogga *et al.*, Phys. Rev. C **67** 034004 (2003).

[39] W. Glöckle, *The Quantum Mechanical Few-Body Problem*, Springer-Verlag, Berlin, (1983).

[40] J. Golak *et al.*, Phys. Rev. **C 52** (1995) 1216

[41] J. Golak *et al.*, Phys. Rev. **C 52** 1216 (1995).

[42] V. Blobel and CLAS software group, "The BOS System for CLAS Software", November 25, (1995).

[43] G. Adams *et al.*, "CLAS detector", Preprint submitted to Elsevier Science, July 15, (2002).

[44] M. D. Mestayer *et al.*, Nucl. Instr. and Meth. **A449**, 81 (2000).

[45] L. Qin *et al.*, CLAS-NOTE **1996-018** JLAB, (1996).

[46] G. Adams *et al.*, Nucl. Instr. and Meth. **A465**, 414 (2001).

[47] E. S. Smith *et al.*, Nucl. Instr. and Meth. **A432**, 265 (1999).

[48] M. Amarian *et al.*, Nucl. Instr. and Meth. **A460**, 239 (2001).

[49] R.M Gibbons, D.I Nathan, Thermodynamic Data of Helium-3, Tech. Report AFML-TR-67-175, Air Force Materials Laboratory, October 1967, Reproduced by U.S. Department of Commerce.

[50] Kim Egiyan, CLAS-NOTE **1999-007** JLAB, (1999).

[51] D. Lawrence, M.D. Mestayer, *CLAS Drift Chamber Calibration Procedures*, CLAS-NOTE 99-011(1999)

[52] H.Egiyan, *Minutes of the CLAS CALCOM Analysis Meeting*,(1997).

[53] C. Smith, EC Energy Calibration. http://www.jlab.org/ lc-smith/EC_Energy_Calibration.html

[54] S.E. Kuhn, A.V. Klimenko *Momentum corrections for E6*, CLAS-NOTE 03-005 (2003)

[55] A.V. Klimenko *Electron Scattering from a High Momentum Neutron in Deuterium*, Thesis (2004)

[56] J.M. Musolf *et al*, Phys. Rep. **239**, 1 (1994)

[57] J. Schwinger, Phys. Rev. **76**, 760 (1949).

[58] L.W. Mo and Y.S. Tsai, Rev. Mod. Phys. **41**, 205 (1969).

[59] Y.S.Tsai, Rev. Mod. Phys. **122**, 1898 (1961).

[60] Juncai Gao, Ph.D. Thesis, MIT (1999).

[61] H. Uberall, "Electron Scattering from Complex Nuclei", Academic Press, (1971).

[62] J.-M. Laget Private communications.

[63] M. Sargsian Private communications.

APPENDIX A

ELECTRON FIDUCIAL CUTS

Fortrane code for electron fiducial cuts:

```
SUBROUTINE EFID_CUT_4710MeV(p,thEl,phiEl, del_phie)
cc electron fiducial cuts for 4.71 GeV data !!Hovannes 24/07/04
cc output int status 1 means passing, 0 means failurec
cc// Input of a functon:
cc// thEl - theta of electron (degress) in DC
cc// phiEl - phi of electron (degrees [-180,180)) in DC
cc// sectEl - DC sector
cc /// p in Gev
REAL a(4),thcut,exp , del_phie,parfid(8),deg2rad
data parfid /11.5,23.5,0.25,32.,11.5,23.5,0.25,32./
INTEGER status, sectEl
deg2rad=acos(-1.)/180
del_phie=0
status=0
if(p.le.3.0)then
a(1)=parfid(1)
a(2)=parfid(2)
a(3)=parfid(4)
a(4)=parfid(3)
else if(p.gt.3.0)then
a(1)=parfid(5)
a(2)=parfid(6)
a(3)=parfid(8)
a(4)=parfid(7)
endif
if(phiEl.lt.-30) phiEl = phiEl+360
if(phiEl.gt.330) phiEl = phiEl-360
sectEl = int((phiEl+30)/60.)+1
```

```fortran
if(sectEl.lt.1)sectEl = 1
if(sectEL.gt.6) sectEl = 6
phiEl = phiEl-(sectEl-1)*60
thcut = a(1)+a(2)/((p+0.15)*3375/2250.)
exp = a(4)*(p*3375./2250)**0.2
if ((thEl-thcut).le.0.) go to 1
del_phie = a(3)*(sin((thEl-thcut)*deg2rad))**exp
if(abs(phiEl.gt.del_phie).and.abs(phiEl).lt.24.and.p.gt.0.8) status=1
1 continue
if(del_phie.gt.24.)del_phie=24.
if(status.ne.1) del_phie=0.
return
end
```

C code for electron fiducial cuts:

```c
Double_t ElFidCut(TLorentzVector V4E) {
// Input of a functon:
// 4 vector of the electron
//
Double_t parfid[8]={11.5,23.5,0.25,32.,11.5,23.5,0.25,32.};
Int_t status=0;
Double_t a[4];
Double_t phiEl=V4E.Phi()*rad2deg,phi;
Double_t thEl=V4E.Theta()*rad2deg;
if(phiEl<-30) phiEl += 360;
phi=phiEl;
Int_t sectEl = Int_t ((phiEl+30)/60);
if(sectEl<0)sectEl = 0;
if(sectEl>5) sectEl = 5;
phiEl -= sectEl*60;
Double_t p=V4E.P();
```

```
if(p<=3.0) {a[0]=parfid[0];a[1]=parfid[1];a[2]=parfid[3];a[3]=parfid[2];}
if(p>3.0) {a[0]=parfid[4];a[1]=parfid[5];a[2]=parfid[7];a[3]=parfid[6];}
Double_t thcut = a[0]+a[1]/((p+0.15)*3375/2250);
Double_t exp = a[3]*pow(p*3375./2250,0.2);
Double_t del_phie = a[2]*pow(sin((thEl-thcut)*deg2rad),exp);
if(phiEl<del_phie&&phiEl>-del_phie&&phiEl<24&&phiEl>-24&&p>1.)    status=1;
if(del_phie>24.) {
del_phie=24.;
}
if(status!=1) del_phie=0.;
return del_phie;
}
```

APPENDIX B

PROTON FIDUCIAL CUTS

subroutine PFiducialCut_4710MeV(pp, theta, phi, status)

c Protons fiducial cuts 4.71 GEV !!Hovannes 24/07/04

c output int status 1 means pass, 0 means failure

c// Function consist from strait cut on

c// 1. theta < 12 —degree

c// 2. theta > -1.3/pp+140

c// 3. abs(phi) < 24

c// 4. phi < 30-4.5/sin(theta-theta0_up) —degree

c// 5. phi > -30+3.5/sin(theta-theta0_down)

c// where

c// theta0_up=U[sect][1]/pp+U[sect][2]+U[sect][3]*pp+U[sect][1]*pp2

c// pp – Momentum in Gev

c// date: 2003/10/10

c// Author : Baghdasaryan Hovhannes

c//

REAL U(4,6)/

, 3.1668,-2.2207,0.81481,-0.65013E-01,

, 4.0110,-2.6646,0.39324,-0.11068E-01,

, 6.5960,-9.5039,2.8438 ,-0.34189,

, 2.8263,0.83451,-4.7386 ,1.1387,

, 4.5659,-4.1917,-1.2117,0.37767,

, 4.9512,-3.3722,0.32571,-0.17245E-01/

REAL D(4,6)/

, 4.5517,-6.5451, 5.1488,-1.0008,

, 1.0820,2.8670,-1.7367,0.40615,

, 2.3644,-0.33861,-0.89477E-01,0.18516,

, 2.95,-0.81404,0.91378,-0.1422,

```
, 4.0755,-1.0917,2.7285,-0.45658,
, 1.4629,7.2206,-5.4606,1.2554/
REAL pp,theta
REAL theta0_up
REAL theta0_down
REAL phi
integer status
integer sect
REAL deg2rad
deg2rad=0.01745329


status= 0
if(pp.lt.0.25) then
status = 0
return
endif


if(phi.lt.-30) phi = Phi+360
if(phi.gt.330) phi = phi-360 !!Added 26/04/07
sect = int((phi+30)/60)+1 !! Corrected JML 24/07/04
if(sect.lt.1)sect = 1
if(sect.gt.6) sect = 6
phi = phi-(sect-1)*60 !! Corrected JML 24/07/04


theta0_up=U(1,sect)/pp+U(2,sect)+
, U(3,sect)*pp+U(4,sect)*pp*pp
theta0_down=D(1,sect)/pp+D(2,sect)+
, D(3,sect)*pp+D(4,sect)*pp*pp


if( theta.gt.12.and.theta.lt.-1.3/pp+140.and.phi.lt.24.and.
, phi.gt.-24)then
if(phi.lt.30-4.5/sin((theta-theta0_up)*deg2rad).and.
```

```
, phi.gt.-30+3.5/sin((theta-theta0_down)*deg2rad))status = 1
endif


return
end


Bool_t PFiducialCut(TLorentzVector V4P){
//
// Function consist from strait cut on
// 1. theta < 12
// 2. theta > -1.3/pp+140
// 3. abs(phi) < 24
// 4. phi < 30-4.5/sin(theta-theta0_up)
// 5. phi > -30+3.5/sin(theta-theta0_down)
// where
// theta0_up=U[sect][1]/pp+U[sect][2]+U[sect][3]*pp+U[sect][1]*pp^2
// date: 2003/10/10
// Author : Baghdasaryan Hovhannes
//


Float_t U[6][4]={
{3.1668,-2.2207,0.81481,-0.65013E-01},
{4.0110,-2.6646,0.39324,-0.11068E-01},
{6.5960,-9.5039,2.8438 ,-0.34189},
{2.8263,0.83451,-4.7386 ,1.1387},
{4.5659,-4.1917,-1.2117,0.37767},
{4.9512,-3.3722,0.32571,-0.17245E-01}};
Float_t D[6][4]={
{4.5517,-6.5451, 5.1488,-1.0008},
{1.0820,2.8670,-1.7367,0.40615},
{2.3644,-0.33861,-0.89477E-01,0.18516},
{2.95,-0.81404,0.91378,-0.1422},
```

```
{4.0755,-1.0917,2.7285,-0.45658},
{1.4629,7.2206,-5.4606,1.2554}};


Bool_t status = kFALSE;
Double_t theta0_up;
Double_t theta0_down;
Double_t theta = V4P.Theta()*rad2deg;
Double_t pp = V4P.P();
Double_t phi_in = V4P.Phi()*rad2deg;
Double_t phi = phi_in;
if(phi<-30) phi += 360;
phi_in=phi;
Int_t sect = Int_t ((phi+30)/60);
if(sect<0)sect = 0;
if(sect>5) sect = 5;
phi -= sect*60;


theta0_up=U[sect][0]/pp+U[sect][1]+U[sect][2]*pp+U[sect][3]*pp*pp;
theta0_down=D[sect][0]/pp+D[sect][1]+D[sect][2]*pp+D[sect][3]*pp*pp;


if( theta>12 && theta<-1.3/pp+140 && phi<24 && phi>-24)
if(phi<30-4.5/sin((theta-theta0_up)*deg2rad) &&
phi>-30+3.5/sin((theta-theta0_down)*deg2rad))status = kTRUE;
return status;


}
```

APPENDIX C

CROSS SECTION TABLES

Cross section versus relative and total momentum.

TABLE X. Cross section for total momentum of the pp and pn pairs (fb/MeV).

p_{tot}	$\sigma(pp)$ (4.7 GeV)	$\sigma(pn)$ (4.7 GeV)	$\sigma(pp)$ (2.2 GeV)	$\sigma(pn)$ (2.2 GeV)
0.110	0.590	5.39	6.10	24.22
0.130	0.805	4.66	7.82	29.77
0.150	0.656	5.12	8.00	36.27
0.170	1.06	6.32	12.58	38.18
0.190	1.64	6.87	10.48	43.54
0.210	1.84	7.42	12.97	43.13
0.230	2.58	7.70	15.22	44.29
0.250	3.02	8.98	19.26	49.42
0.270	2.08	10.9	10.85	53.42
0.290	2.22	9.29	19.79	49.06
0.310	2.40	7.33	12.76	32.46
0.330	1.83	7.17	7.98	24.45
0.350	1.46	4.85	6.68	16.81
0.370	1.12	4.60	7.07	12.04
0.390	1.91	4.29	1.92	10.74
0.410	0.748	3.12	4.21	6.69
0.430	1.35	3.12	1.92	6.72
0.450	0.722	1.89	2.29	3.84
0.470	0.197	1.59	1.54	4.03
0.490	0.371	0.803	0.57	3.65
0.510	0.286	1.19	0.96	3.08

TABLE XI. Cross section for relative momentum of the pp and pn pairs (fb/MeV).

p_{rel}	$\sigma(pp)$ (4.7 GeV)	$\sigma(pn)$ (4.7 GeV)	$\sigma(pp)$ (2.2 GeV)	$\sigma(pn)$ (2.2 GeV)
0.250	0.460	3.20	4.99	27.62
0.270	0.323	4.23	9.40	43.70
0.290	0.367	7.61	11.49	48.83
0.310	1.35	8.40	11.50	51.87
0.330	0.612	6.90	10.90	50.90
0.350	0.878	8.95	14.72	44.18
0.370	1.17	8.29	13.96	43.35
0.390	1.71	8.66	18.73	40.07
0.410	1.26	7.67	13.34	37.61
0.430	2.09	9.04	9.89	31.46
0.450	3.09	7.91	10.84	25.51
0.470	3.71	6.41	9.49	26.04
0.490	2.76	7.43	9.09	17.65
0.510	3.31	6.67	8.31	12.88
0.530	1.91	5.11	4.14	10.99
0.550	1.55	4.54	4.90	8.129
0.570	0.935	3.07	3.20	4.713
0.590	0.852	2.28	0.93	3.76
0.610	0.291	2.04	0.74	4.32
0.630	0.392	1.53	0.55	1.13
0.650	0.06	1.86	0.19	0.75
0.670	0.05	1.07	0.18	1.12
0.690	0.06	0.617	0.18	0.37
	27	123	171	537

VITA

Hovhannes Baghdasaryan

Department of Physics

Old Dominion University

Norfolk, VA 23529

ACADEMIC HONORS:

- 2005 SURA/Jefferson Lab Graduate Fellowship.

- 2004 ODU Physics Department Student Excellence Prize .

- 1999 Graduated Yerevan State University with Honors (Red Diploma).

- 1994 Second place, Armenian Physics Olympiad.

- 1993,1994, Third place, Armenian Mathematical Olympiad.

EDUCATION:

- PhD Physics, Old Dominion University, Norfolk, Virginia, 2007

- M.Sc. Physics, Old Dominion University, Norfolk, Virginia, 2005

- B.Sc. Physics, Yerevan State University, Yerevan, Armenia, 1999

EXPERIENCE:

2003 – present	Research Assistant, Old Dominion University
1999 - 2002	Research Assistant, Yerevan, Armenia, 375036
1998 – 1999	Junior Scientist, Yerevan Physics Institute

COMPUTER SKILLS:

- programming using C/C++, FORTRAN, Pascal,ROOT, PAW/PAW++.

- Extensive experience with UNIX(Solaris, AIX, HP-UX), Linux, Windows.

- System administrating on UNIX(Solaris, AIX, HP-UX), Linux.

Typeset using LaTeX.